POLITECNICO
MILANO 1863

SCUOLA DI INGEGNERIA INDUSTRIALE
E DELL'INFORMAZIONE

# Analysis of nuclear clustering at intermediate energies with the FOOT experiment

Master Thesis in
Nuclear Engineering

Author: **Alice Caglioni**

Student ID: 995321
Advisor: Prof. Stefano Luigi Maria Giulini Castiglioni Agosteo
Co-advisors: Dtt.ssa Silvia Muraro
Academic Year: 2022-23

# Abstract

The interaction between nucleons in nucleus-nucleus collisions promotes the formation of clusters, particularly $\alpha$-particles, within the nuclear medium. Understanding the emergence of $\alpha$ clustering phenomena and the resulting structures has been studied for an extended period. This thesis utilizes Monte Carlo (MC) simulations to study the fragmentation of Carbon (C) projectiles on a C target at 200 MeV/nucleon, generating excited states as potential candidates for $\alpha$-particle condensation. The analysis focuses on specific reactions where the projectile, interacting with the target, leaves the target either in the ground state or in a slightly excited state and subsequently decays into two or three $\alpha$-particles. In particular, this study concerns the possibility of using the FOOT (FragmentatiOn Of Target) experiment for this purpose. The FOOT apparatus makes use of a magnetic spectrometer setup for the detection of projectiles (e.g.: p, $^{12}$C, $^{16}$O) interactions along their path, as well as the identification and measurement of the generated fragments' properties. Through the information obtained from the detection of selected $\alpha$ particles, investigations into the correlation among them have been conducted. The distribution of the angular separation between pairs of $\alpha$ particles provides insights into the decay of $^{8}$Be, whether in the ground or in the excited state, produced by the intermediate stage of C ion projectiles' decay. The excitation energies of $^{8}$Be nucleus has been calculated based on the kinematics of the detected $\alpha$ particles. This experimental information is useful for updating the existing nuclear models at intermediate energies employed in MC code founded on theoretical investigations.

**Keywords:** Nuclear physics, Heavy ion reactions, Nuclear fragmentation, $\alpha$ clustering, Collective properties, Nuclear structure.

# Abstract in lingua italiana

L'interazione tra nucleoni durante collisioni nucleari favorisce la formazione di cluster, in particolare di particelle $\alpha$, all'interno del mezzo nucleare. La comprensione del fenomeno fisico dell'$\alpha$ clustering e l'analisi delle strutture risultanti è stato oggetto di studio per molto tempo. Questa tesi utilizza simulazioni Monte Carlo (MC) per studiare la frammentazione di proiettili di Carbonio (C) su un bersaglio di C a 200 MeV/nucleone, generando stati eccitati che promuovono la condensazione di particelle $\alpha$. L'analisi si concentra su reazioni specifiche in cui il proiettile, interagendo con il bersaglio, lascia quest'ultimo nello stato fondamentale o in uno stato leggermente eccitato e successivamente decade in due o tre particelle $\alpha$. In particolare, a questo proposito, viene impiegato l'esperimento FOOT (FragmentatiOn Of Target). L'apparato di FOOT (FragmentatiOn Of Target), è costituito da uno spettrometro magnetico per la rilevazione delle interazioni di proiettili (es. p, $^{12}$C, $^{16}$O) lungo il loro percorso, nonché per l'identificazione e la misurazione delle proprietà dei frammenti generati. Attraverso le informazioni ottenute dalla rilevazione delle particelle $\alpha$ selezionate, sono stati condotti studi sulle correlazioni tra di esse. La distribuzione dell'apertura angolare tra coppie di particelle $\alpha$ fornisce informazioni sul decadimento di $^{8}$Be, sia che avvenga dal suo stato fondamentale o eccitato, prodotto dalla fase intermedia del decadimento dei proiettili di ioni C. L'energia di eccitazione del nucleo di $^{8}$Be è stata calcolata a partire dalla cinetica delle particelle $\alpha$ rilevate. Le informazioni acquisite dall'analisi sperimentale verranno utilizzate per aggiornare gli attuali modelli nucleari a energie intermedie impiegati nel codice MC, i quali, fino ad ora, sono stati fondati su studi teorici.

**Parole chiave:** Fisica nucleare, Reazioni di ioni pesanti, $\alpha$ clustering, Proprietà collettive, Struttura nucleare.

# Contents

# Introduction

The propensity of objects to congregate together is a common and fascinating occurrence observed across various levels of the natural world. It applies to a wide range of situations, from the clustering of galaxies in space to the formation of social networks in the digital era. Essentially, this phenomenon indicates that entities attract each other. This attraction often leads to the creation of organized groups known as clusters, providing stability and balance through their configuration. More specifically, physical systems often transit to states with lower values of their potential energy. This collective behavior, known as clustering, is evident in a large variety of physical structures and across an extensive range of length scales from cosmic to subatomic.

Gravity plays a crucial role on the cosmic scale, forming galaxies and clusters of galaxies [1]. On a biological and social level, organisms and humans exhibit collective behavior for cooperation, protection, and resource sharing. At the molecular and atomic levels, there is a recognition of order and symmetry in the formation of molecules and crystal lattices. Even deeper, at the nuclear scale, the complexity of the nuclear force, involving nucleons and mesons with different ranges, leads to challenging computational calculations. Despite these challenges, ongoing advancements in nuclear physics provide insights into nuclear structure, correlations, and clustering, treating the nucleus as a complex many-body problem with analogies to condensed-matter physics [2].

Nevertheless, within the world of nuclear particles, remarkable and rather unconventional clustering effects were observed [3]. Nuclei, far from being static assemblages of nucleons, are dynamic systems where their constituents, namely protons and neutrons, move at velocities approaching significant fractions of the speed of light. This dynamic behaviour gives rise to strong correlations, driven by quantum mechanical effects. As an illustrative example, the Pauli exclusion principle forces nucleons to combine in a singlet spin state, imposing that their spins need to be anti-aligned. This minimizes the repulsion arising from the Pauli principle and enhances the binding energy of the system of light nuclei that have equal, and even, numbers of protons and neutrons.

Consequently, the highest correlated system within nuclei is the quartet 2p + 2n, com-

monly known as the $\alpha$ particle. This configuration offers a notable energy advantage due to its high binding energy per nucleon. Moreover, just as noble gases, the $^4$He nucleus has a closed shell and is rather inert. It has a first excited state close to 20 MeV, whereas the average binding energy per nucleon across all the nuclei is less than 8 MeV per nucleon. This implies that once these compact sub-units are formed, they can move undisturbed within the nuclear volume for a substantial duration. This phenomenon is referred to as $\alpha$-clustering and constitutes one of the most captivating aspects of Nuclear Physics.

In this thesis, clustering phenomena in light nuclei are investigating with particular attention on $\alpha$ clustering study. Such a phenomenology has been extensively studied at energies close to the Coulomb barrier and at Fermi energies, i.e. for projectile energies up to about 50 MeV/nucleon. However there are much less data at energies exceeding 150 MeV/u. New data could be very helpful to constraint theoretical models. This thesis concerns the possibility of employing for this purpose the experimental apparatus of the FOOT (FragmentatiOn Of Target) project, funded by INFN.

The FOOT experiment is designed to measure the differential cross sections in angle and energy ($d\sigma/d\Omega \cdot dE$) of the fragments produced in nuclear interactions of H, $^4$He, $^{12}$C and $^{16}$O beams impinging on targets of graphite (C), polyethylene ($C_2H_4$) and PMMA ($C_5O_2H_8$), at the energy range relevant for particle therapy (150-400 MeV/u) and space radioprotection (up to 800 MeV/u).

The data from the FOOT experiment will serve as a benchmark for the existing MC simulation tools, enhancing current nuclear interaction models and offering advantages to various physics fields. The experimental configuration for the FOOT experiment includes a magnetic spectrometer consisting of a pre-target beam measurement station, a particle tracking system operating in a magnetic field, a time-of-flight measurement system, and a calorimeter.

MC simulation was performed utilizing the FLUKA MC code, involving a primary beam of carbon ions with a kinetic energy of 200 MeV/u colliding with a carbon target. The analysis was focused on the selection of $\alpha$ particles generated from the fragmentation of projectile. Thorough the information acquired from the detection of the selected particles, investigations on the correlation between them have been performed. The data collected and analyzed by FOOT could contribute to model the physical phenomena of $\alpha$ clustering that have not been explored yet, thereby broadening the range of applications for the experiment.

In Chapter 1 an overview of the performed $\alpha$ clustering state of art will be presented. In addition, a focus on the experimentally observed clusters in $\alpha$-particle nuclei will be

reported. Chapter 2 is dedicated to describe the FOOT experiment, showing the aims, the strategy of measurements, the experimental setups and the software aspects. The software aspects related to the simulation and the reconstruction of particles implied in the research will be presented in Chapter 3. Chapter 4 will illustrate all the experimental measurements performed with the FOOT setup on the detected $\alpha$ particles. In particular, the methods and the results of the $\alpha$ clustering phenomena investigation will be shown.

# 1 | Clustering in nuclear Physics

## 1.1. Introduction

Clustering phenomena have an impact on numerous aspects across natural and social sciences. These phenomena involve the formation of sets of correlated objects that alter the behavior of a specific system by introducing symmetries and order. The concept of clustering has a deep-rooted history within the field of nuclear physics. Its appeal lies in the ability to transform the frequently uncorrelated actions of individual particles into structured and cohesive quasi-crystalline arrangements. Within this realm, clustering represents one of the most captivating outcomes of the Pauli exclusion principle and is a defining feature of a wide range of nuclear states, particularly in lighter nuclear systems. The nuclear structures resulting from these phenomena exhibit notable uniqueness and peculiarity, and their exploration holds significant importance in comprehending nuclear forces and their associated properties.

This chapter is dedicated to the theoretical and experimental investigation of clustering in light nuclear systems, employing various diverse and complementary techniques. A brief introduction on clustering phenomena development has been analysed in Section 1.2, in which is placed particular attention on nuclear clustering theories. In Section 1.3 are illustrated the various techniques for the study of clusters in light nuclei and their experimental applications are investigated in Section 1.4 and Section 1.5 based on the particles' range of energy implied in the experiments.

## 1.2. Nuclear clustering Developments

Much evidence for the presence of $\alpha$ clusters comes from nuclear structure calculations and from measurements of the cross sections of many nuclear reactions [4]. The structure calculations by Brink and Castro [5] showed that, when nuclear matter is reduced to about one-third of its density at the centre of heavy nucleus, it tends to coalesce into $\alpha$ clusters, while for higher densities the 2-nucleon deuteron condensation is preferred. This suggests that in the outer regions of the nucleus, where the density is low, it is very likely that $\alpha$ clusters will be found. In the case of light nuclei, the Hartree-Fock calculations of the nuclear density show very directly the regions of maximum density, three for carbon, four for oxygen, five for neon and so on, suggesting that these nuclei are made up of clusters of nucleons resembling $\alpha$ particles.

This potential phase of nuclear matter may extend to low-density states of self-conjugate lighter nuclei, in the same way as superfluid nuclei representing finite-size counterparts of superfluid nuclear matter. This means that, under specific conditions, $\alpha$ condensation might prevail over nucleon properties, even in finite nuclei.

For this reason, $\alpha$ particles have dominated the spectrum of cluster states in the history of this field. Nevertheless, other closed-shell systems, such as $^{16}$O and $^{12}$C (the latter having a closed sub-shell), offer some potential. Figure 1.1 provides visual representations of potential cluster candidates. However, both $^{16}$O and $^{12}$C possess relatively low energy levels for their first excited states and decay thresholds, which renders them less resistant to the destabilizing effects of other dynamics within the nucleus. Empirical $\alpha$-binding energies show clearly a proportionality with the number of bonds and, as a consequence, the $\alpha$-binding energy per number of bonds is surprisingly almost constant for each system, indicating an apparently constant $\alpha$-$\alpha$ interaction and the resilience of the $\alpha$-particle constituents in the ground states of light self-conjugated systems.

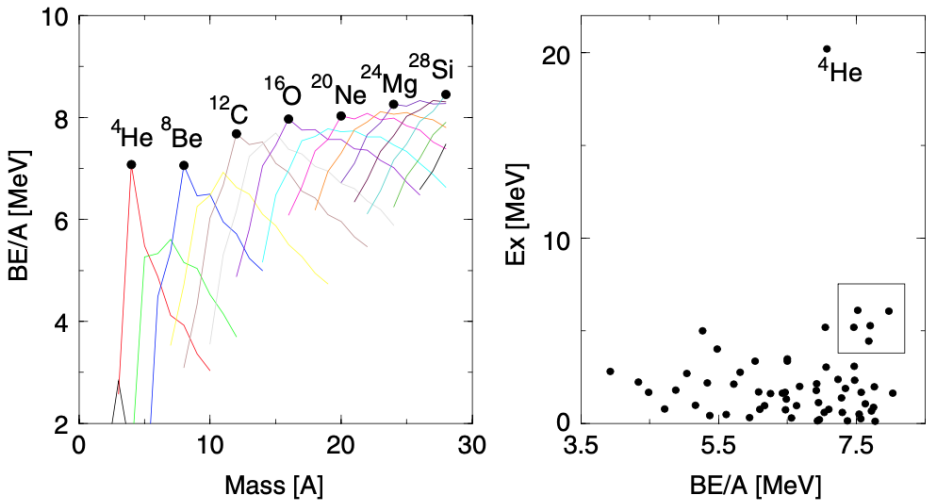


Figure 1.1: (Left) Binding energy per nucleon of light nuclear systems (up to A = 28), the lines connect isotopes of each element. The '$\alpha$ particle nuclei' are marked by the circles. (Right) Excitation energy of first excited states plotted versus binding energy per nucleon for nuclei up to A = 20. Good clusters should have both high binding energies and first excited states. The nucleus $^4$He is clearly an outstanding cluster candidate. The box drawn includes nuclei which may also form clusters; $^{12}$C, $^{14}$O, $^{14}$C, $^{15}$N and $^{16}$O [3].

The discovery of the $\alpha$-decay of heavy-nuclei initiated the idea that clusters of nucleons might be preformed prior to emission.

The first and simplest model aimed at the description of cluster states in nuclei is the so-called *$\alpha$-particle model*. It was developed in the 1930s, starting from the experimental observations of Wefelmeier [6] and of Hafstad and Teller [4]. In the $\alpha$-particle model the interaction of two neutrons and two protons (constituting an $\alpha$ particle) are first considered, and then the interaction of these groups with each other and with particles outside of the groups are considered. Hafstad and Teller brought out the fact that the binding energies per nucleon of *self-conjugated nuclei* (nuclei characterized by an equal number of protons and neutrons distributed over the same single particle orbits) showed local maxima, resulting from the appearance of clustering. This fact is evident in Figure 1.1, where self-conjugated configurations clearly exhibit peaks on the corresponding isotopic lines: all of these nuclei (e.g. $^4$He, $^8$Be, $^{12}$C) can be considered as composed by $\alpha$-particles.

Another important aspect pointed out by Hafstad and Teller was that, if one assumes an $\alpha$-particle structure of self-conjugated systems, their binding energies are linearly correlated with the possible number of connections between $\alpha$ centers. This evidence supported the assumption of a geometrical model describing these nuclei as a close packing of rigid

spheres ($\alpha$-particles), with a certain number of bonds (pairs of adjacent particles). In such a way, one can describe their binding energies as the sum of the binding energy of each constituent $\alpha$-cluster and the $\alpha$-binding energy, i.e. the binding energy associated to each bond between $\alpha$-particles. Figure 1.2 shows the correlation between the total binding energy of the lightest self-conjugated nuclei and the corresponding number of bonds, following the scheme of Hafstad and Teller, compared with the result of a linear fit. The geometrical arrangements of $\alpha$-particles in the first self-conjugated systems, up to $^{28}$Si, are also indicated.

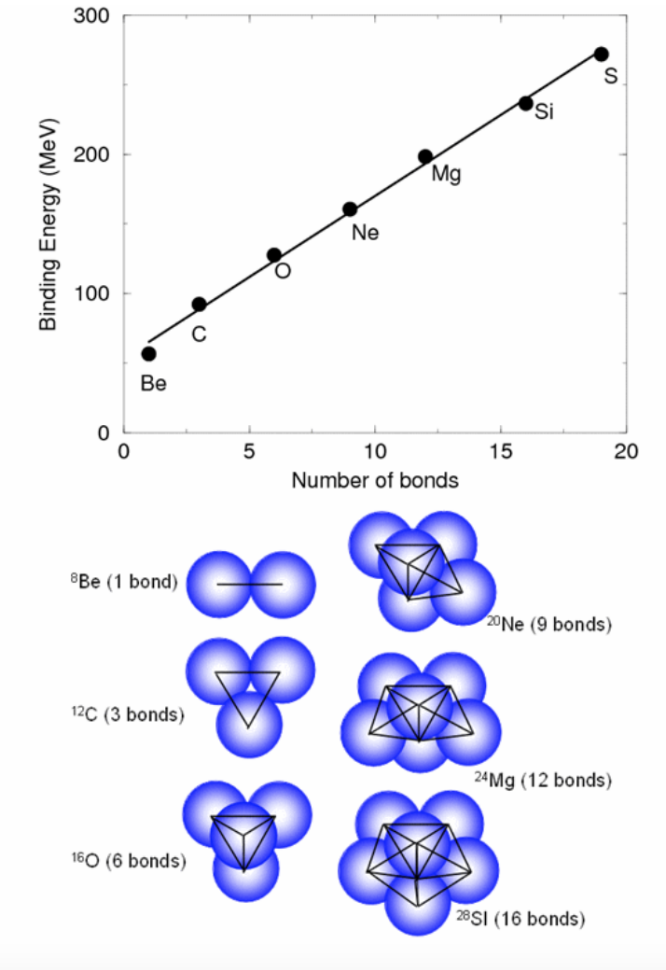


Figure 1.2: (Top) Binding energies of light $\alpha$-particle nuclei as a function of bonds between the alpha-particles. (Bottom) Proposed arrangements of the $\alpha$-particles.

It is important to acknowledge that the perspective of the resilience of the $\alpha$-particle in the ground states of these nuclei is no longer widely accepted, as it is now believed that the cluster structure is typically diminished in most ground states. Nevertheless, these concepts played a significant role in laying the foundation for what came next: Brink

[5] utilized the geometrical model for the excited states of these nuclei as reported in Figure 1.3.

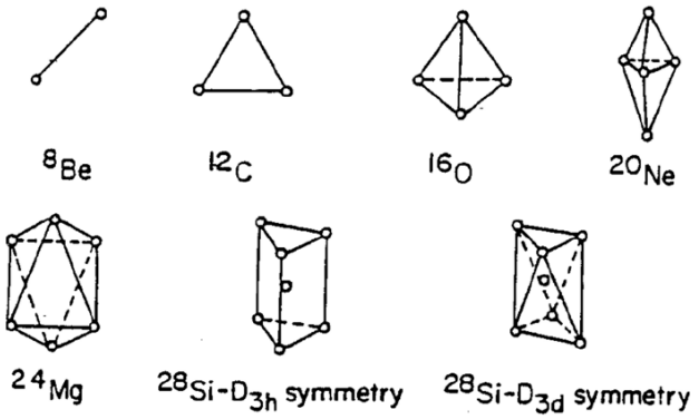


Figure 1.3: Geometric $\alpha$-particle structures predicted by Brink [5]. Note that the arrangements reflect the number of possible bonds between $\alpha$-particles predicted by Hafstad and Teller [29].

Significant progress supporting the idea of $\alpha$-particle condensation in nuclei arises from the accurate theoretical depiction of the Hoyle state (the initial $0^+$ excited state at 7.654 MeV in $^{12}$C) and the $0_6^+$ state at 15.097 MeV in $^{16}$O, utilizing wave functions of the condensate type [7, 8]. The Hoyle state case is particularly interesting since both shell-model and no-core shell model calculations struggle to describe it. It is characterized by a gas-like arrangement of three $\alpha$-particles, predominantly occupying the lowest S orbit. This is supported by the simultaneous emission of three $\alpha$-particles with minimal dispersion in kinetic energy. Recent Fermionic Molecular Dynamics (FMD) calculations [9] allow for an innovative interpretation of the Hoyle state's structure, suggesting it is a blend of different pre-formed $\alpha$-configurations.

The "modern" era of nuclear clustering was catalyzed by the ideas of Morinaga in 1956, who had hypothesized that the 7.654 MeV Hoyle state in $^{12}$C might be a linear arrangement of 3$\alpha$-particles [10]. The concept that linear chain structures might exist in nuclei stuck with the subject until present days and remains to be resolved. Figure 1.4 shows the possible arrangement of the $^8$Be and $^{12}$C particles. The pursuit of experimental evidence for the structures envisioned by Morinaga and those calculated by Brink using the Bloch-Brink $\alpha$-cluster Model [11] has significantly driven research in this direction. For example, in the case of $^{12}$C, the $\alpha$-cluster model finds two structures: the first is an equilateral triangular arrangement which historically has been associated with the ground-state, and the second is a linear arrangement (or chain).

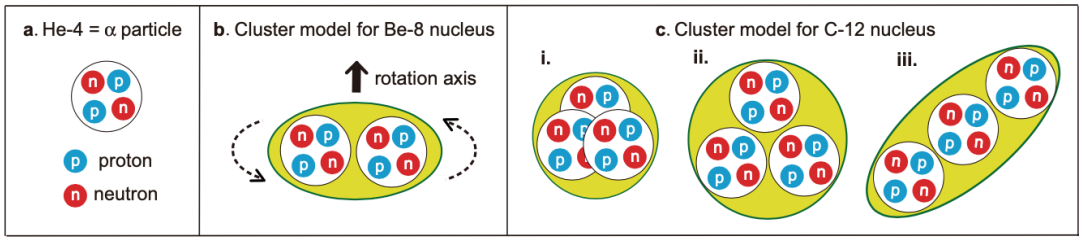


Figure 1.4: Schematic illustrations of $\alpha$ clustering in atomic nuclei. a. $^{4}$He=$\alpha$ particle, b. $^{8}$Be, and c. $^{12}$C (three possible cases, i, ii, and iii). The green areas represent atomic nuclei allowing some movements of $\alpha$ clusters [12].

In the 1960s it becomes clear that the cluster should not be evident in the ground state but it starts to emerge as the internal energy of the nucleus increases [8]. In essence, the cluster structure is anticipated to become visible near, and possibly slightly below, the cluster decay threshold. Namely, the ground band states of $^{8}$Be, the excited states of $^{12}$C with the well-developed 3$\alpha$ molecular structure, the states of $^{16}$0 with $\alpha$ + $^{12}$C structure, and the $^{20}$Ne states with $\alpha$ + $^{16}$O structure, exist near or above the respective threshold energies of the dissociation into clusters. This empirical rule regarded as a necessary condition for the formation of the molecule-like structure was called *threshold rule*. Consequently, it is necessary for a nucleus to have the energetic feasibility to embrace a cluster structure.

Asymptotically, when the nucleus is split into its cluster constituents, an energy equivalent to the mass difference between the host nucleus and the clusters must be supplied. Dissociation energy of a saturating nucleus into several saturating fragment nuclei is small due to the overall saturation property of the nuclear system. Therefore the appearance of the molecule-like structure near the threshold energy means that the structural change into the molecule-like structure occurs by an input of a small amount of energy.

The preservation of the identity of interacting clusters gives rise to the repulsive core effect in the short-range segment of the inter-cluster interaction, as a consequence of the Pauli exclusion principle acting between clusters. Consequently, the transformation of the structure is attributed to the interconnected dynamic interplay between correlation characteristics and the Pauli principle.

To demonstrate the potential for diverse structural changes in nuclei, a diagram known as the *Ikeda diagram* [13], shown in Figure 1.5, was introduced for $\alpha$-nuclei. This diagram depicts various dissociation patterns of $\alpha$-nuclei into fragment $\alpha$-nuclei at their respective threshold energies, as a function of energy and mass number.

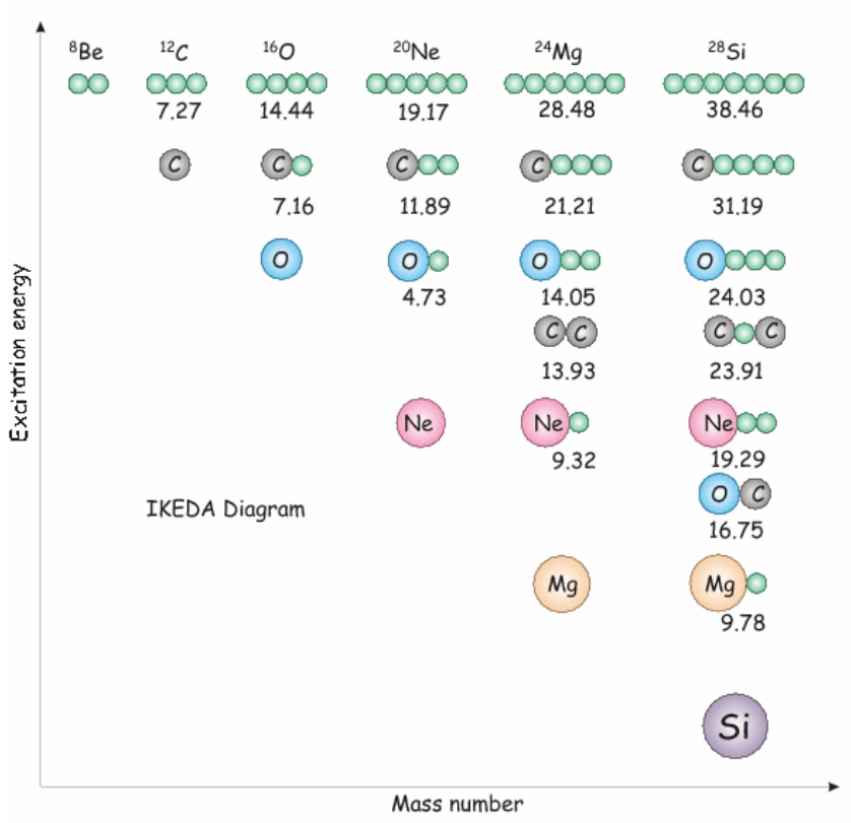


Figure 1.5: The Ikeda diagram [13] which shows the subunits of the possible molecule-like structures expected to appear near the respective threshold energies for the break-up into subunit nuclei. The threshold energies (in MeV) are indicated.

This diagram shows the possible $\alpha$-cluster decompositions of light self-conjugated nuclei in correspondence of each decay threshold. It is evident that the $\alpha$-cluster serves as a fundamental building block for structural changes since the $\alpha$-particle is the smallest saturated nucleus. Ikeda postulates the existence of a gradual transition from the compact ground state to the fully N-$\alpha$ clustered structure. The $\alpha$-particle configurations are here shown schematically as linearly arranged, even if that is not the most stable configuration [14]. Additionally, the structural phase of N-$\alpha$-clusters is positioned at the diagram's upper excitation energy limit, while the spatially compact shell-model-like structure near the ground state is situated at the lower limit. In the transitional region between these two structural phases, one can anticipate the formation of molecule-like structures through various combinations of elemental clusters. The diagram suggests that the cluster's degree of freedom is only liberated while the excitation energy of the system approaches the one of the cluster emission threshold. As an example, while $^{8}$Be has a strongly clustered structure in its ground state, which is located at about 0.0918 MeV from the 2-$\alpha$ threshold, an excitation energy of about 7.27 MeV is suggested to search for the 3-$\alpha$ structures in

$^{12}$C.

An analysis of experimental data through coupled channels [15] verifies the theoretical predictions [7] that estimate the root mean square (rms) radius of the Hoyle state to be 45% larger than the radius of $^{12}$C in its ground state. This can lay the foundation to a possible validation of the conjecture that $\alpha$-particle condensation is a characteristic feature of medium-size self-conjugated 4-N nuclei whose excitation levels are close to the N-$\alpha$ decay threshold.

## 1.3. Techniques for the study of clusters in nuclei

Clustering phenomena in light nuclei can be experimentally probed by investigating their spectroscopy, consisting in the knowledge of the characteristics of its excited states, as the excitation energy $E_x$. These information can be obtained by means of different types of experiments which involve nucleus-nucleus collisions at intermediate energies.

Specifically, these experiments fall into a class of nuclear reactions of particular interest for clustering: the so-called *direct reactions*. As the bombarding energies rise, this category of reactions grows in significance, playing a crucial role in revealing the structure of nuclei below and above the cluster decay thresholds. *Transfer reactions* and *breakup reactions* are particularly pertinent to this objective. The duration of interaction corresponds to the time it takes for the incident particle to cross the nuclear diameter of the target, usually around the magnitude of $10^{-22}$ seconds, much shorter than the time required for a system to form a compound nucleus. Another crucial characteristic of direct reactions is the absence of a mechanism to substantially change the momentum direction carried by the incident particle. In fact, direct reactions involve few (or just one) collisions, resulting in a pronounced asymmetry of angular distributions. As a result, the direction of the emitted particles is strongly correlated with the direction of the incident momentum, leading to a pronounced peak in the forward direction.

The analysis is pointed out on *Breakup reactions*, since they are the class of direct reactions which allow to investigate the possible presence of states characterized by $\alpha$ clustering above the emission threshold. They consist in the excitation of a nucleus by means of the interaction with another nucleus (via inelastic scattering or transfer primary mechanisms) above the particle decay threshold, and the subsequent de-excitation of the excited nucleus via particle emission. Projectile breakup and target breakup are distinguished based on whether the nucleus undergoing final disintegration is the projectile or the target in the collision, respectively. The choice between the two depends on the experimental setup employed to detect the emitted fragments. For instance, in a target breakup reaction,

the breakup products are emitted in a large, nearly isotropic cone with low energies. This is due to the diminished boost from the nearly stationary target after the reaction. Conversely, in a projectile breakup reaction, the breakup fragments are typically forward-focused, propelled by the boost from the projectile, and exhibit higher energies. Additionally, a distinction is made between sequential and direct breakup. In the latter, the nucleus undergoes sudden disintegration due to the forces arising from the density gradient during its interaction with the target [16]. In such cases, breakup fragments do not provide substantial information about the spectroscopy of the emitting nucleus. Conversely, sequential breakup reactions are frequently employed to investigate the structure of nuclei. These reactions follow a two-step process where the nucleus is initially excited through interaction with the target and then undergoes asymptotic (sequential) breakup as part of the de-excitation process. The spectroscopy of the nucleus prior to decay can be inspected by measuring masses and momenta of the outgoing particles. Let us assume a sequential breakup reaction of the type:

$$X + Y \Rightarrow X^* + Y \Rightarrow \sum_{i=1}^{N} x_i + Y \tag{1.1}$$

where the $N$ breakup fragments $x_i$ of masses $m_i$ are emitted by the intermediate resonance $X^*$. The quadri-momentum of the i-th fragment will be:

$$q_i \equiv (x_i^0, x_i^1, x_i^2, x_i^3) = (E_i, p_i^x, p_i^y, p_i^z) \tag{1.2}$$

where we used its covariant components and we assumed c = 1. The usual vector $(p_i^x, p_i^y, p_i^z)$ is the momentum of the i-th fragment, while the first component of the quadri-vector represents its total energy $E_i = \sqrt{\bar{p}_i^2 + m_i^2}$. The total quadri-momentum then will be: $q = \sum_{i=1}^{N} q_i$.

From the definition of the total energy, it is possible to obtain the mass on the laboratory frame (L.F.):

$$^{\text{L.F.}}m_i^2 = \sum_{i=1}^{N} {}^{\text{L.F.}}E_i^2 - \sum_{i=1}^{N} \bar{p}_i^2 \tag{1.3}$$

.

Placing on the centre of mass frame (c.o.m.), the Equation (1.3) can be rewritten as:

$$s = {}^{\text{c.o.m.}}m_i^2 = \sum_{i=1}^{N} {}^{\text{c.o.m.}}E_i^2 \tag{1.4}$$

The quantity $\sqrt{s}$ is called *invariant mass* and it is a relativistic invariant quantity, i.e. a quantity which is independent on the reference frame. It represents the mass of the particle which emitted the N fragments leading to the quadri-momentum $q$.

The excitation energy of $X^*$ before decay is simply the difference between its invariant mass and the mass of the ground state $X$:

$$E_x = \sqrt{s} - m(X) \tag{1.5}$$

The Equation (1.5) allows to obtain information on the energy position of excited states populated in a breakup reaction. This technique is called *multi-particle correlation* and is particularly sensitive to cluster configuration, since they have pronounced decay widths for the emission of constituent clusters.

When a resonant state undergoes decay through the emission of more than two fragments, employing multi-particle correlation techniques allows for the examination of the decay path of the state. A simple example is the decay of a resonance in three equal-mass particles.

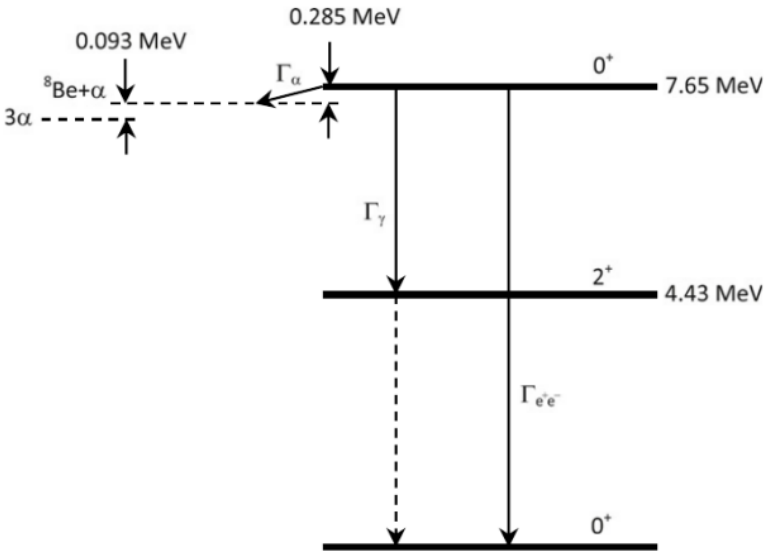


Figure 1.6: Scheme of low-lying states of $^{12}$C. The Hoyle state (7.654 MeV, $0^+$) is shown together with the corresponding $3\alpha$ and $\alpha$ +$^8$Be decay thresholds. The $^{12}$C(7.654) $\Rightarrow$ $\alpha$ +$^8$Be decay and the possible electromagnetic transitions to the ground state are shown [3].

In such a case, as for the Hoyle state in $^{12}$C, shown in the Figure 1.6, one can expect

direct resonance decays of the type $X^* \Rightarrow y_1 + y_2 + y_3$ or sequential decays, where a two-step process occurs: $X^* \Rightarrow y_1 + Y^* \Rightarrow y_1 + y_2 + y_3$. The two mechanisms of decay of $^{12}$C are presented in Figure 1.7. If they are the sole two ways for the resonance decay, the partial width of the decay will be the sum of the direct and the sequential ones: $\Gamma_{y1+y2+y3} = \Gamma_{direct} + \Gamma_{sequential}$.

In the case of sequential fragmentation through $^8$Be, the two $\alpha$ particles that result from its decay must be correlated in angle, and this can be used as an experimental signature to distinguish this channel.

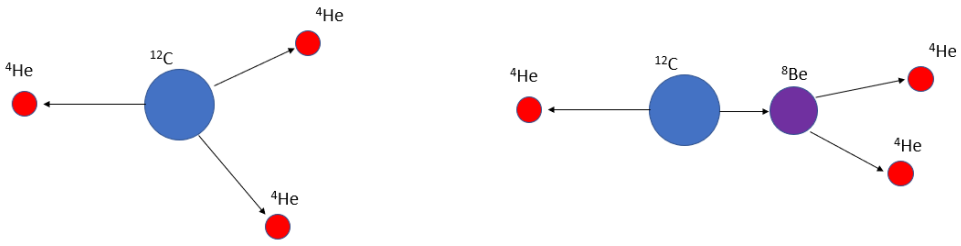


Figure 1.7: Scheme of possible decay processes for $^{12}$C in the c.o.m. frame.

The symmetric Dalitz plot, introduced by Dalitz [17] in the context of particle physics, can be used to geometrically visualize both decays and to extract their amplitudes. It can be built by using the kinetic energy of the three particles $E_{i,j,k}$ in the reference frame where the parent nucleus $X^*$ is at rest. The Dalitz plot coordinates, which are called *normalized decay energies*, can be defined as follows:

$$\epsilon_{i,j,k} = \frac{E_{i,j,k}}{(E_i + E_j + E_k)} \tag{1.6}$$

They can be used as coordinates of a system of axes like the one in Figure 1.8. Since the sum of each of the coordinates is a constant, experimental points, corresponding to $(\epsilon_1, \epsilon_j, \epsilon_k)$ energy coordinates, are therefore localized inside the triangle in the figure. Furthermore, from the energy conservation in the decay we must have $(\epsilon_1 + \epsilon_j + \epsilon_k = 1$, which results in a constraint that confines the data into the green circle. In the case of direct decays, according to the phase space available, the energy can be shared with any of the possible combinations $\epsilon_{i,j,k}$ and the circle is almost uniformly filled. For the case of sequential decays, instead, the energies of the decay have to obey to more restrictive constraints.

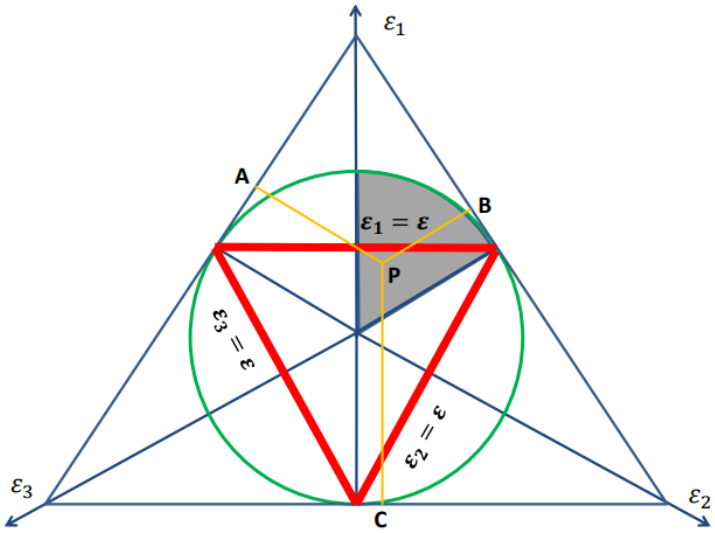


Figure 1.8: A schematic view of a symmetric Dalitz plot. The three axes correspond to the normalized energies of the three particles in their decay center of mass $\epsilon_{i,j,k}$. The conservation of energy $\epsilon_1 + \epsilon_j + \epsilon_k = 1$ results in the data to collapse inside the green circle. The red straight lines correspond to the three loci occupied by the data if, for example, the decay occurs in a two-steps process (sequential).

## 1.4. Experimentally Observed Clusters in $\alpha$-Particle Nuclei at low energies

As described in the previous section, the $\alpha$-clustering scenarios are observed when two heavier nuclei collide head on at c.o.m. with energies around the Fermi energy. The nuclei first fuse and compress. Then decompress and at sufficiently low density the system breaks up into clusters [18].

The idea has been followed by Raduta [19], whose study consists in the production of excited states candidates to $\alpha$-particle condensation. The experiment has been performed through the use of fragmentation of quasi-projectiles from the nuclear reaction $^{40}$Ca + $^{12}$C at 25 MeV/nucleon.

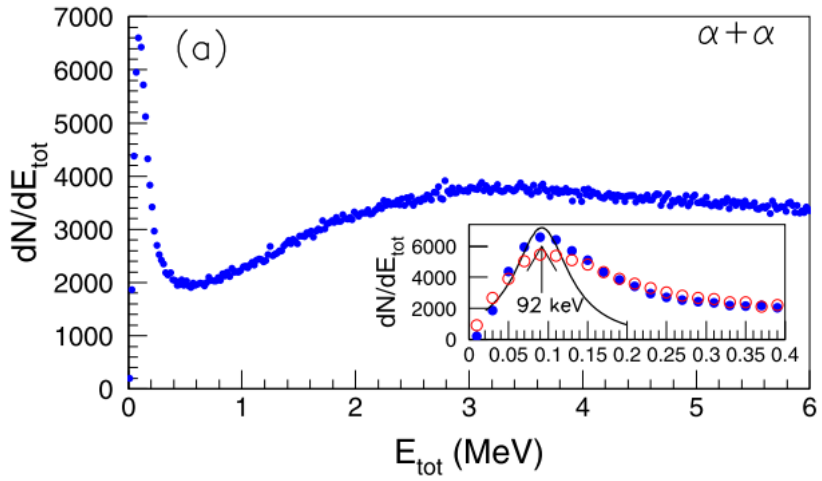


Figure 1.9: Yields of correlated $\alpha - \alpha$ emissions out of quasi-projectile expressed as a function of total kinetic energy. The inset corresponds to zooms on the $^{8}Be_{g.s.}$ peak [19].

The Figure 1.9 represents the correlated spectra as a function of total kinetic energy in the c.o.m. of the two particles. The $\alpha - \alpha$ spectrum shows a narrow peak centered at 92 keV ($\Gamma$ = 84 keV) and a much broader peak centered at around 3 MeV. The first peak corresponds to the ground state of $^{8}$Be ($Q$ = -92 keV) with $\Gamma^{exp}$ = 5.57 eV and the second one to the first excited state at 3.03 MeV ($\Gamma^{exp}$ = 1.5 MeV). The energy levels of $^{8}$Be are shown in Figure 1.10

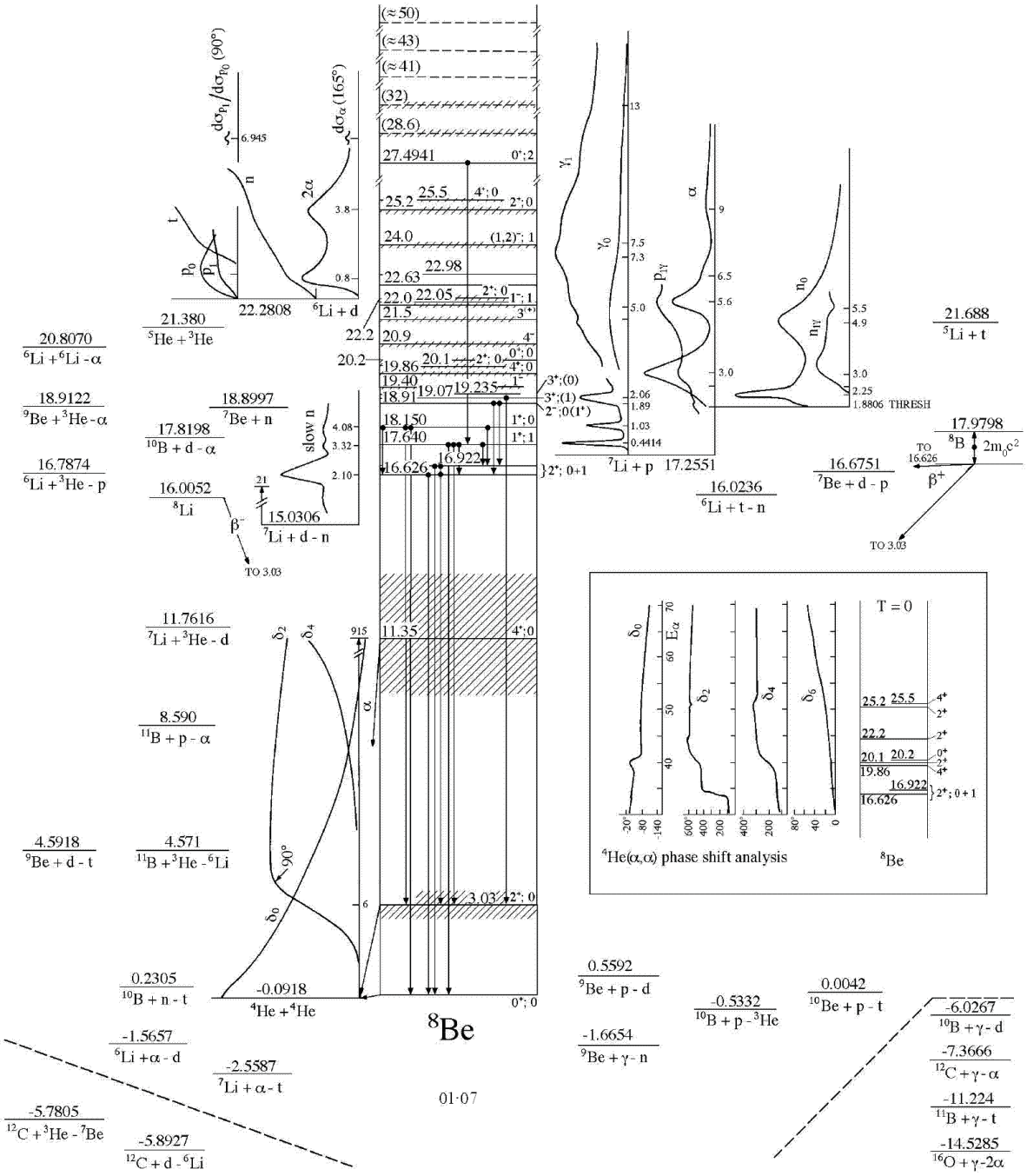


Figure 1.10: Energy levels of $^{8}$Be [20]

Information on the $\alpha$-particle unstable excited states of $^{12}$C populated by the $^{40}$Ca + $^{12}$C at 25 MeV/nucleon reaction may be extracted from the 3$\alpha$ correlation functions. The correlated spectra is shown in Figure 1.11.

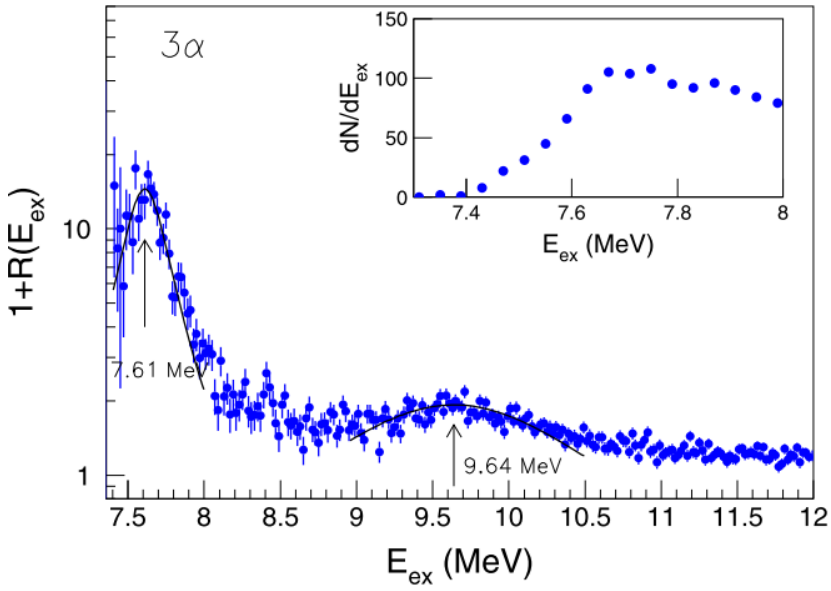


Figure 1.11: $3\alpha$ correlation function as a function of excitation energy. The arrows correspond to centroids of Breit–Wigner distributions (solid lines). Inset: zoom of the correlated spectrum in the energy domain of the Hoyle state [19].

Two peaks centered at $E_x = 7.61$ MeV ($\Gamma = 0.33$ MeV) and $E_x = 9.64$ MeV ($\Gamma = 1.14$ MeV) emerge. The first peak corresponds to the Hoyle state ($E_{x-exp} = 7.654$ MeV, $\Gamma_{exp} = 8.5$ eV), while the second one is due to the complex region of excitations, characterized by the strong $E_{x-exp} = 9.64$ MeV ($\Gamma_{exp} = 34$ keV), $3^-$ state and by the broad $E_{x-exp} = 10.3$ MeV, $0^+$ state submerging a possible $2^+$ state at 9.7 MeV.

It has been demonstrated so far that the $^{40}$Ca + $^{12}$C nuclear reaction at 25 MeV/nucleon populates excited states of $^{12}$C nuclei which decay by $3\alpha$ emission.

A similar analysis is reported by Morelli [21] which has studied the reaction $^{12}$C + $^{12}$C with a 95 MeV Carbon beam delivered by the Tandem accelerator of INFN Laboratori Nazionali di Legnaro (LNL) with the GARFIELD + RCo apparatus covering approximately $4\pi$ [22]. Events where three $\alpha$-particles are detected in the forward cone (RCo) have been selected.

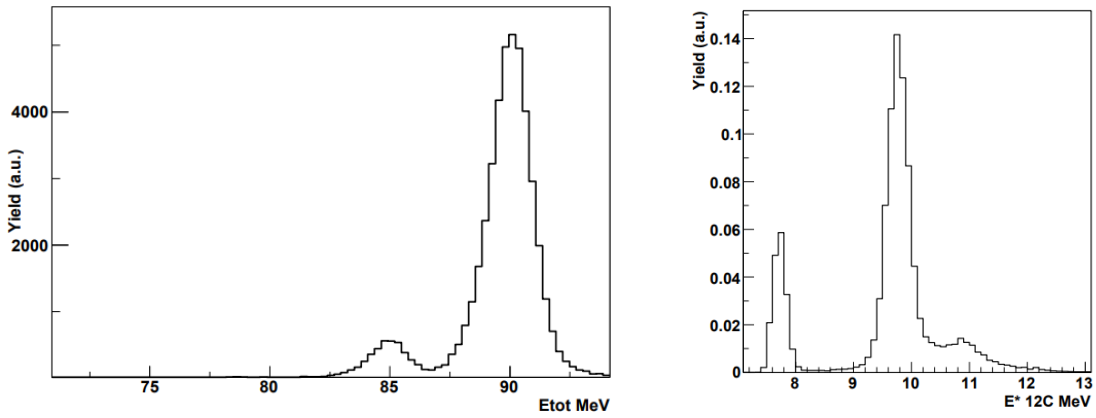


Figure 1.12: (Left) Total energy spectrum for $\alpha$-particles products. From right to left the peaks correspond to the ground and the first excited states of the recoil $^{12}$C nucleus. (Right) Excitation energy spectrum for the breakup of $^{12}$C into three $\alpha$-particles [21].

In Figure 1.12, on the left panel, the energy spectrum of the reconstructed $^{12}$C quasi-projectile is shown, as calculated from the sum of the energy of the three $\alpha$-particles. Most of the kinetic energy is peaked at $\sim$ 88 MeV and a small peak is present at $\sim$ 84 MeV, corresponding to the $^{12}$C quasi-target at $\sim$ 4.4 MeV excitation energy, which is the first $^{12}$C excited level. On the right panel the plot of excitation energies plot is reported where it is clearly visible the well-known Hoyle state.

Moreover, the study has been proposed to determine whether the decay of the excited state of the $^{12}$C is instantaneous or sequential through the formation of $^{8}$Be$_{\text{g.s.}}$. The analysis is performed through the Dalitz plot of the energies of the three $\alpha$-particles normalized to the total energy proposed in Figure 1.13.

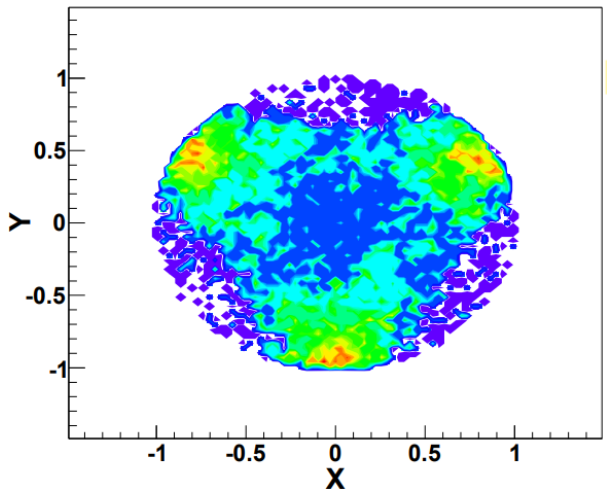


Figure 1.13: Energy Dalitz-plot normalized to the total energy [21].

It is expected that the simultaneous decay would yield three equal kinetic energies, leading to an increase in the central portion of the plot. On the contrary, it shows enhancements in the region where the energies of two $\alpha$-particles are very close to one another and the third $\alpha$-energy is far from the other two. This observation can be interpreted as an indication of the significance of sequential decay.

## 1.5. Experimentally Observed Clusters in $\alpha$-Particle Nuclei at intermediate energies

In the previous section are described experimental techniques to demonstrate the production of clusters through nucleus-nucleus collisions at energies around the Fermi energy. The next analysis aims to achieve the same objectives but at higher energies, characteristic of the Multi-fragmentation phenomena, as shown in the orange part of the graph in Figure 1.14.

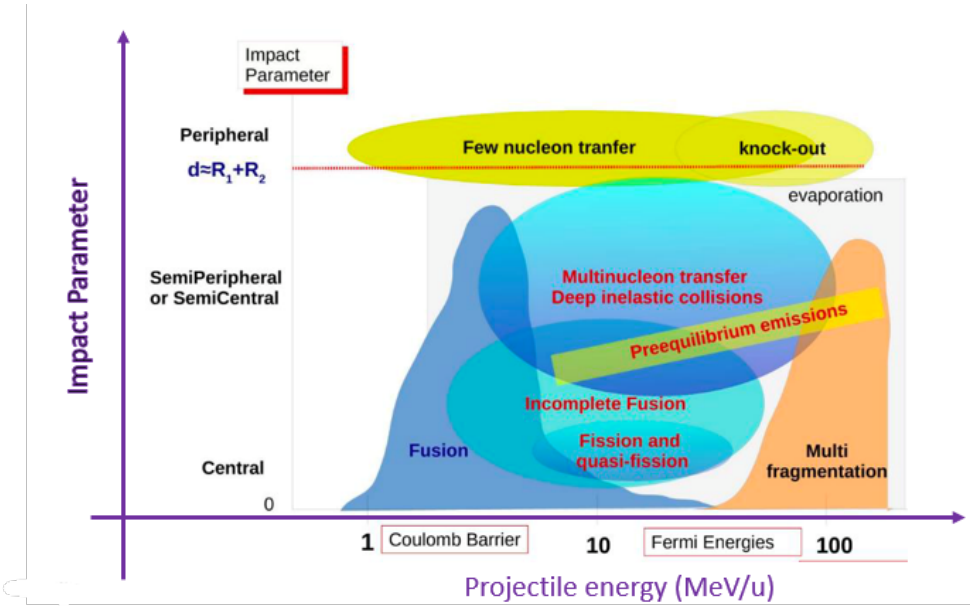


Figure 1.14: Nuclear phenomena and their corresponding energies [23].

The analysis is applied in the study of the carbon ion fragmentation with emulsion technology at NIRS-HIMAC in Japan for 200–400 MeV/nucleon $^{12}$C in water [24]. It has been studied the production of $^{8}\mathrm{Be}_{\mathrm{g.s.}}$ in Carbon ion interactions. Since the $^{8}\mathrm{Be}_{\mathrm{g.s.}}$ is an unstable isotope of Beryllium which decays into a pair of $\alpha$ particles with a life time in the order of 10-16 s and a Q-value of 90 keV, the opening angle of the $\alpha$-pair is expected to show a peak close to zero. When $^{8}\mathrm{Be}_{\mathrm{g.s.}}$ is produced as a projectile-like fragment, its

velocity is equal to that of the primary carbon ion within a few percent error. The fragment promptly decays into two forward-going $\alpha$ particles with a maximum opening angle of 0.013 rad. This angle is due kinematically to the mass difference of 92 keV between $^{8}\mathrm{Be}_{\mathrm{g.s.}}$ and two $\alpha$ particles. For this reason it has been analyzed the angular correlation between the light fragments.

Figure 1.15 shows the measured distribution of opening angles between two Helium particles. It is considered any combination of two helium particles for each event. A prominent peak at $\Delta\Theta_{\alpha-\alpha} \sim 0.01$ corresponds to the expected value for the fragments originating from the decays of the $^{8}\mathrm{Be}_{\mathrm{g.s.}}$.

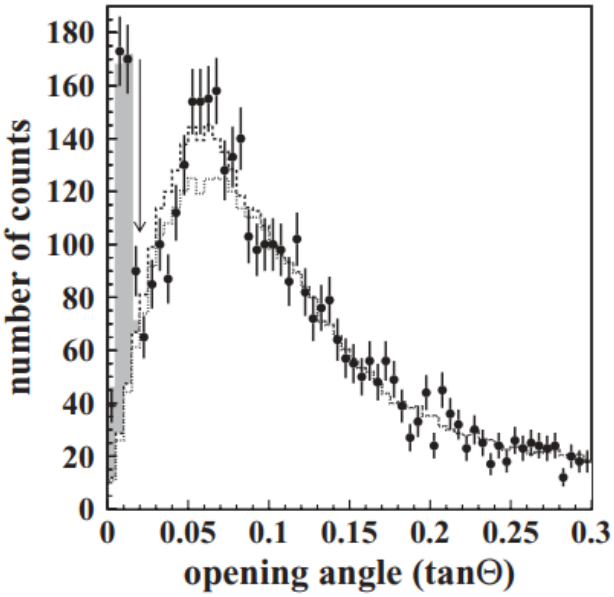


Figure 1.15: Opening angle between two helium particles $\Delta\Theta_{\alpha-\alpha}$. (Black dots) Data and statistical errors. The cut point to select $^{8}\mathrm{Be}_{\mathrm{g.s.}}$ events is indicated by the arrow. (Dotted histogram) Background events with best fit parameters. (Dashed histogram) The sum of $^{8}\mathrm{Be}^{*}_{3.04}$ and background events with best fit parameters. (Gray histogram) $^{8}\mathrm{Be}_{\mathrm{g.s.}}$ events with best fit parameters [24].

The same analysis was reported by De Lellis [25] by exposing the Emulsion Cloud Chamber to a beam of Carbon nuclei with 400 MeV/nucleon at HIMAC (Heavy Ion Medical Accelerator in Chiba) at NIRS (National Institute of Radiological Sciences) in Chiba (Japan). The histogram on the left of Figure 1.16 shows the opening angle of two Helium nuclei: an excess of events is visible below 20 mrad to prove the existence of an angular correlation between $\alpha$ particles. On the contrary, no peak is visible when the opening angle of H-He is plotted (histogram on the right). The latter is the counterproof that

angular correlation appears only in case of $\alpha$-pair production from the $^{8}$Be decay.

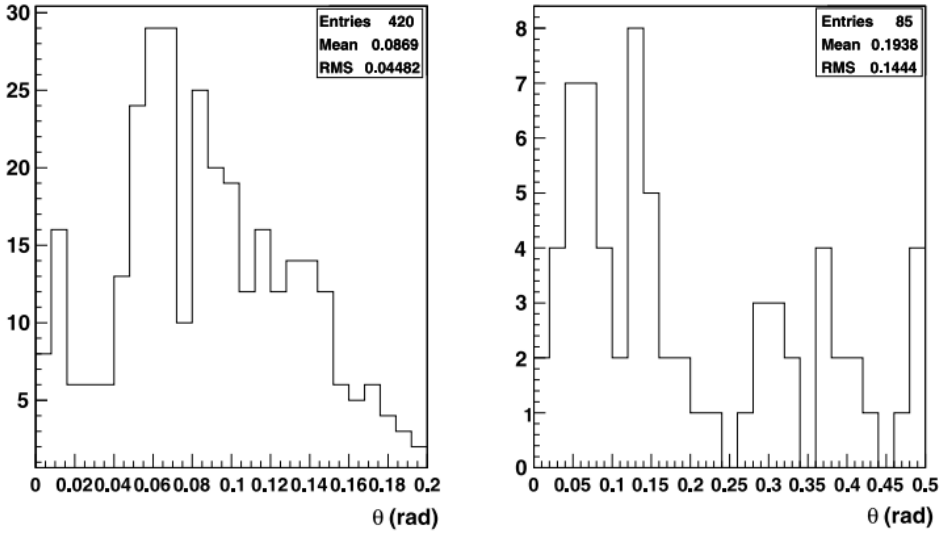


Figure 1.16: (Left) Opening angle between pairs of reconstructed Helium tracks. A peak is visible below 20 mrad. (Right) No peak is visible in the distribution of the opening angles between Helium and Hydrogen [25].

At this point of the $\alpha$ clustering state of art comes naturally to consider new experiments at intermediate energies that allow further investigation on this topic. In the following chapters, it will be considered the possibilities offered by the INFN's FOOT experiment to explore the correlation evidence between $\alpha$ particles generated by the projectile fragmentation beyond 150 MeV/u.

# 2 | The FOOT Experiment of INFN

## 2.1. Introduction

The FOOT (FragmentatiOn Of Target) experiment is inserted in the context of particle therapy (PT) and radiation protection in space (RPS) within the field of nuclear physics. It was founded in 2017 by the Italian National Institute for Nuclear Physics (INFN) with the main goal of measuring the fragmentation double differential cross sections in angle and energy ($d\sigma/d\Omega \cdot dE$) of particles involved both in PT and space radiations. In particular, the experiment aims to measure the fragmentation of H, $^{4}$He, $^{12}$C and $^{16}$O at energies of interest for PT and RPS on different targets, mainly C, H and O.

Two different experimental setups have been developed in the project due to the different measurement requirements. The first one is an electronic spectrometer composed by different sub-detectors optimized to detect heavy fragments ($Z \geq 3$) which are emitted in a forward cone, typically within 10 degrees at the energies of interests. The second one is an emulsion spectrometer based on the emulsion technology to detect the light fragments ($Z \leq 3$) in a wider angular range.

The goals of FOOT are detailed in Section 2.2 while in Section 2.3 is highlighted how the $\alpha$ clustering study can be addressed by the experiment. In Section 2.4 the measurement strategies are investigated on the basis of the different applications. A comprehensive presentation of both apparata is given in Section 2.5, followed by the description of the expected experimental performances in Section 2.6.

## 2.2. Purposes of the experiment

The FOOT experiment has been designed to investigate the nuclear fragmentation processes involved both in Charged Particle Therapy (PT) and radiation protection in human spaceflight applications [26].

In Charged Particle Therapy, light ion beams (like proton or $^{12}$C beams) are used to treat deep-seated solid tumors exploiting the advantageous characteristics of charged particles energy deposition in matter [27]. By using these particles as projectiles, the maximum dose is delivered at the end of the beam's range, specifically within the region where the tumor resides [28]. However, it is crucial to consider the potential impact of the fragmentation of the projectiles and/or target nuclei when planning the treatment. Indeed, when the beam particles interact with atomic nuclei inside the patient's body, they can undergo fragmentation, generating secondary particles with reduced atomic numbers (Z). The majority of the produced fragments are emitted forward with a velocity comparable to that of the projectile. These fragments possess a longer range, leading to an energy loss extending beyond the planned region. Furthermore, the lighter fragments, notably notably fragments with A=1 and A=2, may be emitted at wide angles in relation to the beam's direction. The fragmentation processes alter the delivered dose distribution compared to what can be calculated by considering the sole contribution of primary ions [29]. The effects of nuclear fragmentation in PT vary based on the types of particles employed (whether protons or hadrons). In the case of proton treatments, target fragmentation results in the generation of low-energy, short-range fragments that deposit a notable dose, particularly in the tissues initially encountered along the beam path. Conversely, when employing $^{12}$C or other ions like $^{4}$He or $^{16}$O, long-range fragments are generated, which can release their dose into healthy tissues situated beyond the tumour region. Treatment plans, typically based on deterministic codes and validated against Monte Carlo (MC) simulations [30], currently cannot incorporate the fragmentation component with the level of accuracy (3%) recommended for radiotherapy applications [31, 32]. This results from the poor experimental data, in particular of double-differential cross-sectional measurements with respect to the angle and the kinetic energy [33].

The charged ions radiation effects are also of great interest in the framework of radioprotection in space since the particles involved in the galactic cosmic radiations are the same adopted in PT, even thought they possess a completely different energy range (their energy spectrum extend into the GeV and TeV range). The fragmentation process has to be taken into account during the spacecraft shield design since the produced secondary fragments contribute to the dose release to astronauts and to the damage of the electronic

systems and instrumentation [34, 35]. The measurement of the nuclear fragmentation cross section for the interaction of the Galactic Cosmic Rays (GCR) with different types of shielding material is necessary to validate the MC simulation results, so that the estimation is correctly assessed [36].

## 2.3. The study of nuclear clustering in FOOT

Although FOOT was developed for the applications described in Section 2.2, there is the opportunity to investigate the $\alpha$ clustering processes which have been poorly modeled at the energies involved in the experiment.

The main purpose of this study is to provide a experimental evidence of the $\alpha$ clusterization phenomena in nucleon induced reactions for incident intermediate energies (beyond 150 MeV/u).

A nuclear collision at intermediate energies may be pictured as a series of different physical scenarios. Before the collision the projectile and target are in their ground states. After the contact they interpenetrate and a highly excited and compressed zone is created. Subsequently expansion and cooling occur, leading to the formation of exited fragments that further evolve and deexcite while departing from the collision zone. To develop a dynamical theory that includes these scenarios is a difficult task and so far no single model has been able to adequately describe all three stages.

One of the most difficult issues is related to the fact that this energy region is a transition region between a mean-field dominated dynamics (much below the Fermi energy) and a high-energy regime where individual nucleonic degrees of freedom and associated two-body effects become predominant.

In this framework, FOOT measured and analyzed data could be of help modelling physical phenomena not yet investigated, expanding in the field of applications of the experiment.

## 2.4. Strategy of measurements

The FOOT experiment has been designed to detect, track and identify all the charged fragments produced in ion collisions with different targets, with the aim of performing precise measurements of both projectile and target fragmentation.

For the target fragmentation, the differential cross section with respect to the kinetic energy ($d\sigma/d\Omega \cdot dE_{kin}$) will be measured with the aim to reach an accuracy of about 10%,

while regarding the projectile fragmentation, the double differential cross sections will be measured($d^2\sigma/d\Omega \cdot dE_{kin}$) with an accuracy higher than 5% on the determination of the fragment yields in angle and in kinetic energy.

### 2.4.1. Measurements for PT applications

In the framework of PT projectile fragmentation, FOOT is set to determine the cross-sectional measurements of $^4$He, $^{12}$C, and $^{16}$O beams with typical PT kinetic energies ranging from 200 to 400 MeV/u. These measurements will be conducted using hydrogen enriched targets made of $^{12}$C, $C_2H_4$, and PMMA ($C_5O_2H_8$). Specifically, the measurements of $^4$He and $^{16}$O beams are aimed at assessing the feasibility of introducing these ions into the existing pool of particles used in proton therapy (PT). Additionally, for studies related to target fragmentation, FOOT will determine the cross-sectional data for $^{12}$C and $^{16}$O at 200 MeV/u when interacting with $^{12}$C and $C_2H_4$ targets, employing an inverse kinematic approach.

#### Experimental requirements

In order to match the precision requirements on the final cross section measurements deriving from radiobiological desiderata for PT, the FOOT experiment needs to achieve the following experimental resolutions:

- $\sigma(p)/p \sim 5\%$
- $\sigma(TOF) \sim 200ps$
- $\sigma(E_{kin})/E_{kin} \sim 2\%$
- $\sigma(\Delta E)/\Delta E \sim 5\%$

where p is the momentum, TOF is the Time-Of-Flight, $E_{kin}$ is the kinetic energy and $\Delta E$ is the energy loss.

#### Target material

The choice of the targets for PT applications is driven by the need to replicate the human body's composition, which is primarily composed by oxygen (61%), carbon (23%), and hydrogen (10%) atoms [37]. In the case of carbon ions, it is feasible to create and employ carbon ion targets in the experimental room without complications. However, when it comes to oxygen and hydrogen, the use of pure gaseous and flammable materials poses safety concerns that prohibit their use in accelerator facilities. Furthermore, the

low density of these gases would significantly reduce the interaction rate, rendering the experiment unsustainable. For this reason, the FOOT experiment adopts carbon targets enriched with oxygen and hydrogen particles. The measurements obtained will then be subtracted to the data obtained with pure carbon targets to retrieve the cross-sectional information for pure oxygen and hydrogen targets. As an example, the calculation of the hydrogen cross section measurement is expressed in Equation (2.1) and the results from a previous experiment conducted at Ganil [33] is shown in Figure 2.1.

$$\sigma(H) = \frac{1}{2}(\sigma(CH_2) - \sigma(C)) \tag{2.1}$$

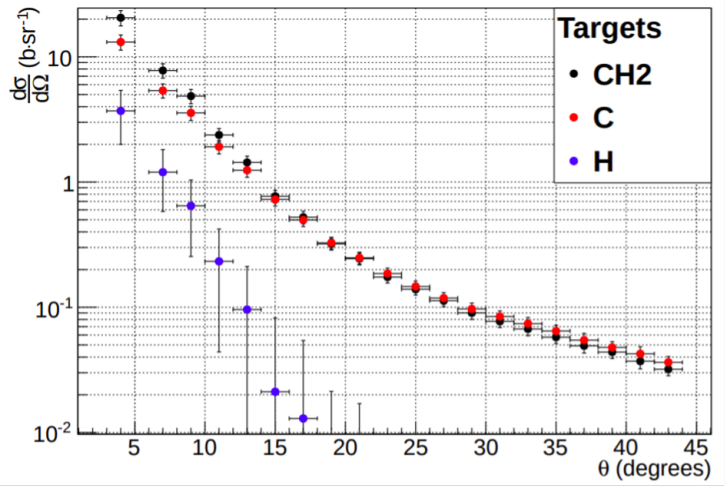


Figure 2.1: Differential cross section measurements of $\alpha$ fragments produced by 95 MeV/u carbon ions on targets of $CH_2$ and $C$. The angular distribution for the hydrogen target is derived by the difference between both, divided by two [33].

In this thesis we have considered a graphite target with a density of 1.83 g/$cm^3$ and a thickness of 5 mm, as the one employed in the preliminary tests of the FOOT experiment. Using a carbon projectile, the percentage of primaries that interact in the target is only 3.645% due to the total reaction cross-section of $^{12}$C against the natural C, which is composed by $^{12}$C and a minor percentage of $^{13}$C, at 200 MeV/u as shown in Figure 2.2.

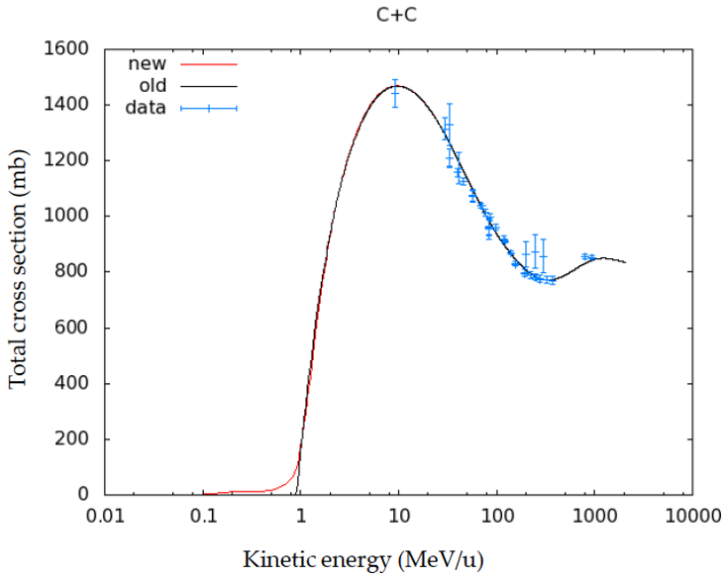


Figure 2.2: Total cross section of C-C reaction function of the energy of the impinging projectile.

## Inverse kinematic approach

Detecting target fragments generated by protons in proton therapy (PT) is a challenging task since they typically possess energies on the order of a few MeV and travel distances on the order of tens of micrometers. For these reasons, the fragments can exit the target material only if they are generated very close to the exit window, typically within the final few micrometers. The idea to minimize the thickness of the target encounters difficulties arising from manageability issues of the target itself. Furthermore, using such thin targets would significantly reduce the nuclear inelastic interactions rate, and the initial kinetic energy of the fragments cannot be accurately measured due to a non-negligible energy loss within the target material. In order to overcome all the difficulties, the FOOT experiment adopts the inverse kinematic approach instead of the direct one. The direct kinematic approach would imply to measure the fragments produced by a proton beam impinging on a tissue-like target made of oxygen or carbon ion. Conversely, the inverse kinematic approach reverses the roles of the projectile and target by impinging tissue-like atoms towards a proton target. This switch results in fragments with enhanced energies and greater travel distances, simplifying their detection. Furthermore, the target can be designed with a thickness on the order of millimeters, increasing the probability of nuclear inelastic interactions without significantly altering the initial kinetic energy of the fragments.

### 2.4.2. Measurements for SRP applications

FOOT will also perform a set of measurements dedicated to the Space Radiation Protection (SPT) with the same primary beams used in PT ($^{4}$He, $^{12}$C, and $^{16}$O) but with higher energies (up to 700-1000 MeV/u) impinging on the same target materials ($^{12}$C, $C_2H_4$ and PMMA).

## 2.5. Description of the experiment

The FOOT experiment has been designed and implemented with two different experimental setups to measure differential cross sections to account for the distinct characteristics of light (Z≤3) and heavy (Z≥3) fragments. As shown in the Figure 2.3 from a FLUKA MC code simulation, the angular distribution of light particles exhibits a wide dispersion, in contrast with heavy fragments that are predominantly emitted within a cone of 10° with respect to the initial particle direction.

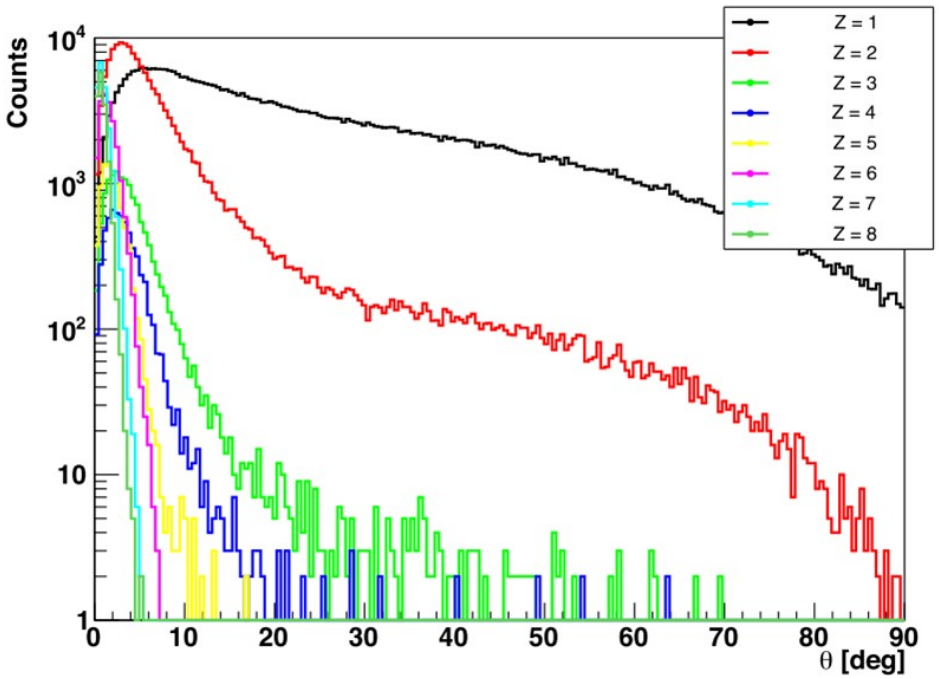


Figure 2.3: Angular distribution of fragments produced by an oxygen beam at 200 MeV/u impinging on a 2 mm thick target made of $C_2H_4$. Data simulated by means of FLUKA.

The first experimental setup is constituted by an *Electronic spectrometer* optimized for the identification of heavy fragments with an angular acceptance of about 10°, while for the second one an *Emulsion Cloud Chamber* (ECC) has been developed for tracking low

Z particles with an angular acceptance of about 70°.

### 2.5.1. Electronic Spectrometer

The development of the FOOT electronic spectrometer aims to identify fragments with Z≥3. This configuration features an angular acceptance of approximately 10°, ensuring the inclusion and detection of all the relevant particles. The entire apparatus can be categorized into three main components:

1. **Upstream region:** is composed of a *Start Counter* plastic scintillator and a *Beam Monitor* drift chamber. These detectors are adopted in the event trigger system, in the Time Of Flight (TOF) measurement system and to reconstruct the incoming primary particle track.

2. **Magnetic spectrometer:** two permanent magnets and a set of tracking detectors (*Vertex detector*, *Inner Tracker* and *Microstrip Silicon Detector*) are placed just beyond the target to reconstruct the fragments' tracks and momenta.

3. **Downstream region:** is composed of a *Tof-Wall scintillator* and a *Calorimeter*. The former is exploited to measure the fragment energy loss $\Delta E/\Delta x$ and, combined with the Start Counter scintillator, provides the particle TOF values. The latter is adopted to measure the kinetic energy.

The overall length of the apparatus is constrained by the available space in the experimental facilities and ranges from 1.5 to 3.5 m depending on the beam's energy. In order to satisfy the experimental requirements highlighted in Section 2.6 relative to $\beta$ and mass resolution, it is required a distance between target and TW of more than 1.5 m, given the TOF resolution of our system. For this purpose the distance for the PT measurements conducted with primaries with a kinetic energy below or equal to 400 MeV/u was set to 1.75 m, at the cost of the geometrical acceptance which is reduced by increasing the distance. For the high energy particle beams (with kinetic energies of about 700 MeV/u or more) dedicated to the SRP data, the downstream detectors are placed at about 3 meters from the target position, increasing the accuracy of the TOF measurement. A schematic view of the electronic spectrometer is shown in Figure 2.4 and in the next paragraphs a complete description of the detectors is presented.

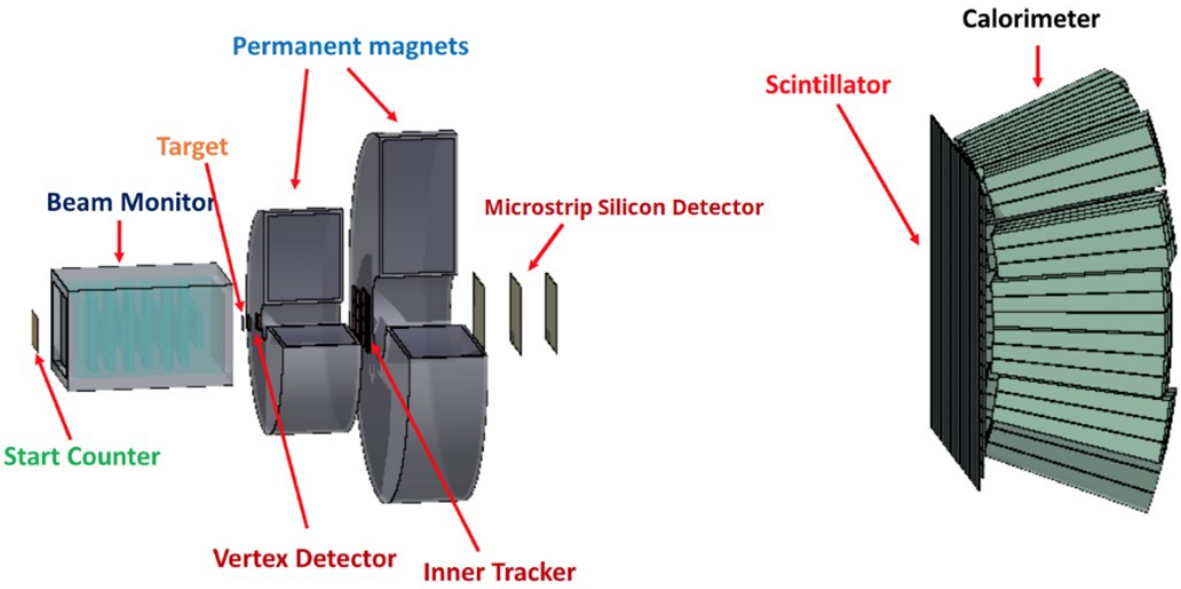


Figure 2.4: Schematic view of the FOOT electronic spectrometer detectors.

## Start Counter

The Start Counter (SC) detector is a plastic scintillator used for multiple purposes, including measuring the incoming ion flux rate, triggering the acquisition system, and establishing the start time for the Time-of-Flight (TOF) measurements performed with the downstream scintillator. Figure 2.5 displays a picture and the technical draw of the SC detector.

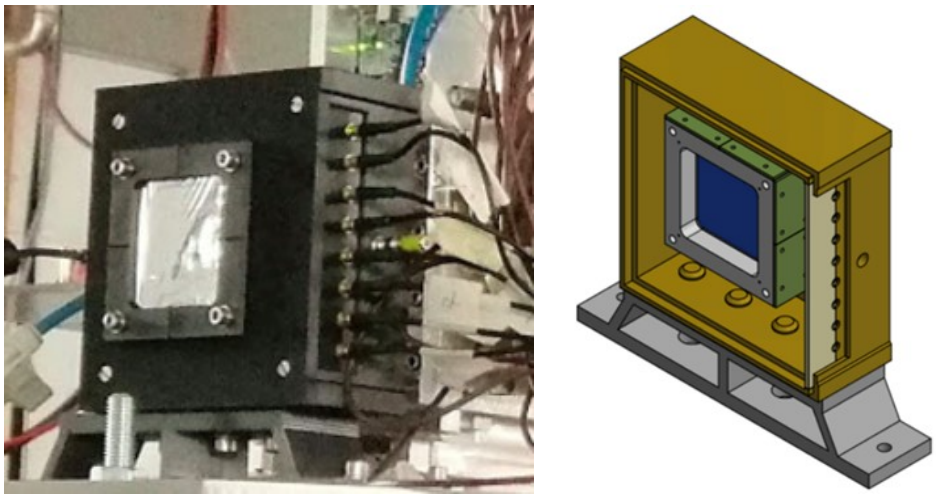

Figure 2.5: A picture (left) and a technical draw (right) of the SC detector.

It is composed by a 250 µm thick, square-shaped ($5 \times 5$ cm$^2$) EJ-228 scintillator foil [38] mounted within an aluminum frame and enclosed in a 3D-printed black housing. This housing features two square windows composed of 4 µm aluminized mylar, aligned with the beam's entry and exit points. The scintillation light is collected on the sides by 48 Silicon Photomultipliers (SiPMs), organized into 8 channels. The readout and powering of the SiPMs is handled by the WaveDAQ system [39]. The maximum signal sampling rate is of 5 Gsamples/s and the dynamic range of 1 V. The incoming signals can be amplified by factors ranging from 0.5 to 100 before digitization, providing versatility to accommodate various projectile energies and species.

The acquired data is analyzed offline with a constant fraction discriminator technique to obtain an accurate event time measurement. This time information is used by the drift chamber detector as reference time and by the downstream scintillator for the TOF measurement.

The detector's performance has been assessed through testing at both CNAO and GSI facilities, involving carbon and oxygen ion beams at different energies. A time resolution of the order of 60ps has been achieved for a $^{12}$C ion beam with a kinetic energy of 700 MeV/u.

## Beam Monitor

The Beam Monitor (BM) is a drift chamber incorporated into both the electronic and ECC setups. Positioned between the SC and the target, its purpose is to determine the incoming beam's direction and the impact point of the primary particles on the target. Additionally, for the electronic spectrometer,it is exploited to reject possible pre-target fragmentation events in the SC and in the BM itself.

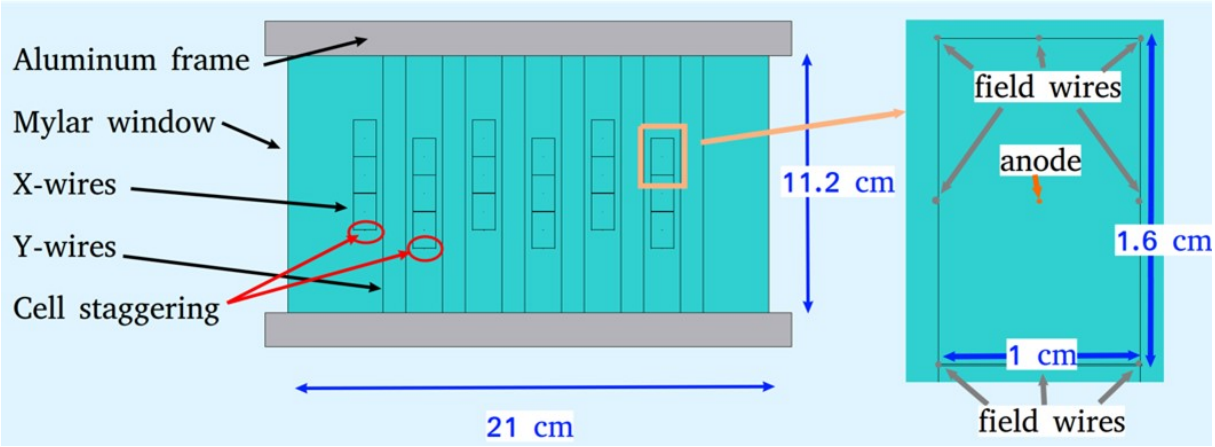


Figure 2.6: Schematic view of the BM detector with a detailed sketch of a BM cell structure.

As shown in Figure 2.6, the BM detector is composed by six layers of cells on both x and y direction (i.e. perpendicular to the z-direction corresponding to the beam line), enclosed by two 100 µm thick mylar films located at the beam entrance and exit. Each layer is made of three rectangular drift cells (16 mm × 10 mm) with the longer side oriented perpendicular to the incoming beam direction. To resolve left-right ambiguities in track reconstruction, two successive layers of the same view are staggered by half a cell [40]. Eight aluminum field wires, each with a 90 µm diameter, demarcate the cell area. Two adjacent cells within the same plane and layer share three field wires. At the center of each cell, there is a gold-plated tungsten sense wire with a diameter of 25 µm. It is linked to the BM's high voltage supply and the readout electronics. The field wires (cathode wires), together with the sense wire (anode wire), determine the electric field inside the cell. The working voltage ranges from 1700 to 2000 V applied to the sense wire (the field wires are at 0 V).

The total BM active squared surface is 16 $cm^2$ and the total length is 21 cm. The active length, which is the distance along the beam direction from the sense wire positions on the first layer to those on the last layer of the same view, measures 13 cm. Figure 2.7 displays both a picture and the technical diagram of the BM.

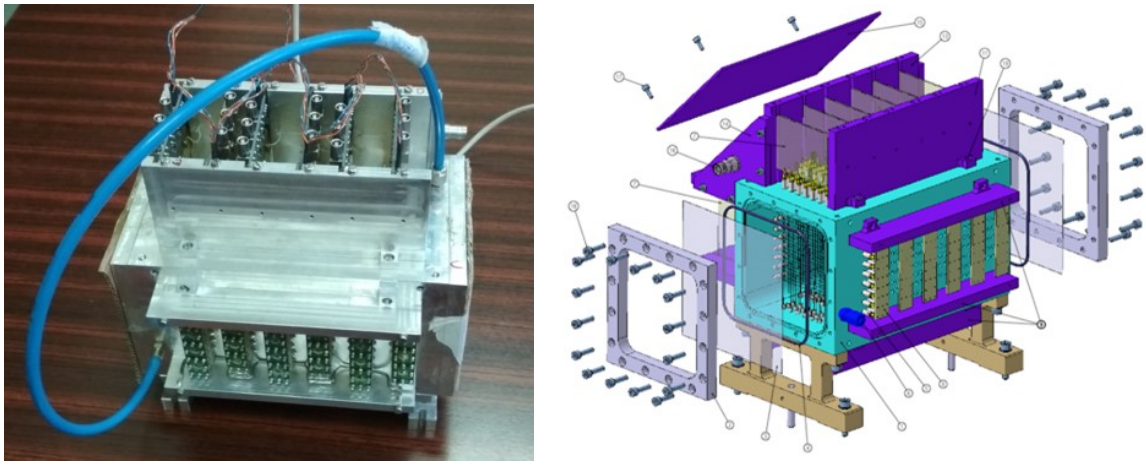

Figure 2.7: A picture (left) and a technical draw (right) of the SC detector.

The BM operates at about 0.9 bar with a gas mixture made of $Ar/CO_2$ at 80/20% and with a gas flow rate of about 1 l/h. The calibration and the performance assessment of the detector has been conducted at the Trento's protontherapy facility with protons at 228 MeV and 80 MeV [41]. Values of about 90% and 100 µm have been found for the hit detection efficiency and the spatial resolution, respectively. High spatial resolution for the BM is crucial because it enables the measurement of the incident beam direction (with an accuracy of a few mrad relative to the primary beam direction) and the determination of the Lorentz boost parameters required for the inverse kinematic approach.

## Vertex detector

The vertex detector (VTX), illustrated in Figure 2.8, is composed of four silicon pixel sensor layers placed along the direction of the incoming beam, guaranteeing a geometrical acceptance of about 40° for the emitted fragments. It is placed few millimeters beyond the target allowing a precise evaluation of the position where the projectile has interacted with the target originating the fragments [42]. The layers are composed of MIMOSA-28 (M28) Monolithic Active Pixel Sensors (MAPS) which consist of a matrix with 928 (rows) × 960 (columns) pixels of 20.7 µm pitch for a total transverse active area of 2.022 × 2.271 $cm^2$. The epitaxial layer has a thickness of 15 µm and is situated on a high-resistivity substrate with a linear resistance of approximately 400 Ω/cm. A single layer has a total thickness of 50 µm, and there is a 2-3 millimeter separation between the layers. The overall maximum rate capability of the detector is of the order of 1-2 kHz to avoid excessive pile up. This also corresponds to the FOOT electronic spectrometer's maximum rate capability, since the VTX is the slowest detector in the acquisition chain.

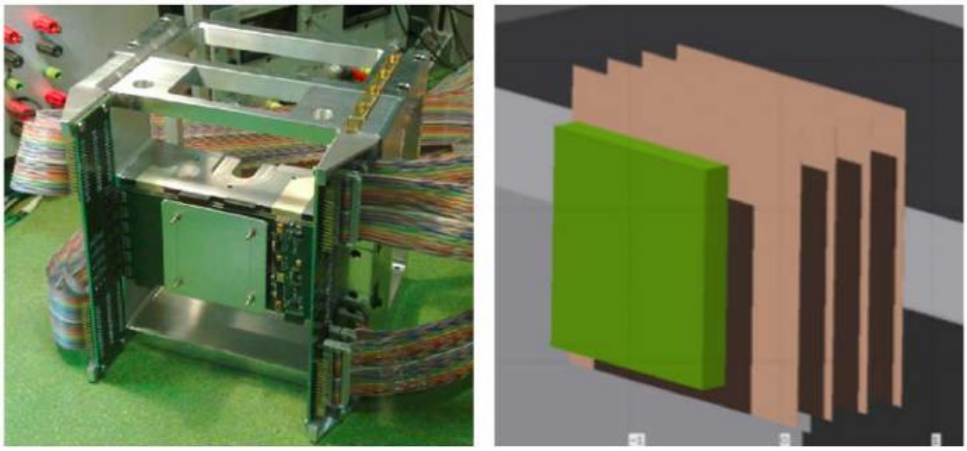

Figure 2.8: Target and Vertex detector setup.

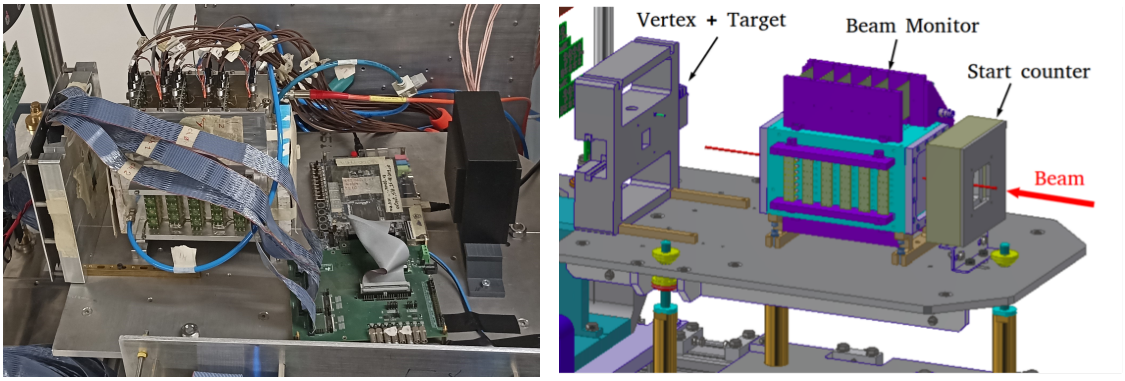


Figure 2.9: (Left) A picture of the up-stream region detectors disposition during the CNAO data taking 2023. (Right) Schematic view of the up-stream region detectors together with the target and vertex container.

## Magnetic system

Beyond the target and the vertex detector, two permanent magnets (PMs) arranged in a Halbach configuration provide the required magnetic field to deflect the fragments in a direction orthogonal with respect to the beam line, facilitating the detection of particle momentum. The choice of magnet type and configuration is driven by the need to balance the portability of the apparatus with the demand for high momentum resolution. Since the magnetic field increases with the external radius and decreases with the gap radius, the two PMs have been designed with different dimensions, in order to provide the required magnetic field maintaining an angular acceptance of 10° for the fragments and to match the momentum resolution of $\sigma(p)/p \sim 5\%$.

Each PM is composed of twelve blocks of magnets arranged in an annular configuration, as shown in Figure 2.10, and they are made of $Nd_2Fe_{14}B_1$. The first PM, close to the vertex detector, has an internal diameter of 5 cm and it provides a maximum magnetic field of 1.4 T. The second PM, close to the downstream region, has a gap diameter of 10.6 cm and a maximum magnetic field of 0.9 T. Between the two PMs there is a gap of 50 mm where the Inner Tracker detector is installed and experiences a magnetic field varying between 0.6 T and 1 T.

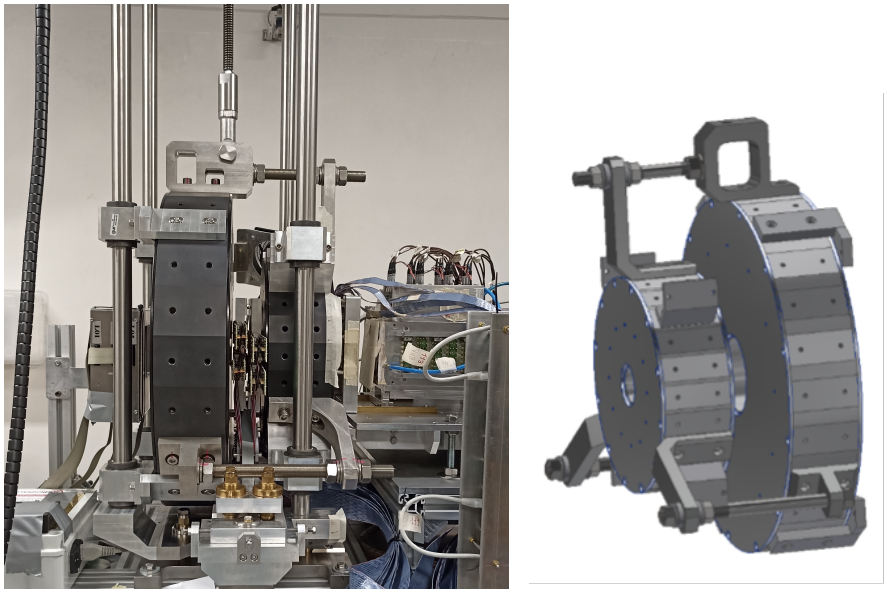

Figure 2.10: (Left) A picture of the magnets' disposition during the CNAO data taking 2023. (Right) Technical draw of the structure containing the two magnets.

Both the PMs provide a magnetic field with an approximately Gaussian shape along the Y axis, perpendicular to the beam direction, as shown on Figure 2.11.

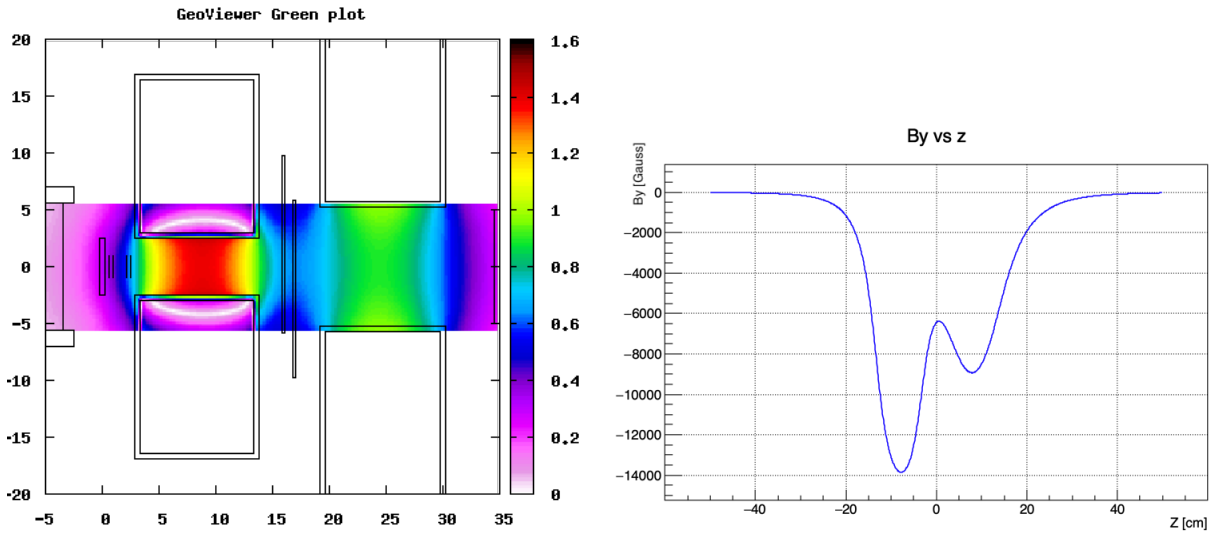


Figure 2.11: (Left) The computed magnetic field map from Sigmaphi [43]. (Right) The profile of the vertical component of the field as a function of z.

In Figure 2.12 it is represented the mechanical structure developed to support the PMs, providing the possibility to lift the magnets allowing the installation and the alignment of the magnetic spectrometer detectors.

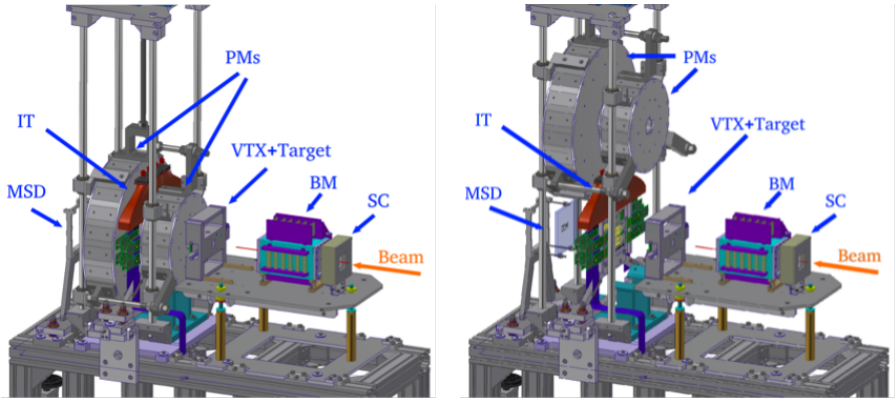


Figure 2.12: The FOOT mechanical structure adopted to contain all the upstream detectors and the magnetic spectrometers during the data taking (left) and during the detectors alignment configuration (right), with the PMs lifted up.

## Inner Tracker

The Inner Tracker (IT) detector, shown in Figure 2.13, is composed of two layers of M28 silicon pixel detectors placed in the gap between the two PMs to track the fragments in the magnetic region. The magnetic field effect on the M28 should be negligible [44]. Each

IT plane, which has a total active area of about 8 × 8 $cm^2$, is composed of two ladders of eight M28 sensors, four on each side, adhered to a 2 mm thick support structure of low-density silicon carbide (SiC) foam. The dead area between two consecutive sensors on the same ladder side is of 30 µm.

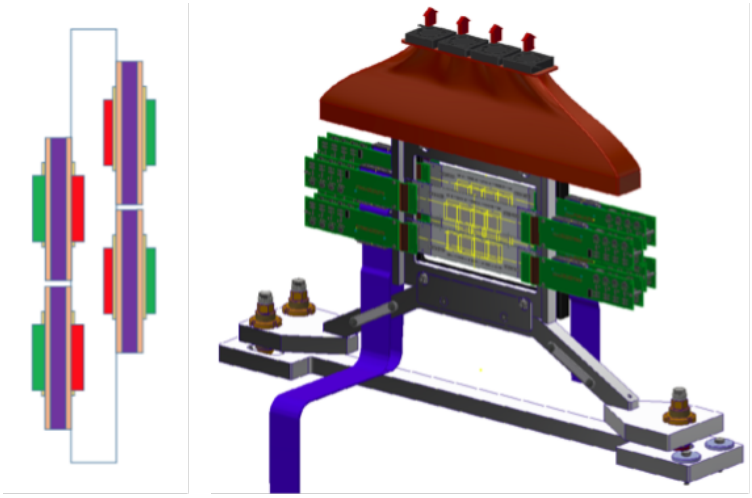

Figure 2.13: Scheme of the IT detector from a perpendicular view (left) and along the beam line (right).

## Microstrip Silicon Detector

The Microstrip Silicon Detector (MSD) is the tracking detector of the FOOT magnetic spectrometer and it is adopted for both determining the fragments' positions and, if needed, quantifying their energy release (ΔE). When focusing on position reconstruction, the detector plays a crucial role in aligning the reconstructed tracks with the signals from the downstream scintillator and calorimeter. The ΔE measurement performed by the MSD complements the one conducted by the Tof-Wall scintillator, which is necessary for identifying the charge of the fragments.

The MSD is composed of three layers of silicon microstrip detectors separated by a gap of about 2 cm and placed beyond the two PMs at 35 cm away from the target. Each layer has an active area of 9.6 × 9.6 $cm^2$ and is composed of two perpendicular Single-Sided Silicon Detector (SSSD) sensors glued on a hybrid Printed Circuit Board (PCB) that provides the mechanical support, as shown in the Figure 2.14. Each sensor has a thickness of 150 µm and a strip pitch of 50 µm. The expected spatial resolution provided by the digital read out is of about 40 µm.

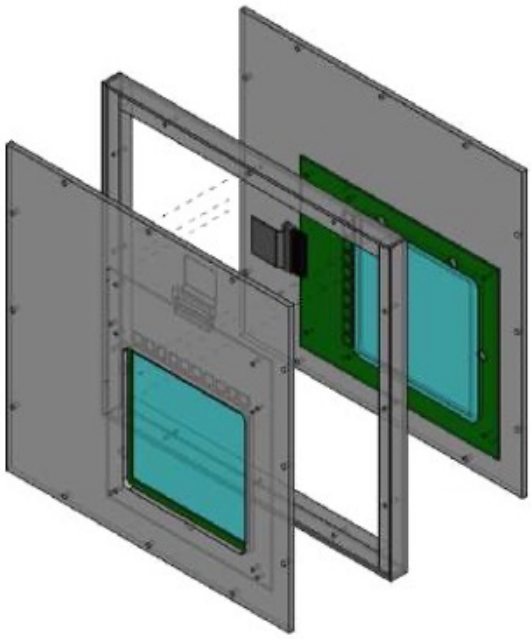

Figure 2.14: View of two layers of the MSD with sensors (blue) and PCB (green).

## Tof-Wall Scintillator

The Tof-Wall detector (TW) is composed of two layers of plastic scintillator bars (EJ-200) oriented in a perpendicular direction, along the x and y plane [45]. It is adopted to measure the fragments' ΔE, position and the last TOF time stamp that allows to obtain the TOF measurement considering as initial time $t_0$ the one taken from the SC. The $\beta$ is obtained from the TOF acquisition based on the track length. The simultaneous measurement of ΔE and $\beta$ allows to identify the charge Z of the impinging ions [46].

Each layer is composed of 20 parallel bars 0.3 cm thick, 2 cm wide and 44 cm long covered with reflective aluminum and darkened with black tape to shield the material from background light sources. The thickness of the bars has been chosen as a compromise between the requirements for the heavier fragments given by the ΔE resolution ($\sigma(\Delta E)/\Delta E \sim 3-10\%$) and TOF resolution ($\geq$ 100 ps) on one hand and the necessity to reduce the secondary fragmentation probability on the other hand. One important limit regarding the TW detection is given by the fact that, if two different particles impinge on the same TW bar at the same time, the system can not distinguishes them. In particular, this problem affects the detection of particles emitted with a low angular separation between them, which are expected to arrive at the same TW bar.

The detector active area is of 40 × 40 $cm^2$ that corresponds to an angular aperture of 10° at 1 m from the target. The read out of each bar is performed by four SiPMs placed

at both the extremities to allow the reconstruction of the hit position along the bar. A picture of a TW bar and of the whole detector is shown in Figure 2.15.

The detector has been tested in different facilities with different primary beams [47]. For proton and carbon ion beams respectively, the obtained energy loss resolution $\sigma(\Delta E)/\Delta E$ is $\sim 6-14\%$ and $\sim 5-7\%$ and the time resolution is 120-180 ps and 30-40 ps. Finally, the precision on the time measurement allows a hit position reconstruction resolution along the bar of $\sigma_{pos} \leq 8$ mm.

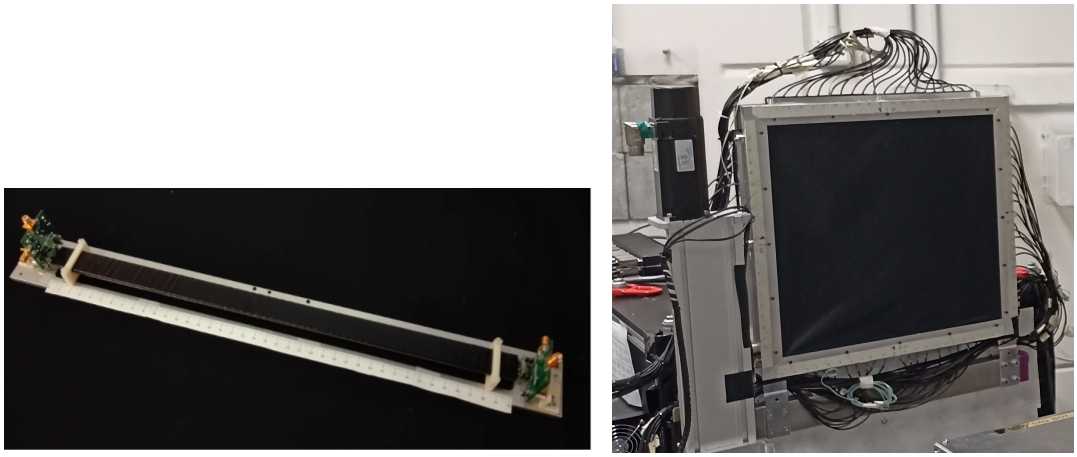

Figure 2.15: Pictures of a crystal of the TW (left) and the whole detector (right) during a test performed at CNAO.

## Calorimeter

The Calorimeter (CA) is the last downstream detector in the FOOT electronic spectrometer, placed just beyond the TW. It is adopted to measure the fragments kinetic energy required to identify their mass number A. It is composed of 320 $Bi_4Ge_3O_{12}$ (BGO) crystals positioned with an approximately spherical arrangement ($\sim$ 20 cm radius), as shown in Figure 2.16, and grouped in Modules, i.e. matrices, of $3 \times 3$ crystals. The crystals have a truncated pyramid shape with a length of 24 cm, a front area of about $2 \times 2$ cm$^2$ and a base area of about $3 \times 3$ cm$^2$ [48]. The readout is based on SiPMs: each BGO crystal is coupled to a 25 SiPMs matrix.

The signal of each crystal is collected by a matrix of 25 SiPMs with an active surface of $2 \times 2$ cm$^2$ and a microcell pitch of 15 µm. This configuration ensures a linear response within the energy range up to 10 GeV. To process the signals from each SiPM matrix, a dedicated board has been custom-designed to match the matrix's dimensions and also monitor the SiPM temperature.

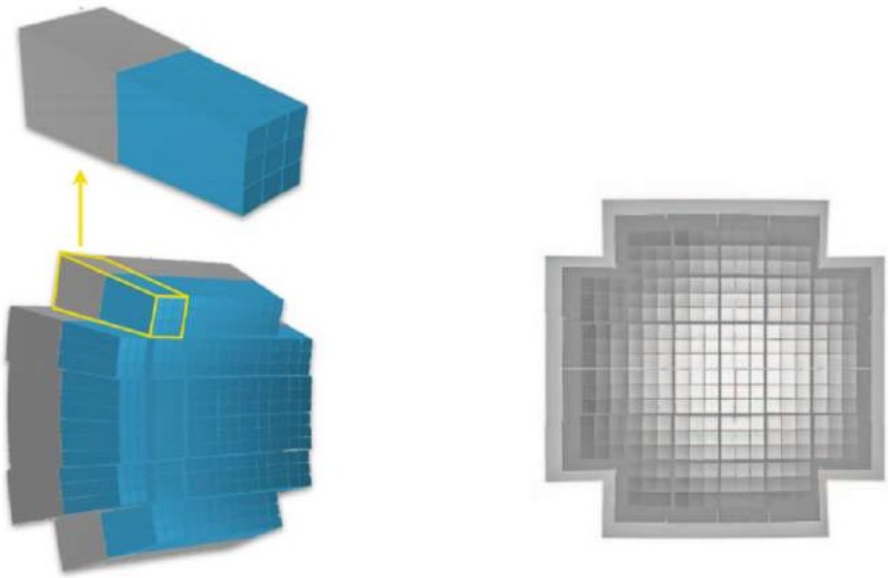

Figure 2.16: CA lateral view with zoom on a single Module (left) and CA front view (right).

After different data takings conducted at CNAO and GSI with proton, helium, carbon and oxygen ion beams in the energy range of 70-400 MeV/u, the CA energy resolution $\sigma(E_{kin})/E_{kin}$ has been evaluated to be below 2% for heavy particles (Z > 2) fulfilling the FOOT experiment requirements for the PT measurements.

Indeed, in the low energy range ($E_{kin} \leq 200$) relevant for PT, the calorimeter reaches its best performances because the primary cause of energy loss in the fragments results from the electromagnetic interactions between the incident particles and the target's electrons and nuclei. In this scenario, full containment of fragments can be achieved to maximize energy resolution. However, this also leads to the production of neutrons, which can escape from the detector and this effect contributes as a systematic error in measuring the energy lost by the particle. In contrast, at energies relevant to space radiation protection measurements (with $E_{kin}$ up to 700-1000 MeV/u), a calorimeter of suitable dimensions cannot completely contain all the fragments produced. At these energies, pion production becomes important and we enter in the regime of hadronic showering, leading to a degradation in detector performance.

### 2.5.2. Emulsion Spectrometer

The emulsion spectrometer (ES) is employed to determine the differential cross sections of low Z fragments (with Z $\leq$ 3) that exhibit a wide angular distribution. The ES, in fact, offers an angular acceptance of about 70° concerning the incident beam axis. The

ES has been designed to function as a standalone experiment and is a highly compact detector based on the same technology as the emulsion cloud chambers used in the OPERA experiment [49].

The whole experimental setup consists of an upstream region, which includes the SC and the BM, followed by the Emulsion Cloud Chamber detector (ECC), which is adopted to track and identify the fragments. The SC is employed to count the total number of delivered particles and to provide the trigger for the data acquisition, while the BM is adopted to measure the incident beam direction and the impinging point position on the ECC. In the Figure 2.17 is shown the experimental setup adopted for the ECC data taking including a plastic scintillator First Start Counter (FSC) developed in the framework of the FIRST experiment and the Beam Monitor adopted also in the FOOT electronic spectrometer.

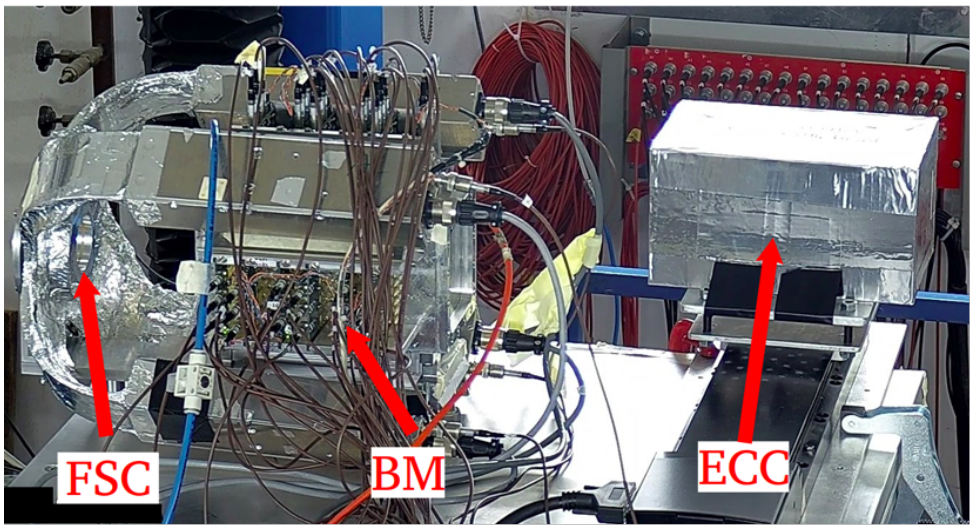


Figure 2.17: A picture of the whole ES setup with FSC, BM and ECC during a data taking performed at GSI.

The ECC is composed of different layers of emulsion films (detector) 70 µm thick adopted to reconstruct the particle position and energy loss, interleaved with passive material exploited as target material and absorber layers. The emulsion films are composed of two sensitive layers of gel with interspersed AgBr crystals of 0.2 µm diameter deposited on the two side of a plastic base 210 µm thick. The layer surface is of 12 × 10 $cm^2$. When a charged particle crosses the emulsion, a sequence of AgBr crystals is sensitized along its trajectory, producing a latent image. Through the chemical development process, each site becomes a crystallization nucleus for metallic Ag transforming the image into a sequence of black-silver grains with a diameter of 0.6 µm, as shown in Figure 2.18. Using an optical

microscope, the three-dimensional position of these grains is determined. By aligning grains across layers of consecutive emulsion films, a particle track, with an associated volume and density, is reconstructed. The positional resolution of the reconstructed track is 0.3 µm and the associated angular resolution is of the order of 1.2 mrad.

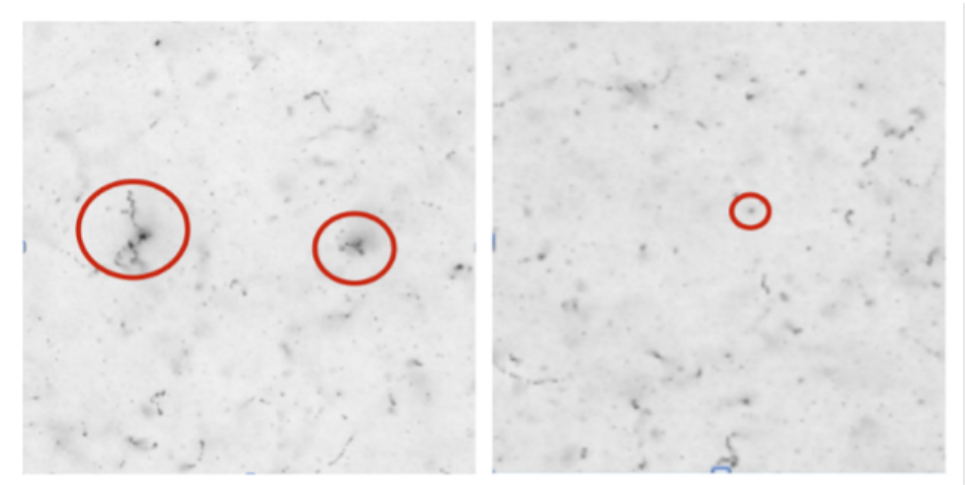

Figure 2.18: A picture of the tracks generated by carbons (center) and protons (right) impinging perpendicularly on the emulsion layer. In the former case, the delta rays are also visible. The view size is 300 × 300 µm [50].

Since the density of a track is directly related to the ionization level of the particle, it enables the identification of the particle's charge within the dynamic range allowed by the detector. For the FOOT emulsions, a minimum ionizing particle leaves a track with a density of the order of 50 grains/100 µm. Furthermore, the refreshing procedure is implemented to overcome the saturation effect experienced with highly ionizing particles. This method extends the dynamic range of the detector by oxidizing the latent image (fading) to eliminate tracks left by particles with lower ionization [50].

The processes taking place in the emulsion film when a beam crosses it makes the ECC a one-shot detector: for each data taking, a different ECC has to be assembled, exposed and lately analysed. The total number of delivered particles needs to be optimized since an excess of incident particles would increase the tracks pile-up, therefore worsening the reconstruction algorithm efficiency. On the other hand, an insufficiency in the number of particles would decrease the statistics not allowing a fully exploitation of the detector.

The ECC can be divided into three main sections (Figure 2.19):

1. **Interaction and Vertexing:** it is composed of emulsion films alternated with layers of target materials(C or $C_2H_4$) of variable thickness (1-2 mm). The emulsion

films are adopted mainly as vertex detector to reconstruct all the secondary charged fragments tracks produced in the target material.

2. **Charge identification:** it is completely composed of emulsion films, aiming to measure the fragments charge with the refreshing procedure [51].

3. **Energy and Mass Measurement:** it contains emulsion films interleaved with absorber layers made of passive high-Z material that can stop the particles in the detector. The aim is to measure the kinetic energy and the momentum of the beam particles by measuring the length of the entire track and the angles between the base-tracks. This allows to identify the particle mass.

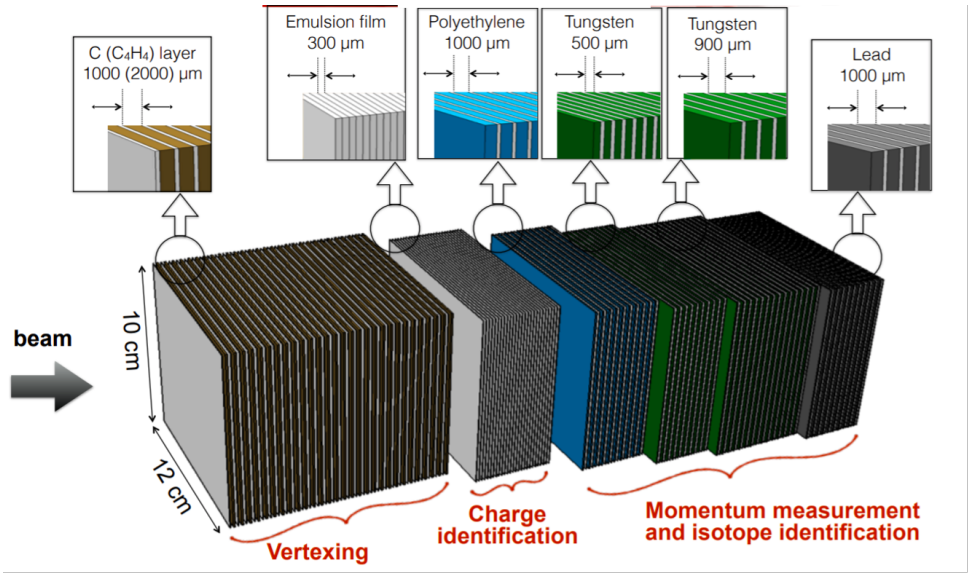


Figure 2.19: Schematic view of the ECC.

## 2.6. Experimental performances required

To meet the objectives of the FOOT experiment while satisfying the radiobiological criteria outlined in Section 2.4.1, different approaches are employed to estimate the charge and mass of the fragments.

For light fragments (with $Z \leq 3$), the ECC refreshing procedure and high-precision tracking effectively meet all performance requirements, as demonstrated in [50].

For heavy fragments (with $Z \geq 3$) various methods are employed in combination with measurements of particle energy loss ($\Delta E$), kinetic energy ($E_{kin}$), velocity ($\beta$), and momentum (p). These methods aid in charge and mass identification, facilitate the inverse kinematic approach, and enable the evaluation of the double differential cross section.

This section will provide details about the measurements performed with the electronic spectrometer detector, the performance criteria assessed through FLUKA Monte Carlo studies, and preliminary results from tests. Subsequently, the techniques used for identifying the charge and mass of the fragments will be presented.

### 2.6.1. Electronic detector required performances

To determine the differential cross sections and conduct charge and mass identification, it is essential to measure the fragments' $\Delta E$, $E_{kin}$, $\beta$, and p with the necessary precision. Different detectors have undergone testing, and through Monte Carlo simulations, the expected and required performances have been assessed, leading to the following outcomes:

- **Energy Loss ΔE:** is fundamental for the charge identification and is measured by the MSD and the TW detectors. Preliminary detector performances from different data takings show a resolution of the order of $\sigma(\Delta E)/E \sim 3-10\%$, as presented in Figure 2.20. In particular, the energy resolution of the TW detector can be modelled as:

$$\sigma(\Delta E) \sim a + \frac{b}{\Delta E} \tag{2.2}$$

where $a = 0.904$ MeV and $b = 18.6$ MeV [47].

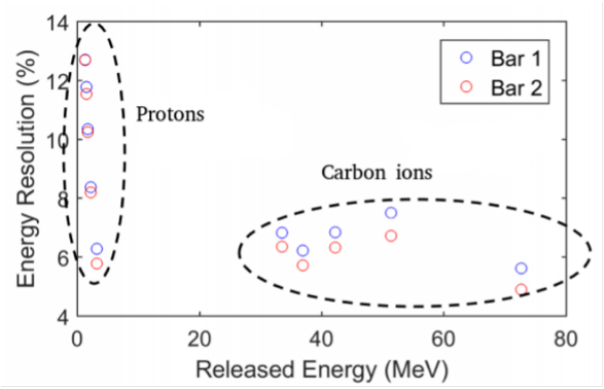


Figure 2.20: Energy resolution $\sigma(\Delta E)/E$ as a function of the energy released ($\Delta E$) in two bars of the TW detector. Data taken at Trento and CNAO with protons at 60-230 MeV and carbon ions at 115-400 MeV/u.

- **Kinetic energy ($E_{kin}$):** is given by the sum of the energy depositions of the particle in the magnetic spectrometer detectors and the calorimeter. In particular, the main contribution to the measurement is given by the CA, whose resolution can

be evaluated as:

$$\sigma(E_{kin})/E_{kin} = \frac{a}{\sqrt{E_{kin}}} \oplus \frac{b}{E_{kin}} \oplus c \tag{2.3}$$

where $a/\sqrt{E_{kin}}$ indicates the stochastic term related to the fluctuations in the sampling of the electromagnetic shower development, $b/E_{kin}$ is the noise term given by the electronic noise of the readout circuit and $c$ is the constant contribution related to the calibration uncertainties. The symbol $\oplus$ indicates the root-sum-square. Preliminary tests, highlighted in Figure 2.21, show a resolution of $\sigma(E_{kin})/E_{kin} \leq 2\%$ for oxygen and carbon ions with energies of 80-400 MeV/u.

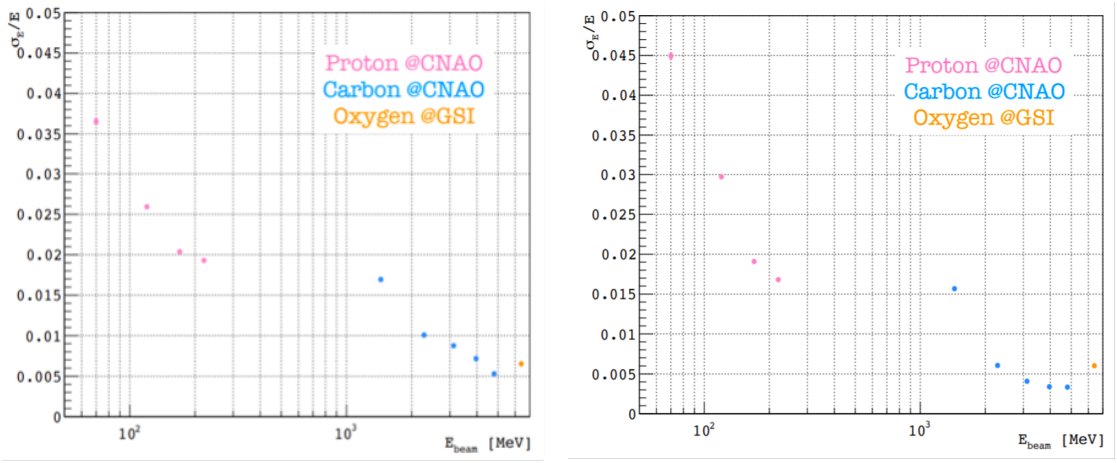


Figure 2.21: Preliminary energy resolution of a single crystal of the FOOT calorimeter evaluated with an amplitude analysis (left) and charge analysis (right) technique. The tests have been performed at CNAO and GSI with different particles at different energies.

- **Velocity ($\beta$):** the particle velocity is evaluated from the particle path length and TOF measurements with the following formula:

$$\beta = \frac{L}{c \cdot TOF} \tag{2.4}$$

where $L$ is the fragment path length from the position where it is produced to the TW detector, which, combined with the SC initial timestamp, provides the TOF measurement. The particle's total travelled distance L is given by the global reconstruction algorithm based on a Kalman filter and it includes the bending due to the magnetic field. The reconstruction algorithm provides an accuracy of $\sigma(L) \sim mm$, while the TOF resolution is calculated as $\sigma(TOF) = \sqrt{\sigma_{SC}^2 + \sigma_{TW}^2}$. Different tests have been conducted with the SC and TW detectors in CNAO and GSI facilities

with 115-400 MeV/u carbon and 400 MeV/u oxygen ions. The results are shown in Figure 2.22: for carbon and oxygen ions in the PT energy range, the overall TOF resolution is of the order of 70 ps. For protons, as shown in Figure 2.21, the TW time resolution is between 100 and 180 ps and the consequent TOF resolution is expected to be $\sim$ 140-250 ps, due to their lower ionizing effect. However, since the electronic spectrometer is designed for the detection of heavy fragments (Z $\geq$ 3), the overall results fulfill the experimental requirements of a $\sigma(TOF) \leq 100ps$. The resolution on the particle velocity is mainly given by the TOF contribution $\sigma(\beta) \sim \frac{L}{c \cdot TOF^2} \cdot \sigma(TOF)$ and it is of the order of $\sim 0.006$.

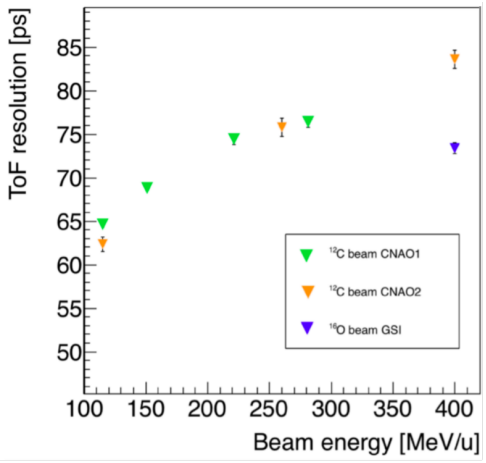


Figure 2.22: TOF resolution evaluated as a function of the incident particle type and energy. Data taken at CNAO and GSI with the SC and TW detectors.

- **Momentum (p):** is evaluated by means of the FOOT magnetic spectrometer. Each detector provides different hits that are elaborated by a global reconstruction algorithm based on a Kalman filter. The preliminary results show that the required momentum resolution is of $\sigma(p)/p \sim 5\%$.

### 2.6.2. Charge and mass identification

In order to optimize the FOOT electronic spectrometer performances, a detailed MC simulation has been developed including all the detectors' parameters and materials. By means of simulations, different methods have been developed for the particle charge and mass identification.

## Charge identification

In the case of emulsion spectrometer, the assessment of fragment charge is achieved through the refreshing procedure, exploiting the particle's energy loss dependence on the atomic number. The same physical phenomenon is also employed in the electronic spectrometer for charge identification through two distinct methods.

The first one involves the MSD and the TW detectors and takes into consideration the simplification of the Bethe-Bloch energy loss formula:

$$\frac{dE}{dx} \sim z^2 \cdot f(\beta) \tag{2.5}$$

where $dE/dx$ is the energy loss, $z$ is the particle charge and $f(\beta)$ is a function of the particle velocity $\beta$, which is expected to be similar to that of the primary particle. In particular, both the detectors measure the particle energy release $\Delta E$, while the path length $\Delta x$ is considered roughly equal to the detector thickness. The ratio $\Delta E/\Delta x$ is an estimate of the energy loss that, combined with the $\beta$ measurement, provides a charge identification.

The second method employs the VTX, MSD and the IT detectors. In details, when a charged particle crosses a layer of silicon pixel detector, it fires different adjacent pixels that can be grouped in a cluster. The cluster size is determined by the number of activated pixels and varies based on the energy loss of the particle, hence reflecting the charge of the incoming particle. An empirical model has been developed to describe this dependence [42]:

$$n_p = 2\pi r_s log(\frac{\Delta E}{2\pi E_g T_s}) \tag{2.6}$$

where $n_p$ is the mean number of pixels, $\Delta E$ is the energy release, $E_g$ is the mean energy for the creation of a pair of charge carriers (e.g. $E_g = 3.6$ eV for silicon material), $T_s$ and $r_s$ are two free parameters. Combining Equation (2.5) and Equation (2.6), the particle charge can be extrapolated from the TOF measurement and the cluster size. Since the cluster size is related to the energy loss logarithmically, with this method the charge identification capability is decreased for the high energy loss and high charged particles.

The most accurate charge identification results are achieved through the TW detector. With a $\Delta E$ resolution of the order of $3 - 10\%$, the level of mis-identification of fragment charges, as determined through MC simulations, remains below 4%. Nevertheless, the

VTX cluster size method can serve as a supplementary mean to validate the TW outcomes, and it can also be integrated into the VTX track reconstruction algorithm.

## Mass identification

The particle isotopic measurement is a more challenging goal compared to the charge identification. For this reason, the particle mass is evaluated combining the TOF, momentum and kinetic energy measurements in three different ways:

1. **TOF and momentum:**

$$p = m\gamma\beta = \frac{m\beta}{\sqrt{1-\beta^2}} \Rightarrow m = \frac{p\sqrt{1-\beta^2}}{\beta}$$

$$A_1 = \frac{m}{u} = \frac{1}{u}\frac{p\sqrt{1-\beta^2}}{\beta}$$

   where $u = 931.494\ \mathrm{MeV}/c^2$ is the atomic mass unit, $p$ is the particle momentum, $\gamma$ is the Lorentz factor and $\beta$ is the particle velocity.

2. **TOF and kinetic energy:**

$$p^2 = E_{kin}^2 - m^2 \Rightarrow m^2\gamma^2\beta^2 = (E_{kin}+m)^2 - m^2$$

$$A_2 = \frac{m}{u} = \frac{E_{kin}}{u}\frac{1+\sqrt{1+\gamma^2\beta^2}}{\gamma^2\beta^2}$$

   where $Ekin$ is the kinetic energy.

3. **Momentum and kinetic energy:**

$$E_{tot}^2 = p^2 + m^2 \Rightarrow (E_{kin}+m)^2 = p^2 + m^2$$

$$A_3 = \frac{m}{u} = \frac{E_{kin}^2 - p^2}{2E_{kin}}$$

   where $Ekin$ is the kinetic energy.

Since the calorimeter suffers from the neutron production, the best mass identification evaluation is obtained with the combination of TOF and momentum measurements. However, all the three methods are adopted to reduce the systematic uncertainty and to achieve the best possible results. The redundancy of the mass determination techniques is an important key factor in the FOOT experiment to reach its goal. The three measurements will be combined with an *Augmented Lagrangian Method* and a *standard* $\chi^2$ *minimization*

*algorithm*:

- **Standard $\chi^2$ minimization algorithm:** is based on the minimization of the following function:

$$\chi^2 = f(\vec{x}) + \mathbf{A}^T(\mathbf{C}\mathbf{C}^T)^{-1}\mathbf{A} \tag{2.7}$$

where

$$f(\vec{x}) = \frac{(TOF - \overline{TOF})^2}{\sigma^2(TOF)} + \frac{(p - \bar{p})^2}{\sigma^2(p)} + \frac{(E_{kin} - \overline{E_{kin}})^2}{\sigma^2(E_{kin})} \tag{2.8}$$

$TOF$ , $p$ and $E_{kin}$ are the reconstructed values, $\sigma(TOF)$, $\sigma(p)$ and $\sigma(E_{kin})$ are the respective uncertainty and $\overline{TOF}$, $\bar{p}$ and $\overline{E_{kin}}$ are the fit output parameters. $\mathbf{A} = (A_1 - \bar{A}, A_2 - \bar{A}, A_3 - \bar{A})$ is the mass estimate vector, where $A_1$, $A_2$ and $A_3$ are the estimated mass values and $\bar{A}$ is the fitted output mass. Matrix $\mathbf{C}$ is the correlation matrix:

$$\mathbf{C} = \begin{bmatrix} \frac{\partial A_1}{\partial TOF} \cdot \sigma(TOF) & \frac{\partial A_1}{\partial p} \cdot \sigma(p) & 0 \\ \frac{\partial A_2}{\partial TOF} \cdot \sigma(TOF) & 0 & \frac{\partial A_2}{\partial E_{kin}} \cdot \sigma(E_{kin}) \\ 0 & \frac{\partial A_3}{\partial p} \cdot \sigma(p) & \frac{\partial A_3}{\partial E_{kin}} \cdot \sigma(E_{kin}) \end{bmatrix} \tag{2.9}$$

- **Augmented Lagrangian Method (ALM):** is based on an iterative procedure of minimization of the Lagrangian function $\mathcal{L}$:

$$\mathcal{L}(\vec{x}, \boldsymbol{\lambda}, \mu) = f(\vec{x}) = \sum_{i=1}^{3} \lambda_i c_i(\vec{x}) + \frac{1}{2\mu} \sum_{i=1}^{3} \lambda_i c_i^2(\vec{x}) \tag{2.10}$$

where $f(\vec{x})$ is the function to minimize shown in Equation (2.8), $c_i(\vec{x}) = (A_i - \bar{A})$ are the constraints, $A_i$ are the mass values estimated with the previous methods, $\bar{A}$ is the fitted mass output parameter, $\lambda_i$ are the Lagrange multipliers and $\mu$ is a positive penalty parameter that, multiplied with $c_i^2(\vec{x})$, constitutes the augmentation factor.

Similar results are obtained with both methods. As shown in Figure 2.23, considering the expected values of $TOF \sim 70ps, \sigma(p)/p \sim 3.7\%$ and $\sigma(E_{kin})/E_{kin} \sim 1.5\%$, the $^{11}$C, $^{12}$C and $^{13}$C peaks are visible and mass identification can be performed. The error on the mass calculation is very sensitive to the uncertainty of the TOF.

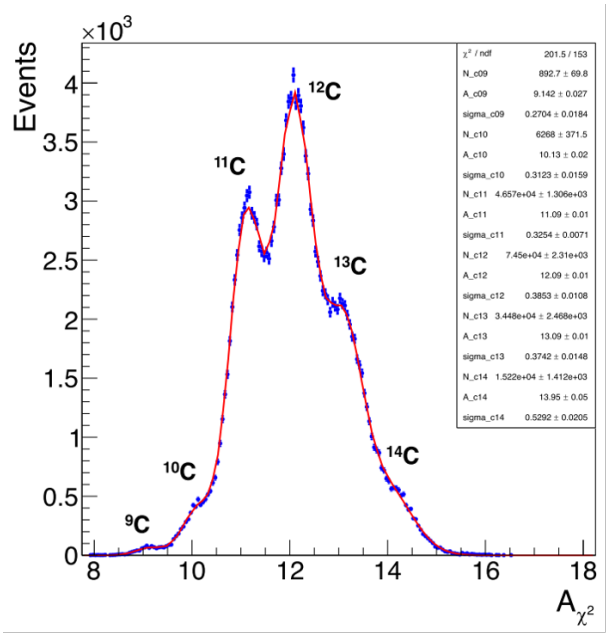


Figure 2.23: Example of mass identification performed with the $\chi^2$ method on MC simulated data. The resolution of the measurements has been set to their expected values: $TOF \sim 70ps, \sigma(p)/p \sim 3.7\%$ and $\sigma(E_{kin})/E_{kin} \sim 1.5\%$.

# 3 | MC simulation and reconstruction software

## 3.1. Introduction

The FLUKA simulation software plays a crucial role in fine-tuning the detector parameters for the FOOT electronic spectrometer and it conducts preliminary investigations through simulated MC data. The analysis of both MC and experimental data is managed by a specialized reconstruction software specifically developed for the FOOT experiment. This software is employed to process the various measurements from the different detectors, such as time stamps, detector hits and associated $\Delta E$. This allows to reconstruct the tracks of charged particles, reconstructing their direction, momentum and identify charge and mass.

In Section 3.2, it is provided a concise introduction to the FLUKA simulation tool employed for generating MC data. Following that, an explanation of the FOOT reconstruction software has been detailed in Section 3.3.

## 3.2. MC Simulation

MC simulations provide a potent tool for accurately modeling and simulating nuclear interactions, covering a wide energy spectrum. This versatility enables MC simulations to adapt to diverse experimental scenarios, spanning from low-energy nuclear reactions to ultra-relativistic collisions. In the context of nuclear and high-energy physics facilities, MC simulations are used to predict the outcomes of collisions, particle decays, and detector responses. This capability empowers researchers to fine-tune experimental setups and enhance data analysis techniques, ultimately optimizing the quality of their results.

In the framework of medical physics, MC simulations are an essential instrument for the design and establishment of innovative clinical facilities, allowing a detailed description of the beam line and the delivery system. Furthermore, MC codes offer a distinctive capability in the commissioning, validation, and potential enhancement of Treatment Planning Systems (TPSs). In situations where experimental validation is unavailable and/or analytical methods are inadequate, MC simulation allows patient-specific dose calculation.

### 3.2.1. The FLUKA Monte Carlo code

The MC simulation tool utilized in the FOOT experiment is the FLUKA (FLUktuierende KAskade) code [52–54]. Developed by the European Organization for Nuclear Research (CERN) and the INFN, FLUKA is a robust and versatile software package designed for simulating and analyzing particle interactions with matter. It is employed in different physics branches for the calculations of particle transport and interactions with matter, spanning from proton and electron accelerator shielding to target design, calorimetry, activation, dosimetry, detector design, Accelerator Driven Systems, space radiation and cosmic ray showers, neutrino physics, and radiotherapy. It excels in the field of PT, thanks to the development of specific simulation features tailored to clinical research. The diverse requirements of these applications demand consistent reliability for all types of projectiles, spanning from elementary particles to heavy ions across a wide energy spectrum. In particular, the energy range covered for hadron–hadron and hadron–nucleus interaction is from threshold up to 10000 TeV, while electromagnetic and $\mu$ interactions can be dealt with from 1 keV up to 10000 TeV. Nucleus–nucleus interactions are also supported up to 10000 TeV/u. Transport in arbitrarily complex geometries, including magnetic field, can be accomplished using the FLUKA combinatorial geometry. A graphical user interface (GUI), FLAIR, makes it easier to set up simulations, define geometry, input parameters, run simulations, and analyze the results. An example of a 2-D top view of the FOOT

simulation setup is shown in Figure 3.1, in a geometrical configuration in which the distance between TG and TW is 1.75 m.

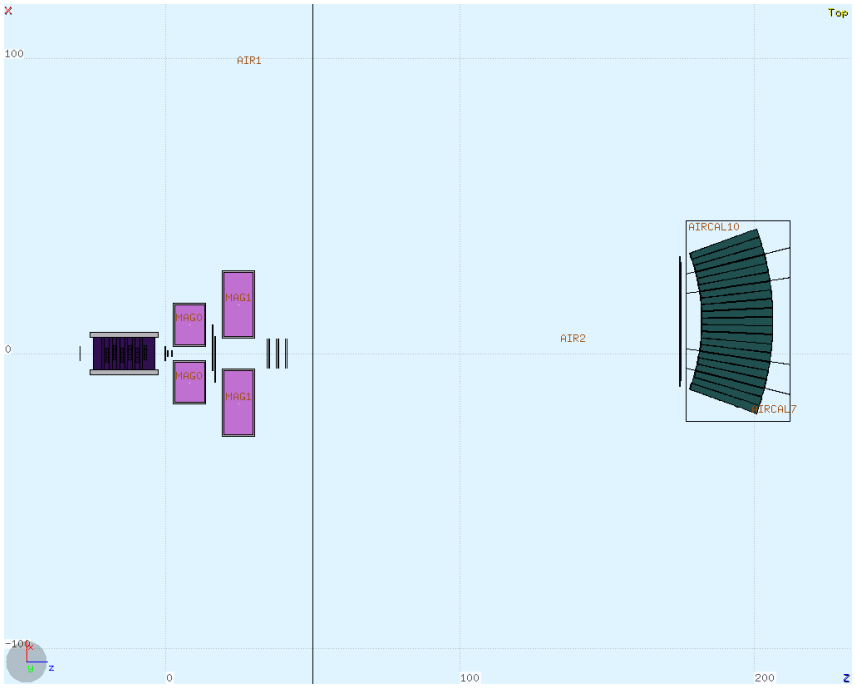


Figure 3.1: FLAIR visualization of the 2-D top view of the experimental setup implemented in the FLUKA simulation.

The code is continuously updated with the latest modern physics models, adopting the microscopic models whenever possible and checking the latest experimental data as benchmark for the simulation output [55].

The main models adopted in FLUKA for the description of the principal physics phenomena are shown below, followed by the presentation of the simulation output scheme specifically developed in the framework of the FOOT experiment.

### 3.2.2. FLUKA physics phenomena models

1. **Hadron-nucleon interactions**

   The FLUKA hadron-nucleon interactions are described in terms of resonance production and decay for energies below 5 GeV and by a model [56] based on the *Dual Parton Model* (DPM) [57] for energies from 5 GeV up to tens of TeV. The DPM is a phenomenological model of particle production in hadronic and nuclear collisions. It is based on the large-N expansion of non-perturbative *Quantum ChromoDynamics* QCD [58] and the *Reggeon field theory* [59], allowing to describe also the soft

collision processes for which the QCD perturbation theory cannot be applied.

2. **Charged particle transport**

   Transport of charged particles is performed through an original Multiple Coulomb scattering algorithm based on the *Moliere theory* [60], supplemented by an optional single scattering method. It gives the correct lateral displacement and it handles some demanding challenges such as the electron backscattering effect and the energy deposition in thin layers, even in the few keV energy range.

   The treatment of ionization energy loss is based on a statistical approach alternative to the standard Landau and Vavilov ones according to the Bethe-Bloch theory. $\Delta$-ray production and transport can be activated taking also into account spin effects and ionisation fluctuations, providing a very good reproduction of average ionization [61].

3. **Hadron-nucleus (h-A) interactions**

   The initial state of the hadron-nucleus interaction is simulated in FLUKA with two models depending on the projectile energy:

   - **PreEquilibrium Approach to NUclear Thermalization (PEANUT):** adopted for particles with momenta below 3-5 GeV/c, the approach is based on a detailed *Generalized Intra-Nuclear Cascade* (GINC) model for the initial hadron-nucleus non-elastic interaction stage. In the GINC model, (h–A) reactions are described as a cascade of two-body interactions concerning the projectile and the reaction products. After the emission or absorption of heavy particles, the subsequent pre-equilibrium stage model is adopted to describe the de-excitation of the hot nuclear components, by emission of nucleons and light nuclei (A$<$5) until thermal equilibrium is reached.
   - **Glauber-Gribov cascade:** is a field theory formulation of the *Glauber model* [62] adopted in FLUKA for particles with momentum higher than 5 GeV/c. The inelastic interactions are modelled as multiple interactions of the projectile with the target nucleons, and the interaction rate obtained is from free handron-nucleon cross sections. As for the PEANUT model, also in this case a subsequent de-excitation phase is described by nuclear evaporation, fission, Fermi break-up and $\gamma$ de-excitation process, depending on the energy and the target-nucleus mass.

   For the FOOT experiment, the PEANUT model is the most relevant since the energy of the particles involved in the measurements is below 5 GeV/c. Its flowsheet

is illustrated in Figure 3.2.

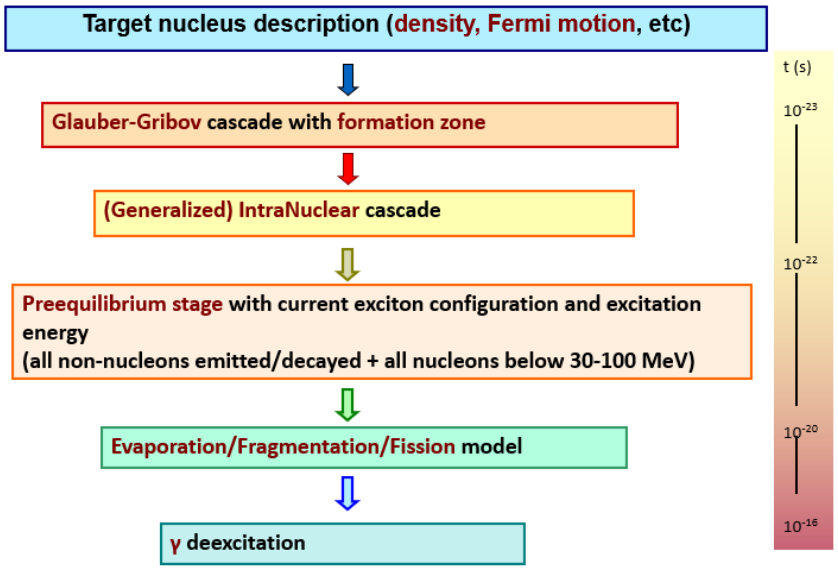


Figure 3.2: FLAIR visualization of the 2-D top view of the experimental setup implemented in the FLUKA simulation.

4. **Nucleus-nucleus interactions:**

   Depending on the energy, three different models are adopted in FLUKA to describe the nucleus-nucleus interactions:

   - the *Boltzmann-Master Equation model* (BME) [63, 64] is adopted for light ion interaction for energies ranging from the Coulomb barrier up to about 125 MeV/u in average. The main process taken into account in the model is the complete fusion of the projectile with the target nucleus, or the incomplete fusion between the quasi-projectile and the quasi-target fragments produced by a break-up process. In particular, the BME model describes the thermalization of composite nuclei by means of two-body interactions and secondary particles emissions. Three body interactions and inelastic excitation are also investigated by the model.

   - the *Relativistic Quantum Molecular Dynamics model* (rQMD) [65] is applied for energies between 0.1 and 5 GeV/u. In this model each nucleon of the projectile and of the target material is represented by a Gaussian wave function. The dynamics is simulated according to the Fermi kinetic energy inside the potential wall generated by the other surrounding nucleons. The collision process is simulated minimizing the nucleon-nucleon Hamiltonian equation of motions,

considering all the nucleons presented in the projectile and target overlapping region. Due to the increase of complexity, MC simulations performed with this model are much more slow than using the normal Intra-Nuclear Cascade (INC) model.

The transition energy range between the two models (100-150 MeV/u) is of great interest for PT and different efforts have been spent in the last years to smooth the transition, developing an extended version of the rQMD code [66].

- at higher energies ($\geq$ 5 GeV/u), *Dual Parton Model* and *JETs* (DPMJET-II or DPMJET-III) [67] model are adopted to simulate the nucleus-nucleus interactions. In details, this model is based on the DPM in connection with the Glauber formalism and it is generally used for the cosmic ray studies.

5. **Leptons-Photons interactions**

The transport of electrons and photons in FLUKA (EMF, for ElectroMagneticFluka) handles all interactions and scattering processes, including photon nuclear interactions [68]. The electromagnetic sector is fully coupled to the hadronic one, for instance photons from nuclear deexcitation are directly transported by EMF, and photonuclear interactions are treated in the same PEANUT framework as hadronic interactions.

The leptons-photons interactions are simulated in a wide energy range of about 12 energy decades, ranging from 1 keV up to 1 PeV. In particular the Bremsstrahlung effect is based on the differential cross section data published by Seltzer and Berger [69, 70] interpolated to obtain a finer energy mesh and extended to 1 PeV. It includes also the Landau-Pomeranchuk-Migdal suppression effect [71] and the Ter-Mikaelyan polarization effect. All the other leptons-photons interactions simulated in FLUKA are listed in Figure 3.3.

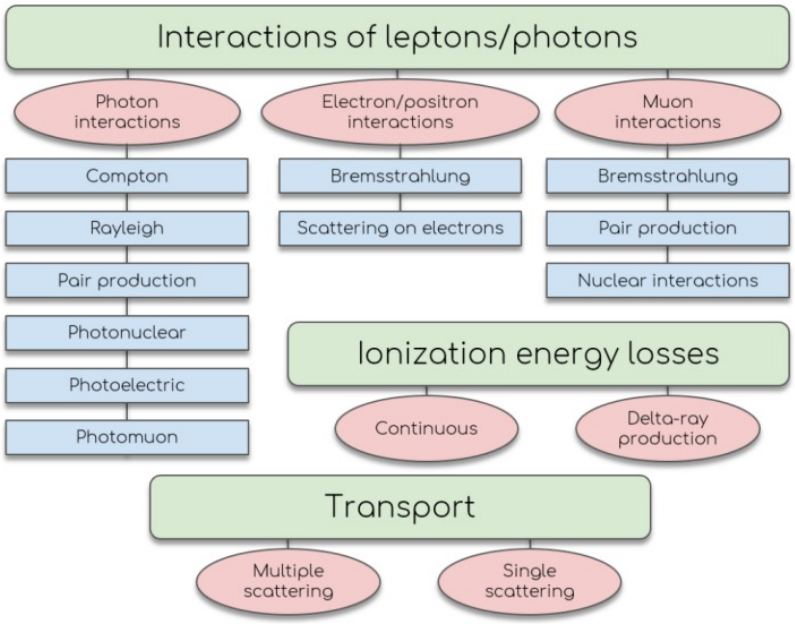


Figure 3.3: Scheme of the electromagnetic interactions models developed in FLUKA.

### 3.2.3. Clustering in FLUKA

The phenomena of nuclear clustering is modelled in FLUKA at the end of pre-equilibrium stage. For all nuclei (both primary and residual) with A<18 a Fermi Break-up model [72] is used. It provides for $\sim$ five thousands combinations and a maximum of six final products. It is triggered in FLUKA regardless of the model that handled the direct interaction, be it BME or rQMD.

The clustering mechanism implemented in FLUKA's Fermi break-up considers the creation of intermediate states (e.g., $^{8}$Be) with a number of energy levels known from nuclear databases. The probability of passing through intermediate states depends on the excitation energy available in the reaction. For example, fragmentation of $^{12}$C into three $\alpha$ particles can also occur directly for very high excitation energies. Thus there is an energy dependence, but not directly related to the energy of the projectile: the excitation energy depends, for example, on the impact parameter and on the number of nucleons involved. Peripheral interactions (characterized by an high value of the impact parameter) are the most frequent, resulting in low values of the excitation energy. In this case, the two-step process is favoured, for example: $^{12}\mathrm{C} \rightarrow {}^{8}\mathrm{Be} + \alpha \rightarrow 3\ \alpha$.

Instead, for A>17, a statistical evaporation model is activated, whose does not explicitly predict $\alpha$ correlations due to clustering. This implies that the simulation with FLUKA of interactions with $\alpha$-conjugated heavy nuclei probably does not correctly match what

happens in reality from the clustering point of view.

### 3.2.4. FLUKA output

Since the FLUKA standard output does not include an event per event data structur, the FOOT team has created a specialized simulation output of the FLUKA code for the electronic spectrometer. This makes possible the reconstruction of each event, with all the detectors information particle by particle and event per event. It is generated by extensively modifying the standard FLUKA output through user routine libraries.

In particular, the custom output is an ASCII file that contains all the simulated data and, by means of a program specifically developed, it is converted into a root file organized in blocks as following:

- **Particles block:** in this part are stored the information related to all the particles produced during the simulation. It is possible to retrieve the particle mass, charge, barionic number, position and momentum at the production and at the death and also the pointer to the parent particle.
- **Detector block:** a dedicated block is reserved to store each FOOT detector output, collecting all the hits information relevant for a given device. A hit is essentially the signal produced when a particle is successfully detected, corresponding to an energy release based on the type of detector. For each hit, the energy release, the position and momentum values and all the other quantity of interest for the specific detector is saved. As an example, when a particle enters and releases energy in a BM cell, a hit is registered in the BM block with the information about the cell coordinates, the particle entrance and exit position and momentum, the energy deposition and an index that points to the particle block.
- **Crossing block:** when a particle crosses a passive or active material defined in the FLUKA geometry, i.e. a region, the information about the crossing position and the particle momentum is stored, together with a pointer to the particle block.

In order to perform MC studies, the FOOT data analysis software is developed to produce the input files adopted by FLUKA to generate the simulated dataset, considering all the geometry parameters of the FOOT detectors. After the event by event simulation, the FLUKA output contains all the detectors simulated hits and measurements and it is returned as input to the analysis software to perform the MC study. In this way, all the geometry parameters and the projectile properties among the simulation and the analysis software are consistent.

## 3.3. SHOE Reconstruction software

The software of FOOT plays a key role in the experiment by performing the reconstruction of the whole event form the raw data of the Monte Carlo simulations. In the first phase it has been used for the study of the best experimental setup by examining the simulation of different detector configurations and, in a second phase, it will perform the reconstruction on the real data, followed by the final cross section measurement. The FOOT software has been named SHOE (*Software for Hadrontherapy Optimization Experiment*) and it is used to read both simulated and real data of all the detectors performing firstly a local and then a global reconstruction procedure. In the local reconstruction, the simulated hits or the raw measurements are elaborated to reconstruct the physics quantities relevant for each detector. Then, a global reconstruction algorithm processes all the information from the detectors to reconstruct the whole event and extract the fragment tracks and properties, performing also the particle charge and mass identification. The main tasks of the local reconstruction on different detectors are:

- **SC and TW:** on the real data, the waveforms is processed by the detectors with a virtual constant fraction discriminator algorithm to retrieve the time measurements. In addition, the TW measures also the energy release of each hit applying a signal amplitude analysis. In case of MC studies, FLUKA provides directly a simulated time stamp and the energy release of each particle in each detector.
- **BM:** on the real data, it combines the time measurements with a given space-time relation to extract the distance measurements. With the MC simulations, the distances are directly extracted from the input file. Then, the software performs a track reconstruction procedure to extract the projectile track parameters from the BM hits.
- **VTX, IT and MSD:** each detector performs a local track reconstruction with both real data and MC file starting from the detection of clusters. Clusters are groups of adjacent pixels that light up when a particle impacts the detector, transferring energy to it. The VTX also attempts to define the "vertices" of primary interactions on the target by matching with the track defined by the BM. In addition, the energy releases are directly measured by the MSD detector and evaluated by means of the cluster sizes by the pixel detectors.
- **CALORIMETER:** in case of real data, the signals are read and processed from each crystal and amplitude, charge and shape analysis are performed to retrieve the energy deposition measurements. Otherwise, FLUKA provides directly the infor-

mation. In both cases, a clustering algorithm is performed to take into account the particles that cross more than one crystal.

In order to take into account the resolution, efficiency, pile-up and the other specific effects of each detector that cannot be simulated directly by FLUKA, SHOE reproduces the detector resolutions, eliminates the simulated hits according to the efficiencies and adds the pile-up and the noise hits in order to make the simulation similar to a real scenario as much as possible. After the local reconstruction, in the global reconstruction stage all the information from the detectors are combined to complete the analysis. At this level, there are no differences in the elaboration of MC or real data. In details, the following main tasks are completed:

- **Global track reconstruction:**

  it is performed by means of the GENFIT [73] software, which is a toolkit that performs track fitting. In GENFIT, the track fitting is based on three pillars: measurements, track representations and fitting algorithms. The latter comprises two *Kalman filters* (one which linearizes the transport around the state predictions and one which linearizes around a reference track) and a *deterministic annealing filter* (DAF).

  The extended Kalman filter is an iterative algorithm that produces an optimal estimate of a system state (with covariance) from a series of noisy measurements (extended dissertation in Section 3.3); nevertheless this particular algorithm can bring some problems due to the linearization around predictions. Especially for the first few hits, state predictions may stray very far from the actual trajectory; moreover outlier points can significantly bend the prediction away from the actual trajectory. The worst consequence can be the failure of the fit. A possible solution is to take estimated track parameters from pattern recognition or previous fit as expansion point for linear approximation, which means linearize around reference track instead of state predictions. This procedure is carried out by the Kalman filter with reference track shown in Figure 3.4.

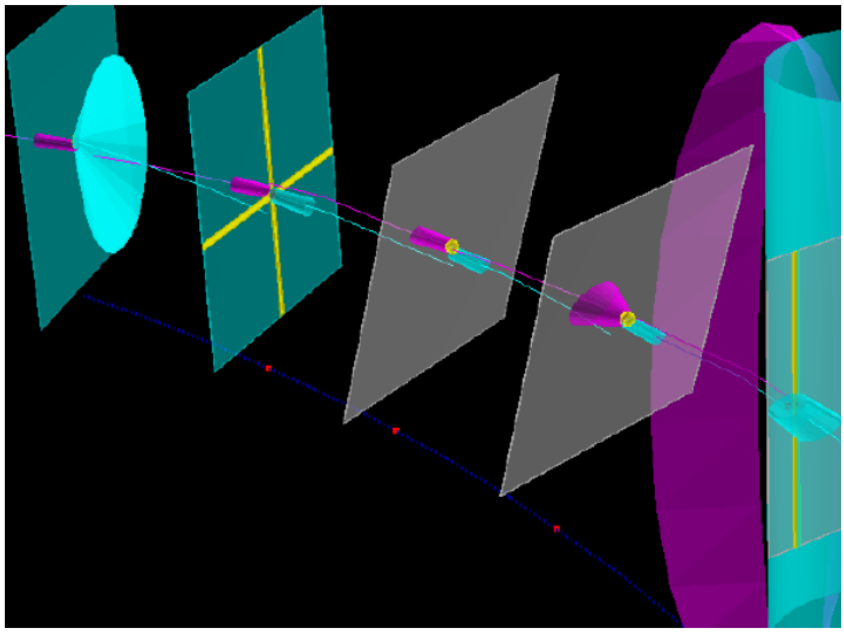

Figure 3.4: First iteration of Kalman filter tracking algorithm with reference track.

However, in case of outliers, the track fitting can be strongly biased. A robust algorithm that can be used in this case is the DAF (Deterministic Annealing Filter) [74] which is able to reject outliers or to resolve left/right ambiguities of wire-measurement. The DAF is an iterative Kalman filter that assigns probabilities to each measurements (weights). By weighting and annealing, the DAF can reject outlying measurement and, doing so, it can find the best fit. An example is shown in Figure 3.5. At present, the specific implementation in FOOT experiment uses the standard Kalman filter algorithm; different studies are ongoing on the possible use of the DAF, which should be more powerful and appropriate in the presence of multiple background hits. Figure 3.5.

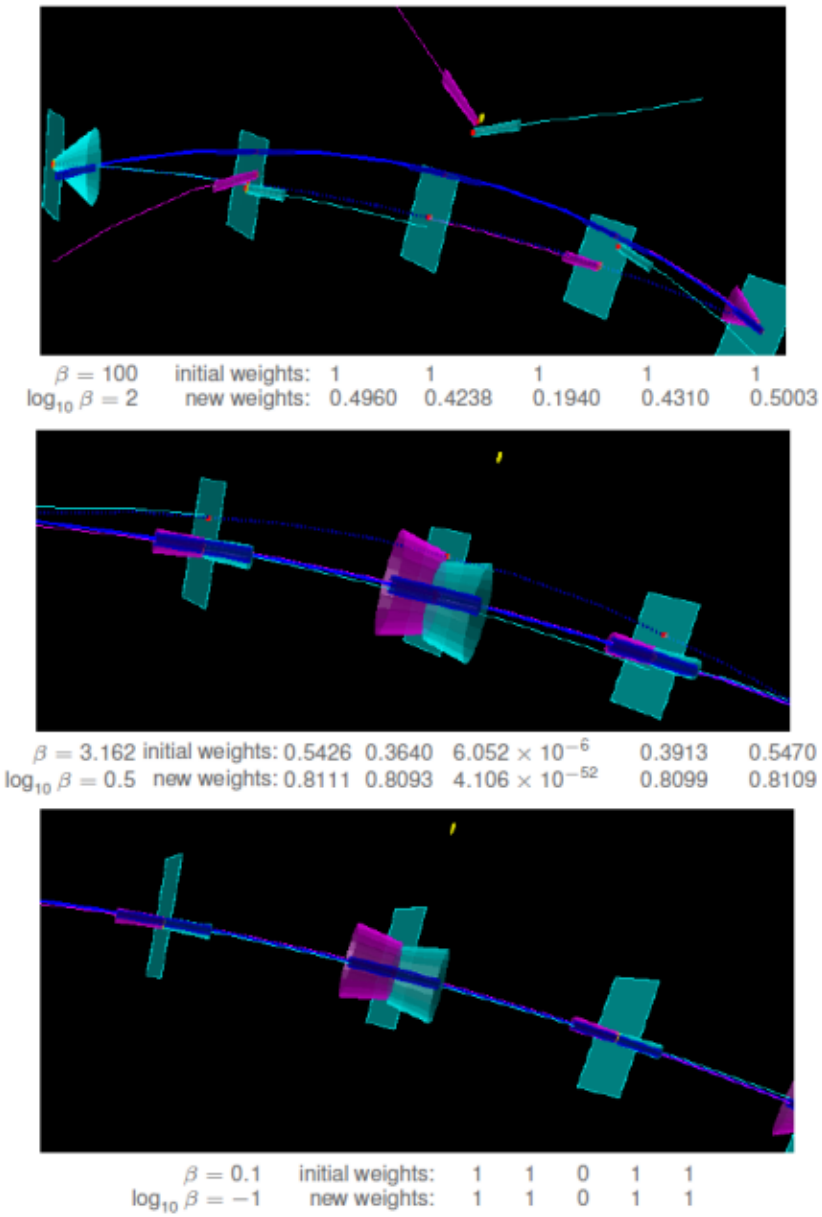


Figure 3.5: The figure shows three steps of the weighting procedure of the DAF. The proper weights are determined by the measurement of the residuals at every interaction. The final step shows the reject of the outlier point.

After the track fitting, the particle momentum can be retrieved from the Kalman filter reconstruction algorithm and the TOF. Moreover, energy release and kinetic energy measurements can be associated to the reconstructed particle.

- **Charge and mass identification:** combining the particle energy loss, kinetic energy, TOF and momentum measurements, the fragment charge and mass identification can be performed as explained in Section 2.6.2.

- **Cross section analysis:** in the final stage, all the information about the particles measurements and the detectors efficiencies are employed to determine the differential cross section measurements.

## The Kalman Filter

The extended Kalman filter is an efficient recursive algorithm that finds the best estimate for the state of dynamic systems from a series of noisy measurements. Since its development, Kalman filter algorithm has had numerous application in technology: a common application is for guidance, navigation, and control of vehicles, particularly aircraft and spacecraft. Kalman filters also are one of the main topics in the field of robotic motion planning and work for the modelling of the central nervous system movement control. Moreover Kalman filter algorithms have been applied to track fitting in high energy physics by many experiments [75].

In the framework of Global Track Reconstruction, the Kalman Filter treats the particle's trajectory as a dynamic system represented by a state vector. It is a progressive method, where the assessment of the track's parameters evolves step by step, incorporating information from each new measurement [76].

The state vector describes the track in each point of its trajectory and it is represented as a p-dimensional vector $\bar{x}_k$where the suffix $k$ stays for the number of the measure's site. The evolution of the state vector $\bar{x}_{k-1}$ is represented by a system equation:

$$\bar{x}_k = f_k(\bar{x}_{k-1}) + w_{k-1} \tag{3.1}$$

where $f_k$ is a non-linear function called *state propagator* (from hit $k-1$ to hit $k$) and $w_{k-1}$ designates random disturbances due to the process noise (e.g. Multiple Coulomb scattering or energy loss). Assuming that the process noise is random and unbiased it results:

$$\begin{cases} \langle w_{k-1} \rangle = 0 \\ Q_k = \langle w_{k-1} w_{k-1}^T \rangle \end{cases} \tag{3.2}$$

whrere $Q_k$ is the covariance.

At each site $k$, the detector measures one or more observables, which form an m-dimensional vector called measurement vector $m_k$. It is a function of the state vector, with the addition of a measurement noise $\epsilon_k$. The relationship between the measurement vector and

the state vector is expressed by the measurement equation:

$$m_k = h_k(\bar{x}_k) + \epsilon_k \tag{3.3}$$

As it was done previously, assuming that measurement noise is random and unbiased it results:

$$\begin{cases} \langle \epsilon_k \rangle = 0 \\ V_k = \langle \epsilon_k \epsilon_k^T \rangle \end{cases} \tag{3.4}$$

In GENFIT, the state vector $\bar{x}_k$ is a 5-dimensional vector containing a track parametrization in plane coordinates:

$$\bar{x}_k = (q/p, u', v', u, v)^T \tag{3.5}$$

where $q/p$ is the ratio between the charge and the momentum of the particle, $u$ and $v$ are the planar coordinates of the detectors, $u'$ and $v'$ are the Tangent directions to the track.

The measurement vector $m_k$ depends on detector type but generally it is a 3-dimensional vector containing hit coordinates. The noise $w_k$ is primarily caused by Multiple Coulomb Scattering and energy straggling, while $\epsilon_k$ is due to electronic noise present in the various detectors.

Given $C_k$ the covariance matrix of $\bar{x}_k$, $Q_k$ and $V_k$, as previously introduced, the covariance matrices of process and measurement noise $w_k$ and $\epsilon_k$ respectively, the Kalman filter finds recursively an estimate $x_k$ for the unknown true state vector $\bar{x}$ of a system.

The Kalman filter works in a two-step process: the prediction step and the update step.

In the *prediction step* the algorithm produces estimates of the state vector at the $k^{th}$ hit, along with the uncertainties, starting from the measurements made at the $(k-1)^{th}$ hit. The state vector is indicated as $x_{k-1}^k$:

$$x_k^{k-1} = f_{k-1}(x_{k-1}) \tag{3.6}$$

and the respective covariance matrix is defined as:

$$C_k^{k-1} = \langle (x_k^{k-1} - \bar{x}_{k-1})(x_k^{k-1} - \bar{x}_{k-1})^T \rangle = F_{k-1} C_{k-1} F_{k-1}^T + Q_{k-1} \tag{3.7}$$

where $F_{k-1}$ is the propagator matrix:

$$F_{k-1} = \left( \frac{\partial f_{k-1}}{\partial x_{k-1}} \right) \tag{3.8}$$

The track parameters are updated as new measurement points are added. Because of this we can take into account a step-by-step the evolution of the track parameters, yet accounting for multiple Coulomb scattering and energy loss through matter. Doing so, the algorithm updates the state vector and the covariance matrix such that the track comes closer to the actual hit than the predicted one did (Figure 3.6).

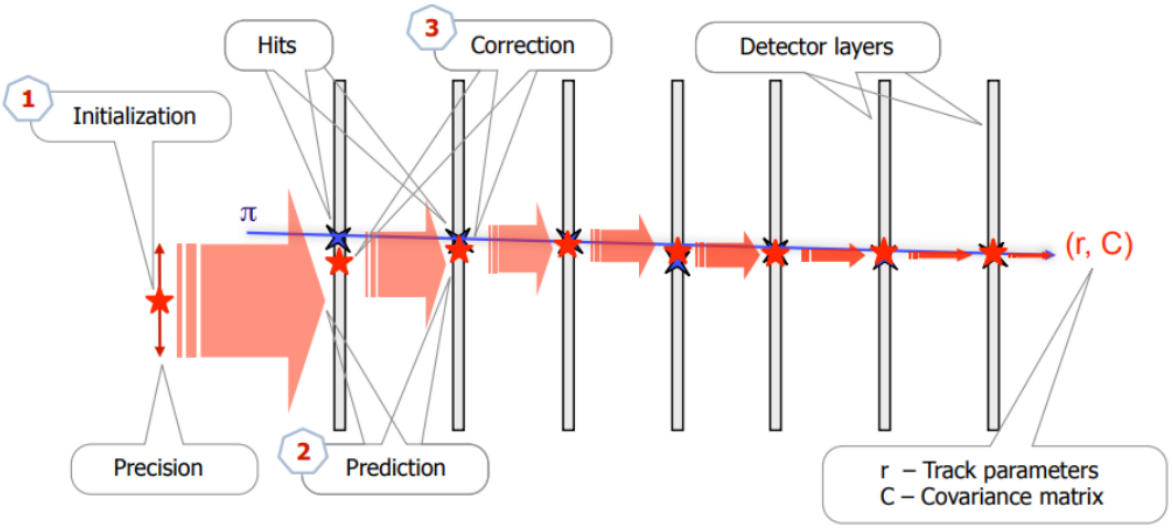


Figure 3.6: Graphic visualization of Kalman filter estimation of the track parameters at one or more hits along the track.

In the *update step* the estimates are updated considering the $k^{th}$ hit information given by the measurement state $m_k$. The state vector becomes:

$$x_k = x_k^{k-1} + K_k(m_k - h_k(x_k^{k-1})) \tag{3.9}$$

where the matrix $K_k$ is called *Kalman Gain Matrix* and represents how the new measurement at the $k^{th}$ site improves the predicted state vector:

$$K_k = C_k^{k-1} H_k^T (V_k + H_k C_k^{k-1} H_k^T)^{-1} \tag{3.10}$$

It depends on the *projector matrix* $H_k$ defined as:

$$H_k = \left( \frac{\partial h_k}{\partial x_k^{k-1}} \right) \tag{3.11}$$

With Equation (3.9) together with Equation (3.10), the predicted state vector $x_k^{k-1}$ can be updated by including the information from the new measurements at $k^{th}$ site and the filtered state vector $x_k$ is obtained.

Accumulation of the measurement vectors improves the estimate of the state of the system: that's why a recurrence formula is needed. The algorithm is recursive and is iterate over all the selected measurements in each layer. After the Kalman filter has been performed on all hits of the track, the reconstruction can still be biased due to wrong starting values, named "seed". This error can be reduced by repeating the procedure backwards, with the iterative algorithm running in the opposite direction of the initial filter, using the previous fit results as starting values. The final "smoothed states" are the weighted mean of the previous predicted states and the updated states of the backwards filter.

## The FOOT track Reconstruction algorithm

The event reconstruction involves the handling of the input and output data from the different detectors in order to obtain the identification of the fragments produced. In the FOOT experiment, the full reconstruction chain for both data and simulated events is performed by a ROOT based framework, developed in the GSI laboratory within the FIRST collaboration. The code uses a hierarchical structure to obtain a solid and simple object-oriented architecture. In order to perform a full event reconstruction and analysis, the SHOE software performs two steps: the first one consists in reading, interpreting and converting in a single format both the data and the simulation events provided in different input formats. Data are given in raw format by the DAQ system, like digitized signals, ascii and dat files; the simulation files are in ROOT n-tuple format. In the second step, events are processed in order to identify the track and extrapolate the needed information for the fragmentation studies and results.

The FOOT reconstruction algorithm is based on the Kalman Filter and relies on the GENFIT code. It takes as input the hit provided by each detector that is crossed by a particle in order to give as output a reconstructed global track.

The reconstruction algorithm has a free parameter, which is the minimum number of hits required for a track to be reconstructed, ranging from a minimum of 5 to 9 for the

considered simulation. To optimize this parameter, two variables are used: efficiency and purity. The efficiency is defined as the number of reconstructed tracks compared to the number of simulated particles generated in the target and reaching the TW:

$$Efficiency = \frac{Number\ of\ reconstructed\ \ particles}{Number\ of\ MC\ Truth\ particles} \tag{3.12}$$

Instead, purity is defined as the ratio between the number of points in a track associated with the particle that generated the most hits (referred to as Main-Track-Id) and the total number of points in the track itself:

$$Purity = \frac{Number\ of\ hits\ in\ the\ track\ associated\ to\ the\ Main-Track-Id\ particle}{Total\ number\ of\ hits\ in\ the\ track} \tag{3.13}$$

Efficiency and purity take values between zero and one: the goal is to choose a value for the minimum number of points that maximizes both. It is expected that as the minimum number of points increases, efficiency decreases because the number of reconstructed tracks will be lower. On the other hand, increasing the minimum number of points means increasing purity because the more points there are, the more likely they are associated with the same particle.

Once a properly number of hits is set to reconstruct the track, the algorithm initiates the creation of an initial track using the space point from the VXT. Subsequently, it updates the track fit using the measurements from the following detectors. The final point associated with the track is that of the TW, from which the charge can be measured. In cases where a magnetic field is present, it's possible to also measure the particle's momentum.

This process is the same whether dealing with real data or data from a MC simulation. If the track reconstruction is performed on a MC sample, each reconstructed track contains also all the relevant MC information. In this case, it is known exactly which particle generated a specific hit allowing the association between the reconstructed track and the MC particles. When a single track is generated by different particles, the track is automatically associated to the particle (identified by the Main-Track-Id) that generates the most hits.

# 4 | MC study of $\alpha$ clustering fragmentation in the FOOT experiment

## 4.1. Introduction

The work of this Master thesis is focused on on the possibility to investigate $\alpha$ clustering phenomenology using the FOOT experiment, in particular by detecting $\alpha$ particles and measuring their correlation generated from the two decay channels of $^{12}$C.

The analysis is dived into two main fields of study. In the first one it is examined the opening angle between pairs of detected $\alpha$ particles generated from a single event. The aim is to understand the impact of the production of $^{8}$Be during the $^{12}$C decay. The second analysis consists in the examination of the excitation energy of the $^{8}$Be from the study of the detected pairs of $\alpha$ particles.

In pursuit of these objectives, a MC simulation was executed using the FLUKA code. The simulation involved a primary beam of carbon ions with a kinetic energy of 200 MeV/u impinging on a carbon target. The analysis encompassed five million events within the complete configuration of the FOOT experiment, as described in Section 2.5. All detector efficiencies and functionalities were taken into account in the simulation. One of the omitted aspect was the background noise, which, by the analysis of some data taken in previous years, emerge that it should not affect the results of the study significantly.

In Section 4.2 is described the setup for the experimental simulation followed by the the definition of the analysis's strategy in Section 4.3. Results on the angular separation and excitation energy investigations are reported in Section 4.4 and Section 4.5 respectively.

## 4.2. The full MC simulation of the experimental setup

The complete experimental setup described in Section 2.5 has been implemented in the MC simulation in the FOOT experience to properly take into account all the interactions of the particles with the whole apparatus. Since the distance between target and TW is set to 1.75 m, the maximum accessible polar angle will not allow to contain all the Z=2 fragments, given their wide angular distribution (see Figure 2.4). The TW angular acceptance in the chosen geometry is approximately of 10°.

The whole experimental setup is shown in the Figure 4.1 where are illustrated both simulated tracks of the MC primary particles that do not fragment on target and the $\alpha$ particles generated from interactions on target of primary particles.

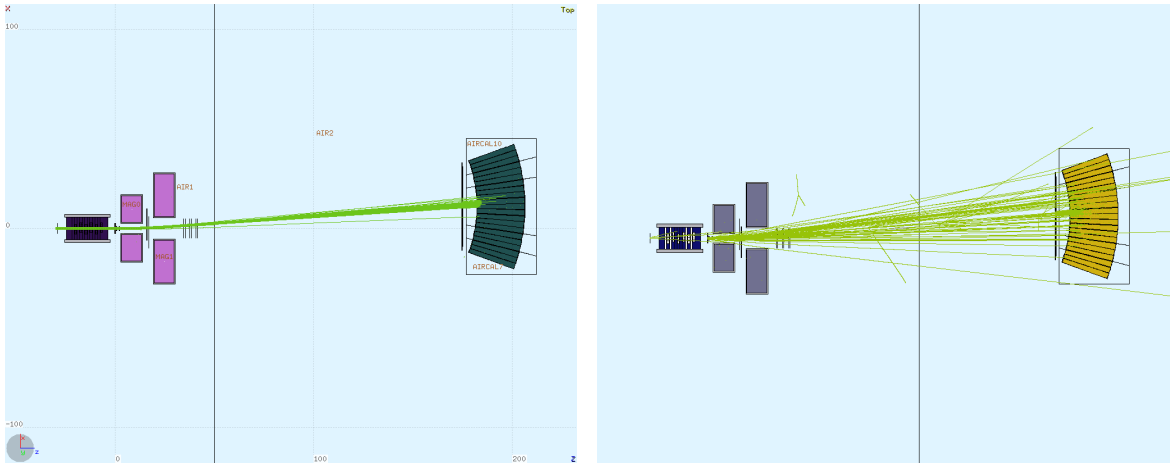

Figure 4.1: Simulated MC tracks of primary particles (left) and $\alpha$ particles (right). Their relative angular distribution and the detector's angular acceptance is shown.

## 4.3. Strategy of analysis

The simulation is divided in two parallel analyses:

- The MC *Truth* analysis consists in the study of the MC simulated particles without any effect due to detection and reconstruction. From this investigation, the information relative to all the particles produced during the simulation are stored. Here, one can retrieve the particle's mass, charge, barionic number, position and momentum at the production and at the death. All the primary and secondary particle chain is accessible. It is also possible to obtain information each time the particle crosses a boundary of a region defined in the FLUKA geometry as the space volume having a homogeneous material. These retrieved data consist in the coordinates

and complete kinematics of particles at the crossing position and a pointer to the particle block.

- In the *Reconstruction* analysis, the reconstructed algorithm described in Section 3.3 is applied. The minimum number of hits for which a track can be rebuilt has been set equal to 7 to maximise the quality of the reconstructed tracks without decreasing the reconstruction efficiency, defined as the ratio between the number of reconstructed tracks and the number of simulated particles, as shown in Figure 4.2. The analysis is in turn divided into three sub-analyses, which differ in the level of information acquired from the MC:
  - In the first one it has been asked to select all the particles between the ones that have been generated in the target from a primary particle. In addition, the MC charge of the associated particle has been assigned to the reconstructed track to exclude the effect of the mis-identification of the charge reconstructed by the TW.
  - In the second one, the first requirement of the previous analysis has been maintained while the charge is taken from the reconstruction.
  - In the third analysis all the MC information has been eliminated. In this way, real experimental conditions have been simulated.

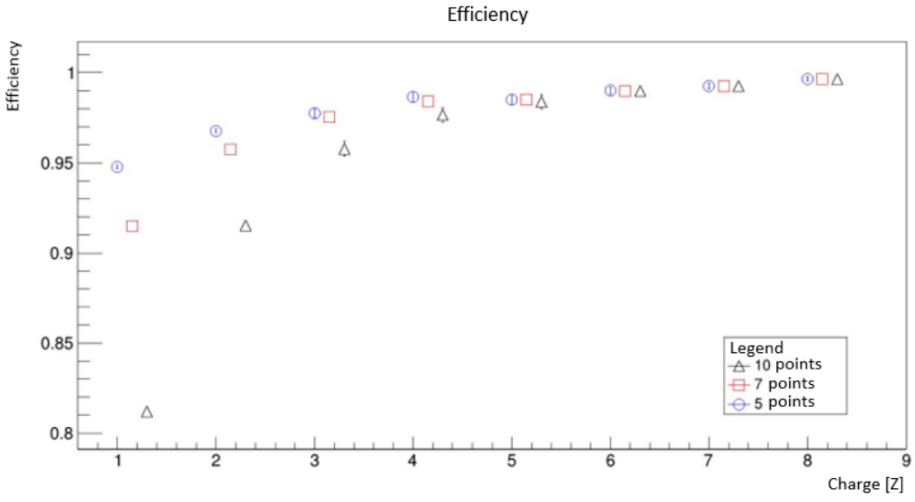


Figure 4.2: Efficiency per charge for different minimum point numbers. The markers have been shifted to the right compared to the original position to enhance a better view of the graph [77].

### 4.3.1. Selection of $\alpha$ particles

From the MC *truth* analysis it is investigated the production kinetic energy distribution of the $\alpha$ particles arriving on TW shown in Figure 4.3. It can be seen that the $\alpha$ particles produced on target and arrived on TW have at least 25 MeV/u initial energy. It is chosen to impose a threshold at 50 MeV/u in the selection of $^4$He nuclei.

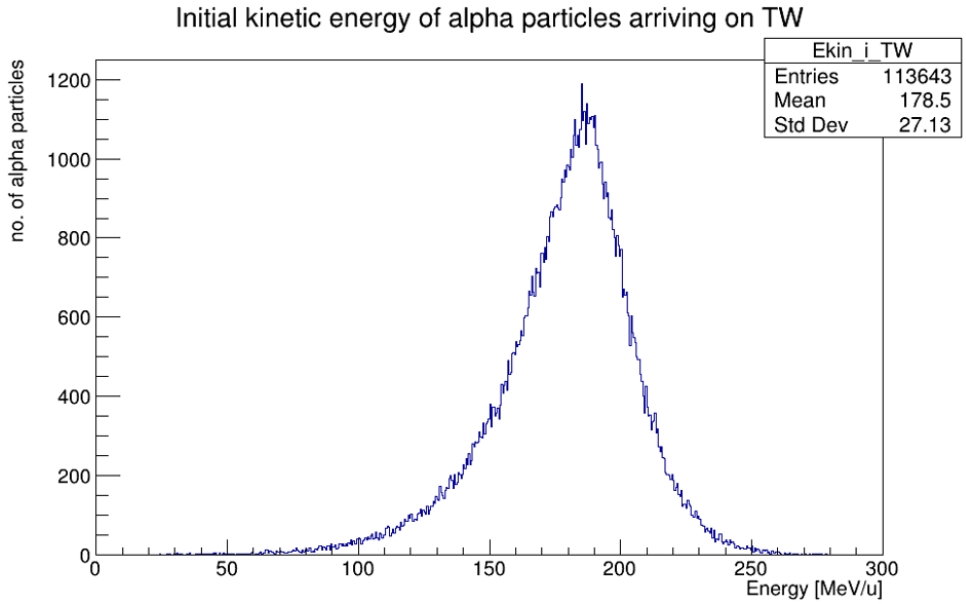


Figure 4.3: Initial kinetic energy distribution of $\alpha$ particles generated on target that arrive on TW from the MC Truth analysis.

### MC Truth $\alpha$ particles selection

The particles that will be analyzed are the ones generated by the primary fragmentation on target and then tracked by the different detectors up to the TW. For this reason, it is asked that the particle must be generated from a primary particle and that the production and final detection regions must be respectively the target and the TW. It is required that the particle is forward directed, which means that its initial momentum must be positive. The maximum polar angle is set equal to 10° to approximately reproduce the TW acceptance. The initial energy is required to be $>$ 50 MeV/u as seen previously. The charge and the baronic number are selected to be equal to 2 and 4 respectively in order to analyse only the $^4$He.

## Reconstructed $\alpha$ particles selection

From what concerns the *Reconstruction analysis*, the information about the true particle corresponding to the reconstructed track is not unambiguously available. It is possible to associate the reconstructed track to the most probable MC particle, which is the particle that has generated the highest number of hits of the track. Since the the true mass number cannot be retrieved, it is chosen to perform the $\alpha$ particle selection through the available information about the mass. Figure 4.4 shows the reconstructed mass distribution for the reconstructed particles with the reconstructed charge $Z_{rec} = 2$. It can be identified the primary peak centred on the $^4$He mass equal to 3.73 GeV/$c^2$. In order to consider only $^4$He, it is chosen to select the reconstructed $\alpha$ particles which possess a mass between 3.2 and 4.3 GeV/$c^2$ from the FWHM of the nominal peak.

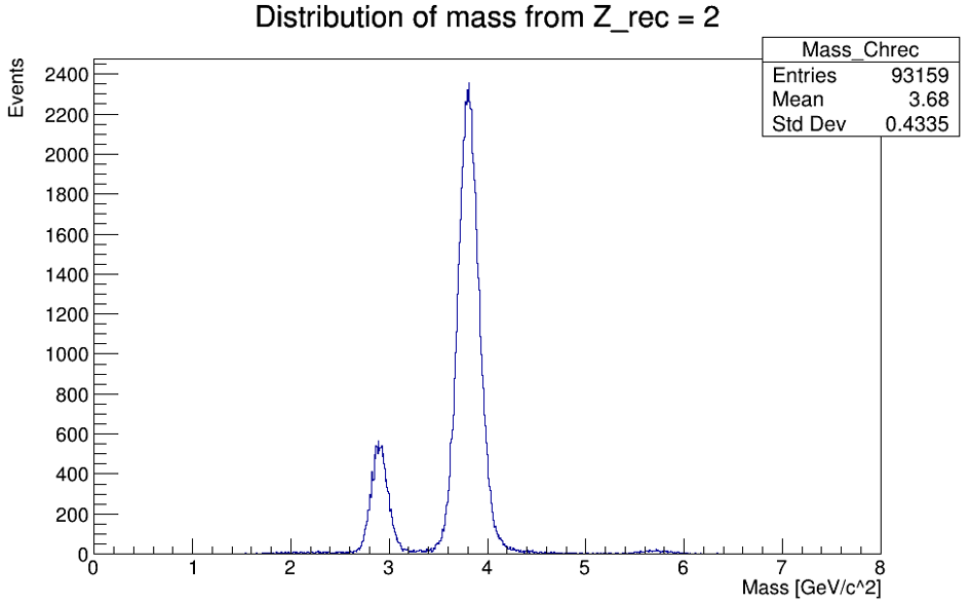


Figure 4.4: Mass distribution of the reconstructed particles with the reconstructed charge $Z_{rec} = 2$ generated on target that arrive on TW from the Reconstruction analysis.

### 4.3.2. $\alpha$ reconstruction efficiencies

As described in Section 3.3, the global reconstruction algorithm processes the information from all the detectors (local level) to reconstruct the whole event (global level). It is then possible to evaluate the total efficiency of the FOOT tracking system in reconstructing particles, in particular $\alpha$ particles for our purposes. The evaluation is conducted on clean events: background events with a nuclear inelastic interaction of the projectile in the detectors before the target (in the SC or the BM) are neglected. Three different efficiency calculations were performed.

The efficiencies are defined as the ratio between the total number of reconstructed $\alpha$ associated to a MC particle and the total number of MC $\alpha$ particles generated on target and detected by the TW:

$$Eff = \frac{Number\ of\ reconstructed\ \alpha\ particles}{Number\ of\ MC\ \alpha\ particles} \tag{4.1}$$

What distinguishes the three calculations are the hypotheses on the charge selection and whether the MC information on the number of the reconstructed $\alpha$ particles is included or not.

In particular, they are calculated as:

$$Eff_1 = \frac{No.\ of\ reconstructed\ \alpha\ from\ MC\ charge\ selection}{No.\ of\ MC\ \alpha\ particles} = 84.7\% \tag{4.2}$$

$$Eff_2 = \frac{No.\ of\ reconstructed\ \alpha\ from\ reco\ charge\ selection}{No.\ of\ MC\ \alpha\ particles} = 67.2\% \tag{4.3}$$

It can be seen that the efficiency increases when the charge selection is performed through the MC Truth charge associated to the reconstructed track. The second efficiency is affected by the mis-identification of the charge measured in the TW from the reconstructed algorithm.

$$Eff_3 = \frac{No.\ of\ reconstructed\ \alpha\ from\ reco\ charge\ selection\ (No\ MC\ info)}{No.\ of\ MC\ \alpha\ particles} = 74.2\% \tag{4.4}$$

The $Eff_3$ is calculated by taking as numerator the number of reconstructed $\alpha$ particles without imposing the production region and without considering only secondary particles produced by the primaries impinging on target. This can lead to count also $\alpha$ particles crossing the TW generated outside the target by multiple collisions. For this reason $Eff_3$ results slightly higher than $Eff_2$ with the disadvantage that the measurement is contaminated by undesired particles.

### 4.3.3. Reconstruction performances

For each reconstructed fragment, the MC information has been accessed to check whether the charge reconstructed by the TW and the reconstructed momentum were matching the

true values.

For the study of the charge reconstruction accuracy, the so called *mixing matrix*, shown in Figure 4.5, is implemented. It compares the reconstructed charge (x axis) versus the true one (y axis). The non diagonal elements of the matrix indicate the number of mis-reconstructed charges for each fragment type. If the reconstruction procedure assigns the $Z_{reconstructed}$ equal to 2, there is 1.84% possibility that it fails to well recognize the particle.

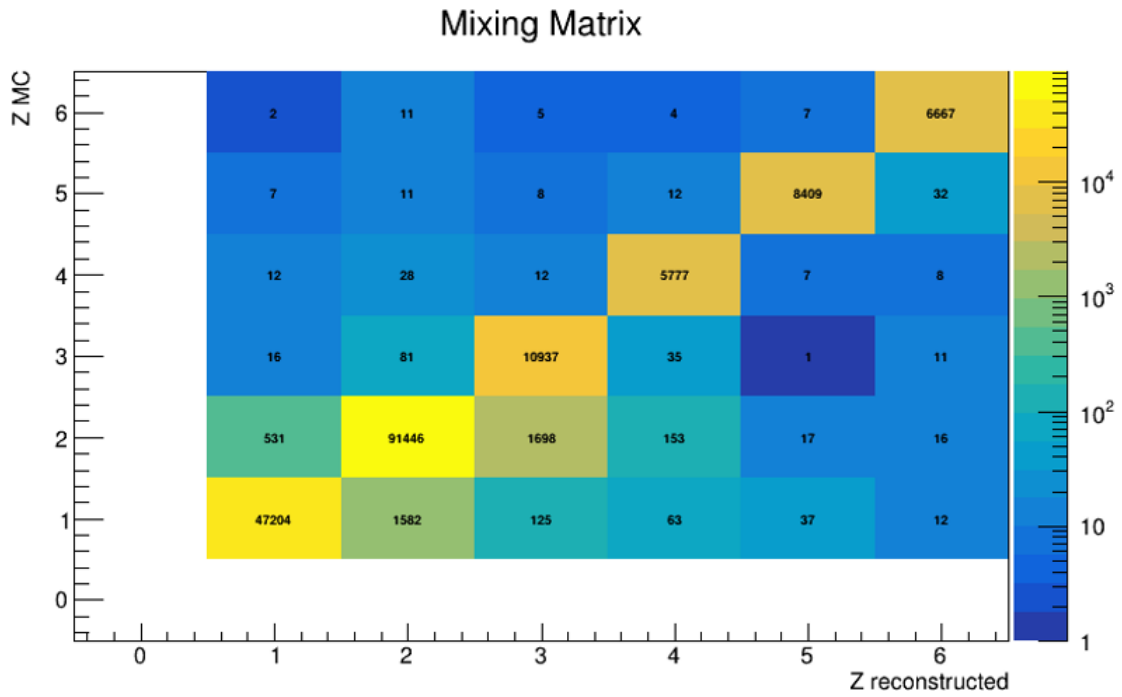


Figure 4.5: Correlation between the charge reconstructed by the TW (x axis) and the MC charge (y axis).

For the study of the momentum reconstruction accuracy, it is examined the difference between the reconstructed track momentum and the MC one, both calculated at the exit of the target:

$$\Delta P = P_{reconstructed} - P_{MC} \tag{4.5}$$

The evaluation has been conducted for all the detected $\alpha$ particles. Then, the momentum resolution distribution has been fitted with a Gaussian. The standard deviation of the Gaussian represents the momentum resolution of the $\alpha$ particles reconstructed track. The result is shown in Figure 4.6.

It has to be noticed that the the difference of the modulus of momenta is not centered in zero, but there is a shift of the peak towards the positive direction of the x axis, meaning

the presence of a systematic overestimation of the reconstructed momentum with respect to the MC value. The causes of it are currently under study.

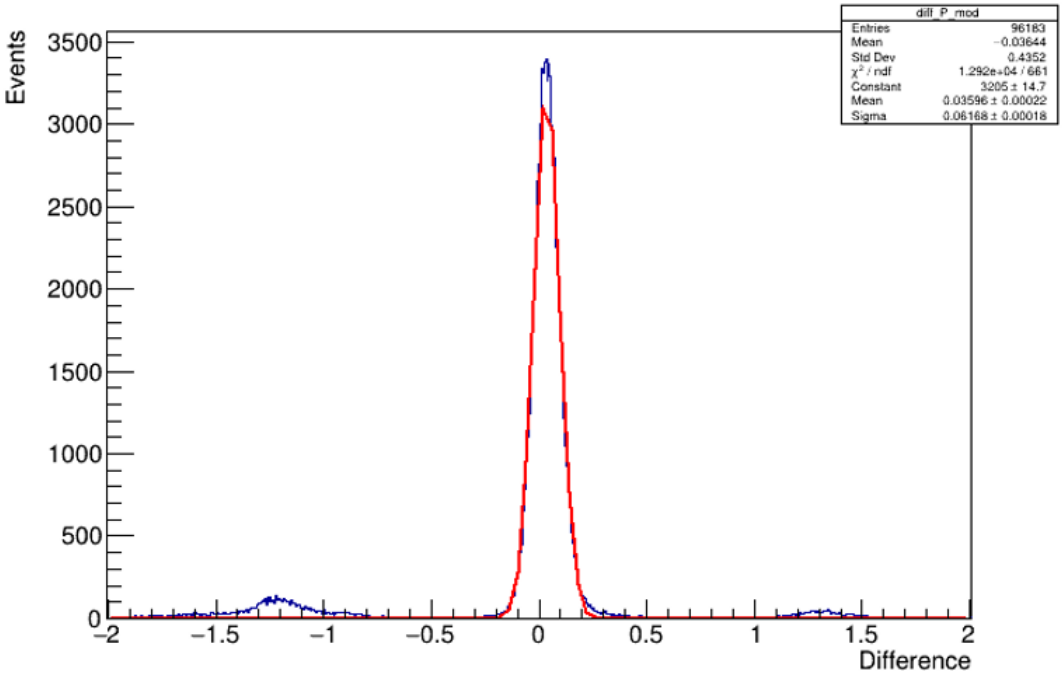


Figure 4.6: Difference between the modulus of reconstructed and MC momenta. In red is reported the Gaussian distribution.

### 4.3.4. Analysis development

The produced $\alpha$ particles multiplicity per event is shown in Figure 4.7 for both the MC Truth and Reconstruction analyses.

On the left are represented events from the MC truth analysis where $\alpha$ particles are originated from the fragmentation of a primaries on target. A good portion of events generates zero alpha particle that can be detected on TW. This because, as described in Section 2.4, the probability that the primary particles interact in the target generating a subsequent fragmentation is low. Out of 5 million primaries, the events with inelastic interaction in the target are 182250.

The most interesting events for our research purposes, consist in the generation of pairs or triplets of $\alpha$ particles in the same event.

The corresponding analysis is reported on the right representing the reconstructed events. It can be noted that the number of events which produce more than one $\alpha$ particle is higher than the MC Truth. This can be attributed to the mis-identification of particles

for which different particles are reconstructed as an $^4$He or to the fact that we are detecting $\alpha$ particles produced also out of target. The resulting increase of the number of wrong particles under investigation leads to an addition of the blurring signal to the analyses.

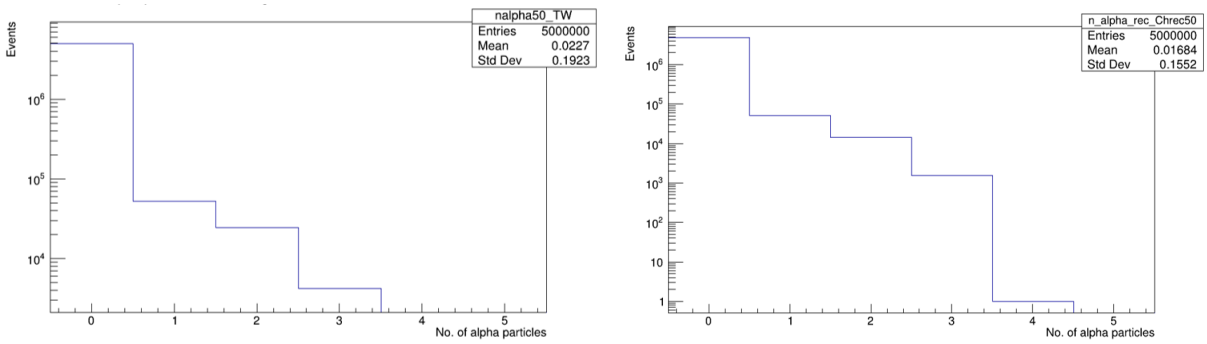


Figure 4.7: $\alpha$ particles multiplicity per event in MC (right) and Reconstruction (left) analyses in logarithmic scale.

The subsequent investigation focuses on the study of events in which two or three $\alpha$ particles are produced. The first objective is to examine the existence of an angular correlation between pairs of $\alpha$ particles. What is expected is an appearance of a narrow peak at lower opening angle due to the decay of $^8$Be produced by interactions of Carbon ion projectile. A further analysis is conducted to investigate the excitation energy of $^8$Be and $^{12}$C nuclei from the properties of the two or the three final-state $\alpha$ particles, respectively.

## 4.4. Angular Separation Analysis

In this section, the investigation of the opening angle distribution starting from the selection of events producing two or three $\alpha$ particles is performed.

The differences in angle between pairs of $\alpha$ particles are calculated by taking into consideration the momentum of each particle constituting the analysed pair. Defining the modulus of the momentum $p_k$ of particle $k$ starting from its momentum component in the Cartesian reference system $P_x$, $P_y$, $P_z$:

$$p_k = \sqrt{P_{x_k}^2 + P_{y_k}^2 + P_{z_k}^2}; \tag{4.6}$$

it is possible to measure the difference in angle $\Delta\Theta$ between particles $i$ and $j$ :

$$\Delta\Theta = \arccos\left(\frac{P_{x_i}P_{x_j} + P_{y_i}P_{y_j} + P_{z_i}P_{z_j}}{p_i p_j}\right) \tag{4.7}$$

The resulting angular separation distribution of the emitted $\alpha$ particles from the target in the MC truth analysis is plotted in Figure 4.8.

In both graphs there is evidence of an excess of events below 2° constituting a narrow peak centered at $\sim 0.6°$, which corresponds to the expected value for the fragments originating from the decays of ${}^{8}Be_{g.s.}$. A second broad peak is present at larger opening angles which can be attributed to the ${}^{8}Be^{*}_{3.03}$ promptly decaying into two $\alpha$ particles. In this peak are included also the $\alpha$ particles which are not generated by the ${}^{8}$Be decay.

Calculating the number of events in the two peaks, it results that the contribution of the narrow peak at low opening angle is respectively equal to 22.71% and 28.21% for events producing two and three $\alpha$ particles. By comparing the plots, it can be noted that the height of the primary peak is lower for events with three $\alpha$ particles production. This is due to the lower probability of three $\alpha$ generation from the collision of the primary particle on target. This fact can be observed by comparing the entries, corresponding to the number of events characterized by the fulfilment of the requirements previously described. In addition, from the comparison of the two angular distributions, the broad peak results wider in events with only two $\alpha$ particles production: the maximum difference in angle approaches the maximum angular aperture imposed by the experimental setup (about 20°) in case of generation of two ${}^{4}$He, while in case of three $\alpha$ particles production it is at $\sim 14°$. It can be assumed that the broad peak is shifted on the left at lower opening angles. This phenomena can impact the calculation of the relative area under the peaks previously illustrated, resulting in an increase of events under the primary peak when we deal with the production of three $\alpha$ particles.

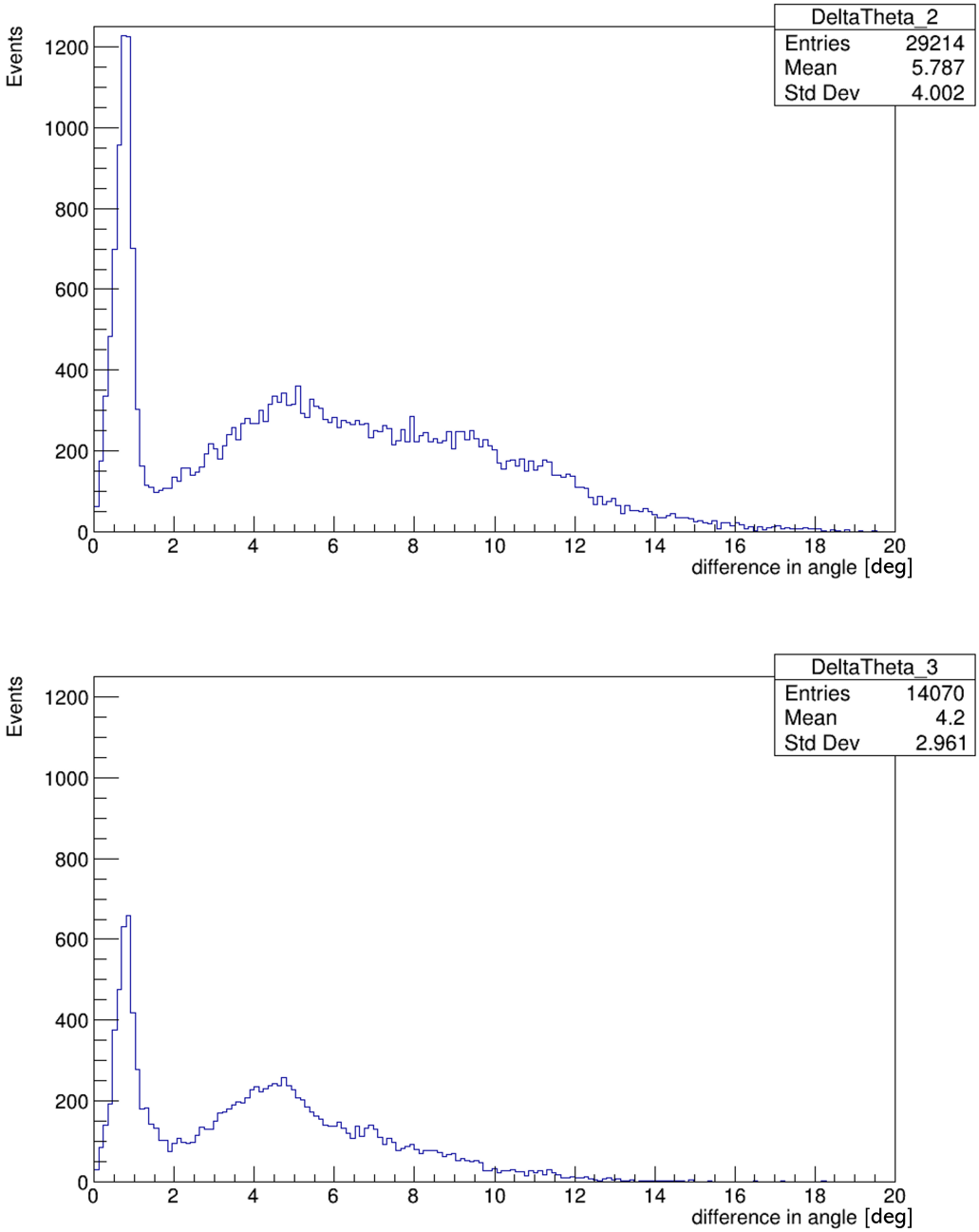


Figure 4.8: Opening angle between pairs of MC simulated $\alpha$ particles at target from events producing two (top) and three (bottom) $\alpha$ particles.

Considering events producing two and three $\alpha$ particles together, the angular distribution between all the pairs of $\alpha$ particles produced in a single event is plotted in Figure 4.9.

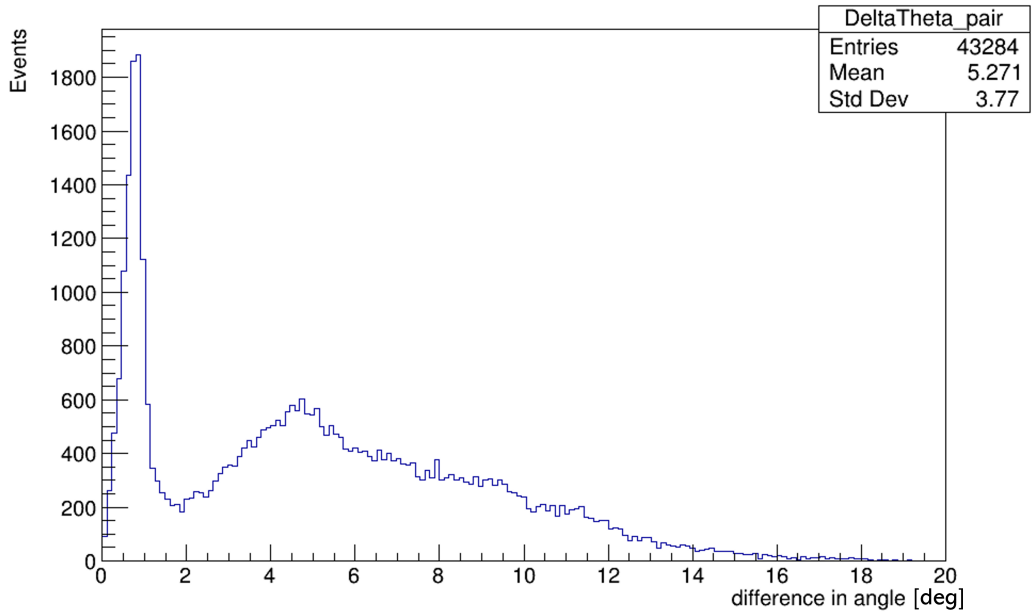


Figure 4.9: Opening angle between pairs of MC simulated $\alpha$ particles at target from events producing two and three $\alpha$ particles together.

Since the previous graphs are generated taking into account the angular distribution in the momenta of $\alpha$ particles generation at the target exit, it is now important to understand if this distribution degrades when analysed at different layers of the FOOT experimental detector. In particular, the analysis is conducted at layers progressively farther from the target. Information of particle momentum on VTX, MSD and TW has been retrieved and plotted in Figure 4.10.

Moving progressively away from the target, the primary narrow peak decreases in amplitude and increases in width. This means that pairs of $\alpha$ particles emitted with a small angular separation increase their difference in angle on their way to TW. Scattering phenomena during the path of $\alpha$ particles can explain this experimental evidence: the particle can modify its direction by nuclear interactions. The consequent opening angle distribution at TW results blurred by originally correlated $\alpha$ particles that lose their small angular aperture due to the distance of the TW from the target. In fact, posing the TW at 1.75 m from target increases the interaction probability of the emitted particles with the medium in the space between production and detection. It can be noted also that the number of entries deceases passing from the target to the TW. This is due to the fact that a consistent portion of $\alpha$ particles is lost during the particle's path, lowering the detected $\alpha$ particles' statistic.

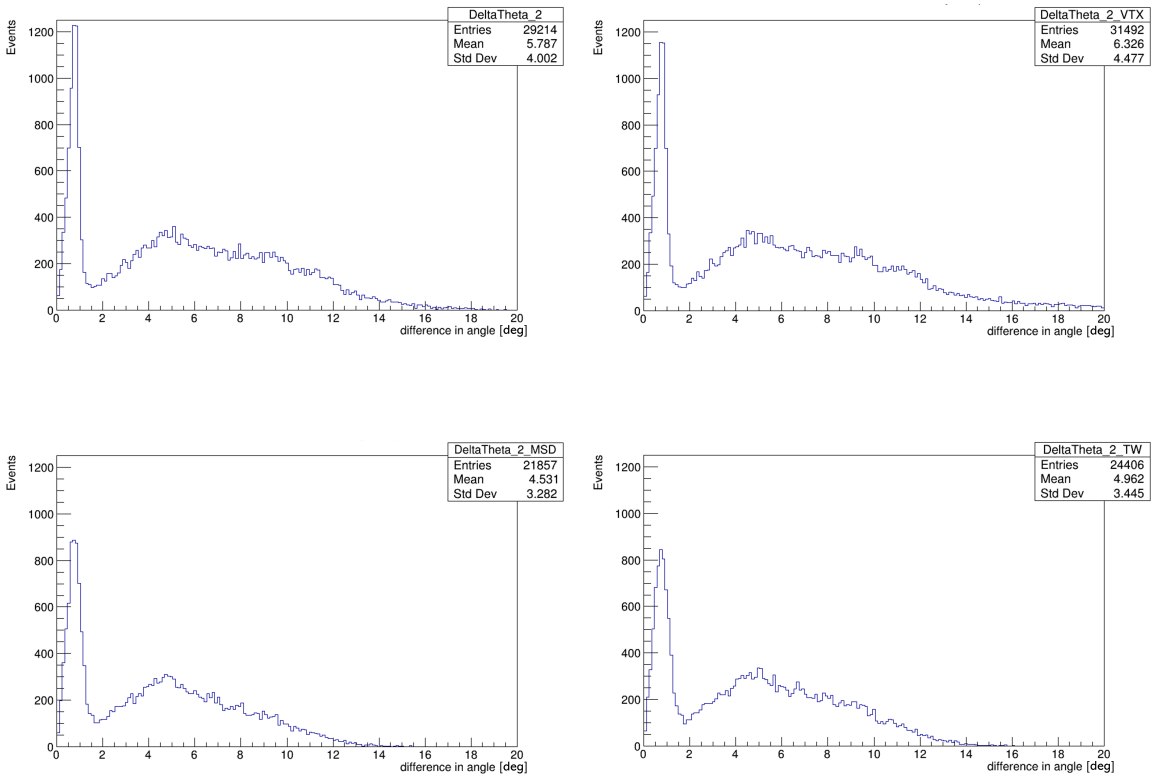


Figure 4.10: Opening angle between pairs of MC simulated $\alpha$ particles from events producing two $\alpha$ particles at target (top left), VTX (top right), MSD (bottom left), TW (bottom right).

The same angular distribution investigation is performed on the reconstructed data sample. Taking into account the reconstructed $\alpha$ particles detected at TW with the reconstructed charge selection and without imposing the region of origin and the parent particle, the angular difference distribution is shown in Figure 4.11.

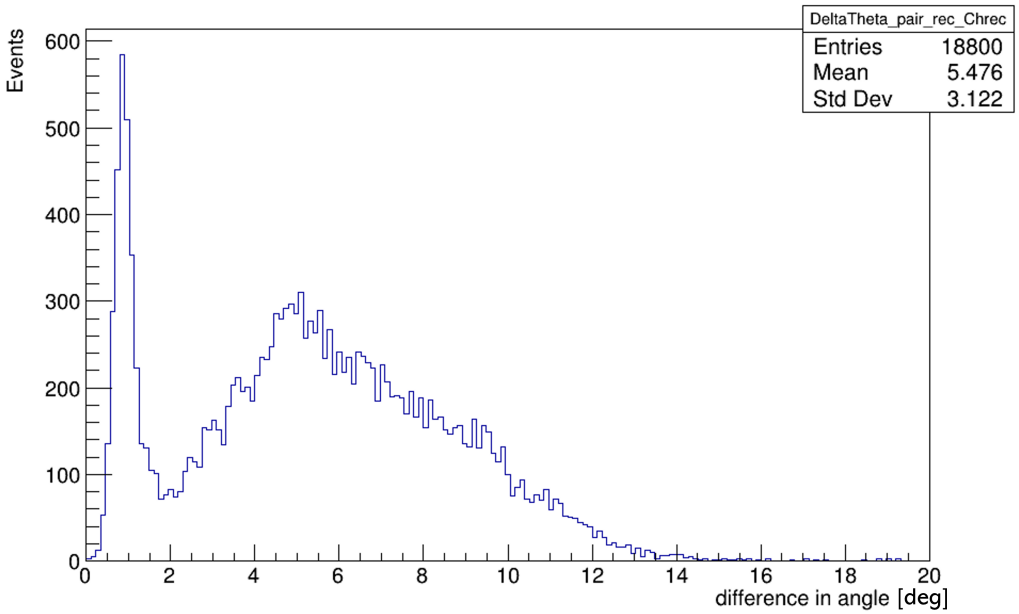


Figure 4.11: Opening angle between pairs of reconstructed $\alpha$ particles at TW from events producing two and three $\alpha$ particles together.

It is possible to obtain the same angular distribution of the MC truth analysis with the visible main peak at a lower angular difference indicating the existence of an angular correlation between the generated $\alpha$ particles.

The area under the narrow $\Delta\Theta$ peak covers the 17,47 % of the detected events. The consistent reduction of the number of $\alpha$ particles detected with a lower angular separation can be attributed to the problem of reconstruction efficiency.

The detector's geometrical efficiency is defined as the ability of the instrument to distinguish more than one particle arriving on the detector at the same time. In the FOOT experimental setup two different situations lead to a reduction in resolution. The fist one is the case in which two (or more) different particles arrive on the same TW bar. Due to how the system has been designed, it is not able to detect any of these particles. The second case takes into consideration two different particles arriving on the same TW bar but the reconstruction software fails to track one of the two. In this case, only one particle is detected. Both situations contribute to the loss of $\alpha$ particles that, crossing the same TW bar, are assumed to have a small angular separation from each other.

To demonstrate this hypothesis, the angular difference distribution from the MC Truth analysis between all the pairs of $\alpha$ particles impacting on the same TW bar is reported in Figure 4.12. It is evident for the primary peak that most of the particles which hit the same TW bar exhibit a lower angular aperture between them.

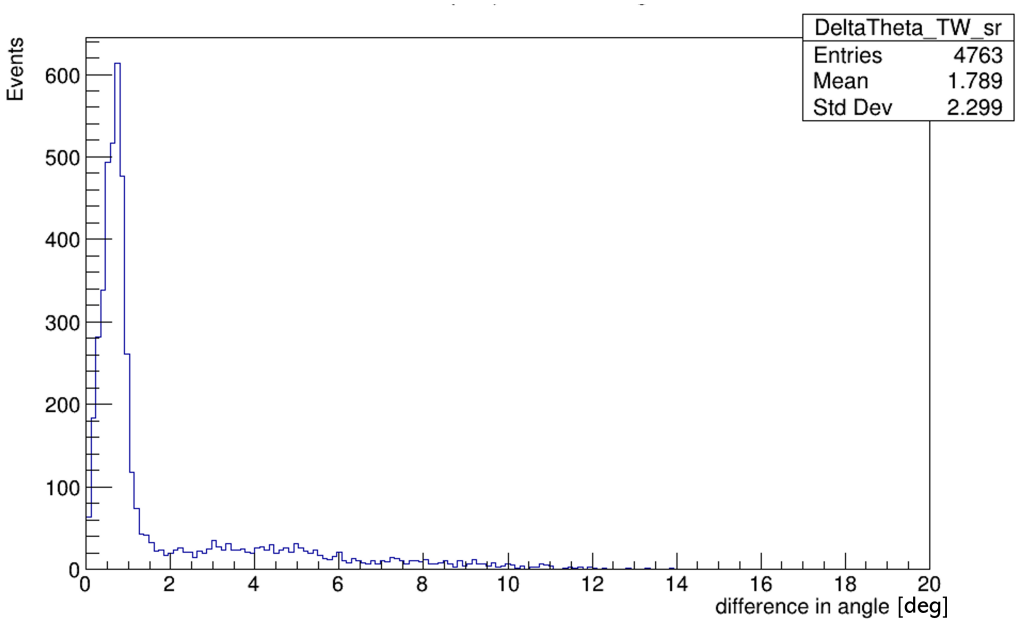


Figure 4.12: Opening angle between pairs of MC $\alpha$ particles at TW impacting on the same TW bar from events producing two and three $\alpha$ particles together.

Having demonstrated so far the existence of an angular correlation between the $\alpha$ particles due to the presence of a peak at low aperture angles, it is necessary to verify, as already proved by De Lellis [25], that the narrow $\Delta\Theta$ peak is not present when calculating the angular distribution between an $\alpha$ particle and particles other than $^4$He.

In the realm of the MC Truth simulation, two other angular distributions on target have been performed: the first one is between $\alpha$ and $^1$H particles, and the second one is between an $\alpha$ and particles other than $^4$He. All the particles under investigation are originated by the fragmentation of primary particles on target. The results are illustrated in Figure 4.13.

No peaks at lower angular apertures are visible in both graphs demonstrating the absence of the angular correlation between the particles taken into account. However, the peaks emerging from the two plots are particularly interesting and they require further investigation. The most significant one is the first peak in the $\alpha$-$^1$H angular distribution: given the high probability of clustering, it could be possible that the proton is generated by an $\alpha$ particle subsequently broken from an $\alpha$ clustering event.

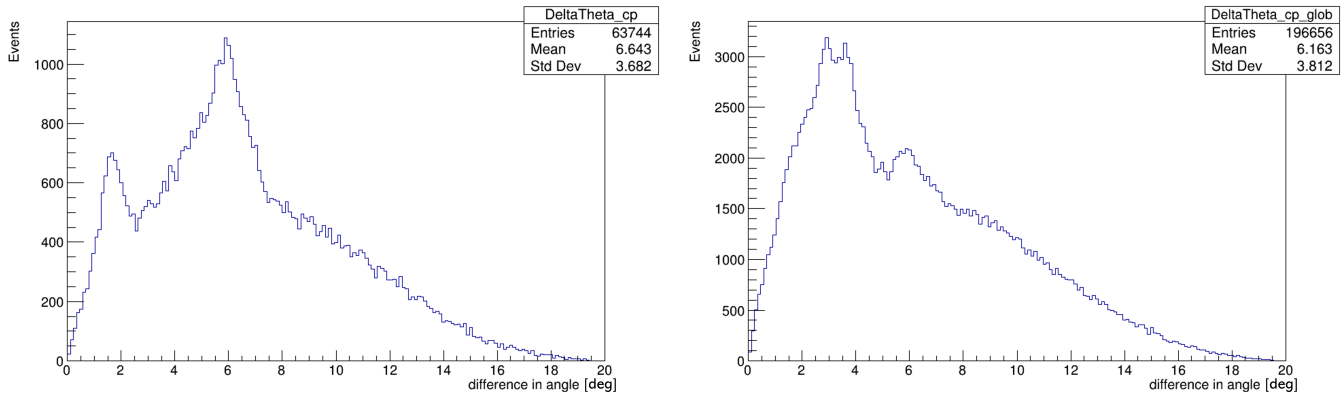


Figure 4.13: Opening angle on target between MC simulated $\alpha$ and $^{1}$H particles (left) and between $\alpha$ and particles other than $^{4}$He (right).

The opening angle distribution between $\alpha$ and particles other than $^{4}$He is reported also for reconstructed events with the same MC results but with different peaks shown in Figure 4.14.

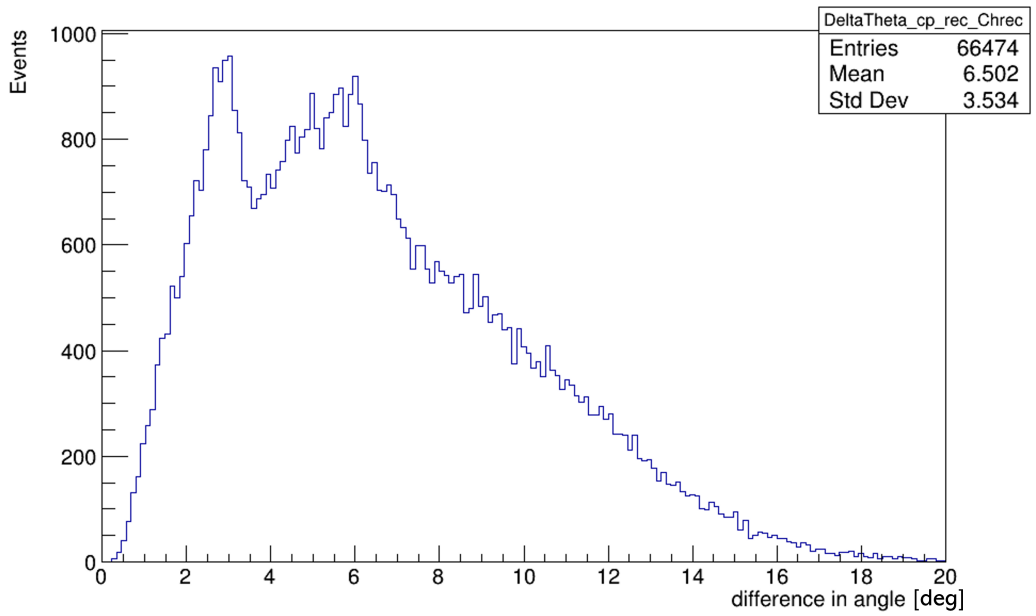


Figure 4.14: Opening angle on TW between reconstructed $\alpha$ and particles other than $^{4}$He.

## 4.5. Excitation energy Analysis

The excitation energies of $^{8}$Be may be reconstructed from the kinematics of the detected $\alpha$ particles. The calculation of excited energy enables the acquisition of information regarding the energy distribution of excited states that are populated during a breakup

reaction.

## $^8$Be excitation energy

For the analysis of the $^8$Be excitation energy, events participating at the reaction $^{12}$C($\alpha$,$^8$Be) have been investigated. For this reason, only events producing two $\alpha$ particles are taken into account. It is expected that the $^8$Be originated through the breakup of $^{12}$C is produced in excited energy states. Their information can be retrieved by the detection of the two consequently emitted $\alpha$ particles from the $^8$Be decay.

By knowing the initial kinetic energies $E_{kin}$ and the 3-momentum $\bar{p}$ at the time of emission of the two $\alpha$ particles $i$ and $j$, the $^8$Be excitation energy can be retrieved from the c.m. energy of the 2 $\alpha$'s. This can be obtained from their invariant mass:

$$^{8\text{Be}}E_{ex} = \sqrt{(E_{kin_i} + E_{kin_j} + 2m_\alpha)^2 - (\bar{p}_i + \bar{p}_j)^2} - 2m_\alpha \tag{4.8}$$

where $m_\alpha$ is equal to 3.73 GeV/$c^2$.

The resulting $^8$Be excitation energy spectrum from MC Truth analysis is reported in Figure 4.15.

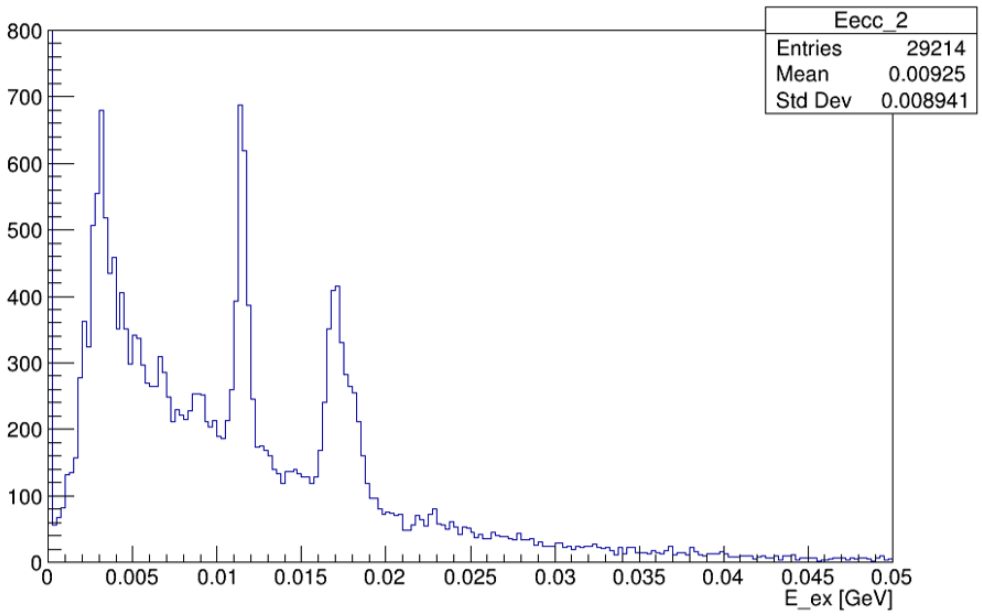


Figure 4.15: Excitation energy spectrum for the breakup of $^8$Be intermediate stage of $^{12}$C into two $\alpha$ particles from MC $\alpha$ particles analysis.

Peaks corresponding to the energies of the excited states of $^8$Be clearly emerge in the plot. The excitation levels implemented in FLUKA are typically the first three of each

nucleus. The minimum excitation energy for a $^{8}$Be to dissociate into two $\alpha$ particles is 92 keV and its contribution is visible on the first narrow peak near the y axis. The first $^{8}$Be excited state at 3.03 MeV and the second one 11.4 MeV are respectively represented by the second and third peak. A forth peak can be associated to the conglomerate of excited states at about 17 MeV shown in the diagram of the $^{8}$Be energy levels in Figure 1.10.

Still at the level of MC Truth analysis, the angular separation distribution and the excitation energy one have been incorporated in Figure 4.16.

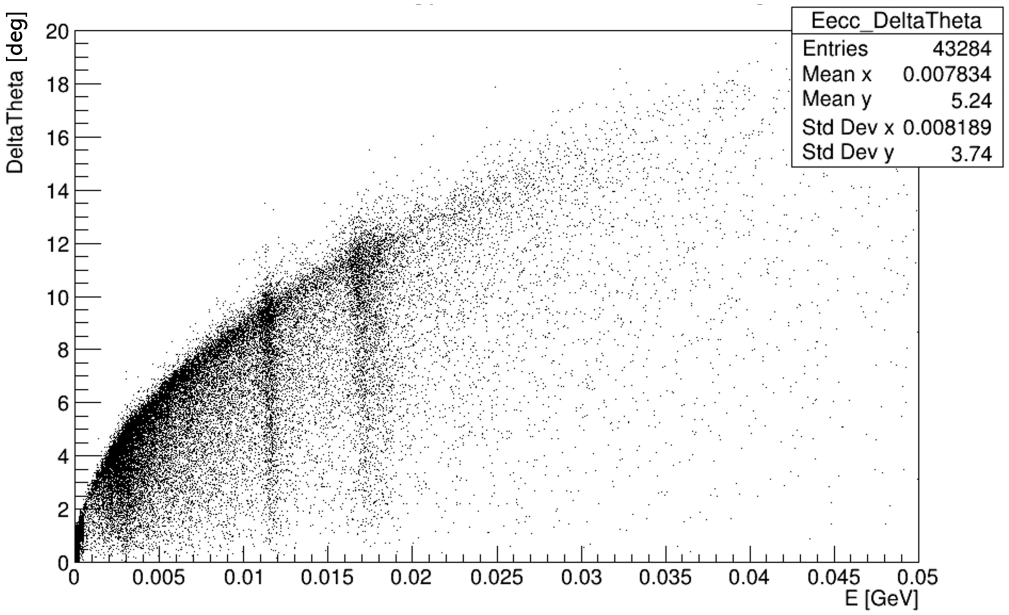


Figure 4.16: Excitation energy spectrum of the breakup of $^{8}$Be intermediate stage of $^{12}$C into two $\alpha$ particles VS the opening angular distribution between $\alpha$ particles in the MC Truth analysis.

It can be noted that the plot has a parabolic shape. Starting from the Equation 4.8 is possible to retrieve the relation between the excitation energy and the $\Delta\Theta$ following the proposed calculations:

$$^{8\mathrm{Be}}E_{ex} = \sqrt{(E_{tot_i} + E_{tot_j})^2 - (\bar{p}_i + \bar{p}_j)^2} - 2m_\alpha \tag{4.9}$$

$$^{8\mathrm{Be}}E_{ex} = \sqrt{E_{tot_i}^2 + E_{tot_j}^2 + 2E_{tot_i}E_{tot_j} - \bar{p}_i^2 - \bar{p}_j^2 - 2\bar{p}_i\bar{p}_j cos(\Delta\Theta)} - 2m_\alpha \tag{4.10}$$

$$\Delta\Theta = \arccos\left[\frac{2m_\alpha^2 + 2E_{tot_i}E_{tot_j} - (E_{ex} + 2m_\alpha)^2}{2\bar{p}_i\bar{p}_j}\right] \tag{4.11}$$

It is now evident that the $\Delta\Theta$ depends quadratically on the excitation energy, justifying

the resulting paraboloid shape in Figure 4.16.

With the obtained graph it is possible associate the structures in the angular separation distribution to the different energy levels. For example, it can be seen from the Figure 4.11 how the first peak corresponds to 92 KeV, which is the energy released in the $^{8}$Be decay in the ground state. By following the same pattern, the second $\Delta\Theta$ peak corresponds to the 3.03 MeV excited state. The plot also suggests that there should be a visible structure at $\sim 9.5^{\circ}$ corresponding to the excitation level around 11.5 MeV and a structure at $\sim 11.5^{\circ}$ corresponding to the level of 16.6 MeV. On the angular separation distribution in Figure 4.11, these structures are not evident maybe due to the poor statistics of $\alpha$ particles emitted with an high angular aperture between them.

By repeating the same kind of analyses but by taking into consideration reconstructed $\alpha$ particles, the results shown in Figure 4.17 were obtained.

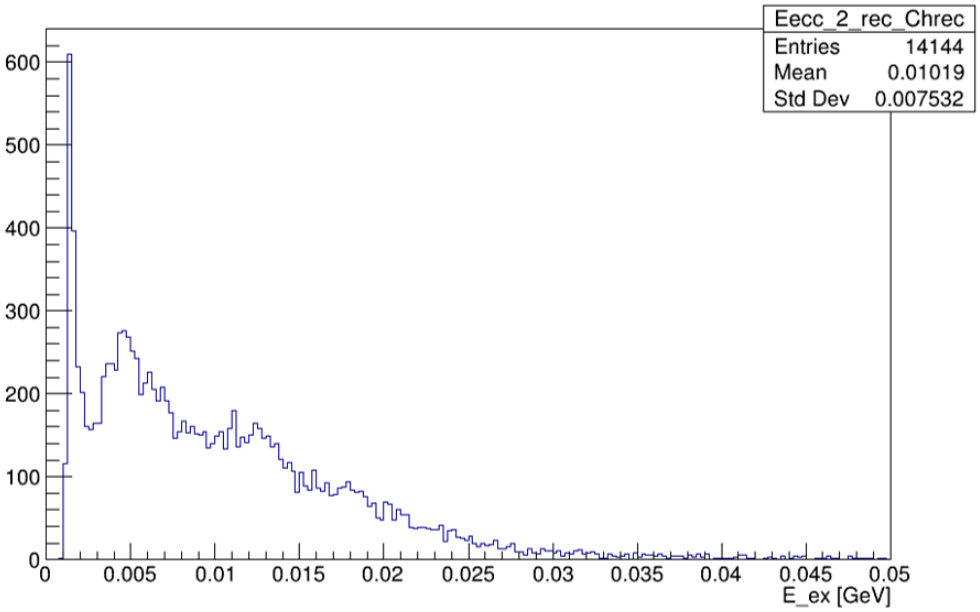


Figure 4.17: Excitation energy spectrum for the breakup of $^{8}$Be intermediate stage of $^{12}$C into two $\alpha$ particles from reconstructed $\alpha$ particles analysis.

It is evident how the same peaks previously explored are still present even if shifted to the right. This is the consequence of the reconstructed momentum overestimation compared to the MC true one seen in Section 4.3.3.

The peak resolution worsens from the MC analysis and this can be attributed to the momentum and charge mis-identification provided by the reconstruction software. In addition, in the data sample, there is also a background component due to the $\alpha$ particles production out of target that do not derive from the $^{8}$Be decay.

The excitation energy spectrum of $^{8}$Be VS the opening angle distribution between reconstructed $\alpha$ particles is presented in Figure 4.18.

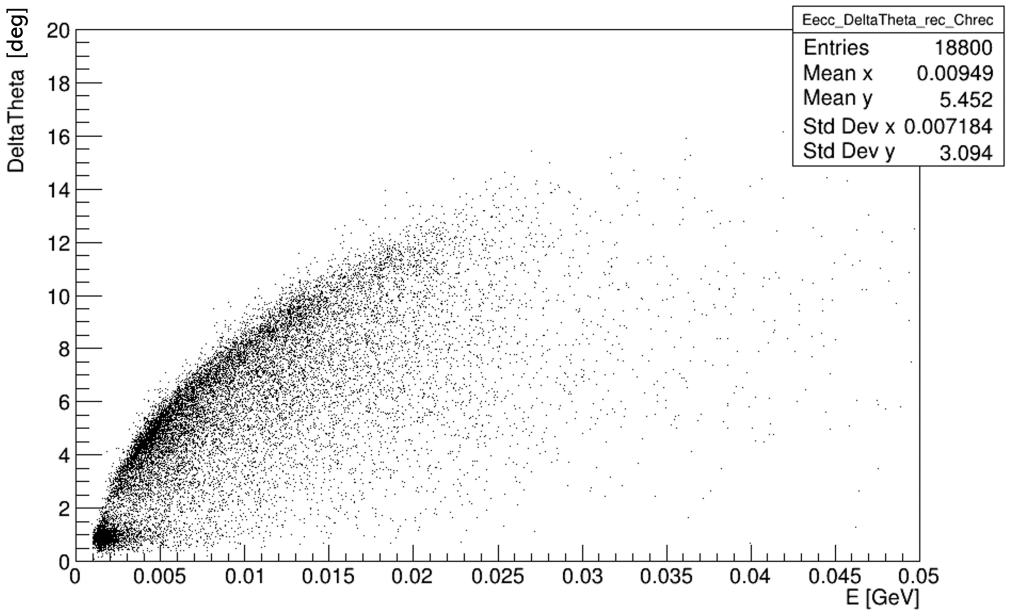


Figure 4.18: Excitation energy spectrum of the breakup of $^{8}$Be intermediate stage of $^{12}$C into two $\alpha$ particles VS the opening angular distribution between $\alpha$ particles in the Reconstruction analysis.

The resulting structures are less evident than the ones in Figure 4.16 due to the poor peak resolution shown in Figure 4.18 and because of the low statistic included in the Reconstruction analysis. For this reason, one of the future development of FOOT experiment in this realm is to reproduce the same kind of analyses employing a greater number of simulated primaries.

## 4.6. Analyses Results

From our investigation it was possible to retrieve information about the angular correlation between $\alpha$ particles and excitation energies of the nuclei from which they are emitted. In particular, the narrow peak at low $\Delta\Theta$ is present in the angular separation distribution demonstrating the strong angular correlation between $\alpha$ particles. It was seen that also at reconstruction analysis level we can retrieve the same information. This allows us to investigate the phenomena with real data from the FOOT experiment campaign. On the contrary, the reconstruction analysis regarding the excitation energy yields results tainted by low statistics and effects of mis-identification of charge and momentum resulting from the reconstruction software efficiency. Despite these challenges, the peaks corresponding

to the excited states of $^{8}$Be are visible and well distinguishable.

# 5 | Conclusions and future developments

The FOOT experiment was designed to measure differential cross-sections for particles at energies relevant to hadrontherapy and space radiation protection. This thesis aimed to explore the possibility of using this experiment to explore the $\alpha$ clustering phenomenology at energies around 200 MeV/nucleon, with a specific focus on the detection and measurement of $\alpha$ particles and their correlation resulting from the two decay channels of $^{12}$C, the direct one described by the reaction $^{12}$C($\alpha$, 2$\alpha$) and the one described by the intermediate stage involving $^{8}$Be in the reaction $^{12}$C($\alpha$, $^{8}$Be).

The goal of the project is to fill the current lack of theoretical models and experimental data on clustering phenomena at intermediate energies and to use the results as benchmark for the current MC simulation tools.

The FLUKA code was employed to simulate a primary beam of carbon ions with a kinetic energy of 200 MeV/u interacting with a carbon target.

By selecting $\alpha$ particles generated from the projectile fragmentation, the angular separation and excitation energy analyses were performed.

From the opening angular distribution between pairs of reconstructed $\alpha$ particles, peaks in correspondence of expected angular separation values for the fragments originating by the decay of $^{8}Be_{g.s.}$ and $^{8}Be^{*}_{3.03}$ are present. On the contrary, no corresponding peaks are visible by investigating the opening angle distribution between an $\alpha$ particle and particles other than $^{4}$He, demonstrating the absence of the angular correlation between them.

The excitation energy analysis is performed to examine the excitation levels of $^{8}$Be from the study of the detected pairs of $\alpha$ particles. By selecting the reconstructed $\alpha$ particles, it was possible to retrieve information about the first three energy levels implemented on FLUKA with good agreement even by taking into account the charge and the momentum mis-identification carried out by the reconstruction software. This demonstration can lay the groundwork for the observation of the same energy levels within collected real

data and to make the same analysis on other light nuclei, such as $^{12}$C and $^{16}$O. In this framework we are planning to start the study of the $^{12}$C excitation levels by means of the events with 3 detected $\alpha$ particles. In addition, the same setup could also be used to study the clustering of other even-even nuclei ($^{20}$Ne, $^{24}$Mg, etc.) for which there is still less data compared to $^{12}$C and $^{16}$O.

FOOT is proposed also to make the same kind of analysis by employing the ECC setup for lighter fragments.

Data collected by the FOOT experiment, whose constructions has been now completed, could help understanding whether the clustering phenomenology, deeply studied at lower energy, is still present at higher energies. This should be useful for the improvement of both theoretical models and of MC calculation models.

# Bibliography

[1] J.A. Peacock, S. Cole, P. Norberg, et al. A measurement of the cosmological mass density from clustering in the 2dF Galaxy Redshift Survey. , 410(6825):169–173, March 2001.

[2] M. Freer. Nucleon Clustering in Light Nuclei. In *Oxford Research Encyclopedia of Physics*, page 90. 2023.

[3] M. Freer. The clustered nucleus-cluster structures in stable and unstable nuclei. *Reports on Progress in Physics*, 70(12):2149, nov 2007.

[4] L. R. Hafstad and E. Teller. The alpha-particle model of the nucleus. *Phys. Rev.*, 54:681–692, Nov 1938.

[5] D.M. Brink and J.J. Castro. Alpha clustering effects in nuclear matter. *Nuclear Physics A*, 216(1):109–124, 1973.

[6] W. Wefelmeier. Ein geometrisches modell des atomkerns. *Zeitschrift für Physik*, 107(5):332–346, 1937.

[7] A. Tohsaki, H. Horiuchi, P. Schuck, et al. Alpha cluster condensation in $^{12}$C and $^{16}$O. *Phys. Rev. Lett.*, 87:192501, Oct 2001.

[8] Y. Funaki, T. Yamada, H. Horiuchi, et al. $\alpha$-particle condensation in $^{16}$O studied with a full four-body orthogonality condition model calculation. *Phys. Rev. Lett.*, 101:082502, Aug 2008.

[9] M. Chernykh, H. Feldmeier, T. Neff, et al. Structure of the hoyle state in $^{12}$C. *Phys. Rev. Lett.*, 98:032501, Jan 2007.

[10] H. Morinaga. Interpretation of some of the excited states of $4n$ self-conjugate nuclei. *Phys. Rev.*, 101:254–258, Jan 1956.

[11] D.M. Brink and E. Boeker. Effective interactions for hartree-fock calculations. *Nuclear Physics A*, 91(1):1–26, 1967.

[12] T. Otsuka, T. Abe, T. Yoshida, et al. $\alpha$-clustering in atomic nuclei from first principles

with statistical learning and the hoyle state character. *Nature Communications*, 13(1):2234, 2022.

[13] K. Ikeda, N. Takigawa, and H. Horiuchi. The Systematic Structure-Change into the Molecule-like Structures in the Self-Conjugate 4n Nuclei. *Progress of Theoretical Physics Supplement*, E68:464–475, 07 1968.

[14] N. Itagaki, W. von Oertzen, and S. Okabe. Linear-chain structure of three $\alpha$ clusters in $^{13}$C. *Phys. Rev. C*, 74:067304, Dec 2006.

[15] S. Ohkubo and Y. Hirabayashi. Bose-einstein condensation of $\alpha$ particles and airy structure in nuclear rainbow scattering. *Phys. Rev. C*, 70:041602, Oct 2004.

[16] A.C. Shotter. Elastic breakup of light projectiles for $(E/A)$ approx 10 mev/a. *Journal of the Physical Society of Japan;(Japan)*, 58, 1989.

[17] R.H. Dalitz. On the analysis of $\tau$-meson data and the nature of the $\tau$-meson. *The London, Edinburgh, and Dublin Philosophical Magazine and Journal of Science*, 44(357):1068–1080, 1953.

[18] P. Schuck, Y. Funaki, H Horiuchi, et al. Alpha particle clusters and their condensation in nuclear systems. *Physica Scripta*, 91(12):123001, nov 2016.

[19] Ad.R. Raduta, B. Borderie, E. Geraci, et al. Evidence for -particle condensation in nuclei from the hoyle state deexcitation. *Physics Letters B*, 705(1):65–70, 2011.

[20] D.R. Tilley, J.H. Kelley, J.L. Godwin, et al. Energy levels of light nuclei a=8,9,10. *Nuclear Physics A*, 745(3):155–362, 2004.

[21] L. Morelli, M. Bruno, M. D'Agostino, et al. $^{12}\mathrm{C} \rightarrow \alpha + \alpha + \alpha$ Reaction. *Annual Report 2014 of Laboratori Nazionali di Legnaro INFN.*

[22] M. Bruno, F. Gramegna, T. Marchi, et al. Garfield+ rco digital upgrade: A modern set-up for mass and charge identification of heavy-ion reaction products. *The European Physical Journal A*, 49:1–13, 2013.

[23] D. Dell'Aquila. *Clusters in light nuclear systems: a multi-method approach.* PhD thesis, Univerità degli studi di Napoli "Federico II", 2017.

[24] T. Toshito, K. Kodama, L. Sihver, et al. Measurements of projectile-like $^{8}$Be and $^{9}$B production in 200–400 mev/nucleon $^{12}$C on water. *Phys. Rev. C*, 78:067602, Dec 2008.

[25] G. De Lellis, S. Buontempo, F. Di Capua, et al. Measurement of the fragmentation of carbon nuclei used in hadron-therapy. *Nuclear Physics A*, 853(1):124–134, 2011.

[26] G. Battistoni, M. Toppi, V. Patera, and The FOOT Collaboration. Measuring the impact of nuclear interaction in particle therapy and in radio protection in space: the foot experiment. *Frontiers in Physics*, 8, 2021.

[27] M. Durante and J.S. Loeffler. Charged particles in radiation oncology. *Nature Reviews Clinical Oncology*, 7(1):37–43, 2010.

[28] M. Durante and H. Paganetti. Nuclear physics in particle therapy: a review. *Reports on Progress in Physics*, 79(9):096702, aug 2016.

[29] D. Schardt, I. Schall, H. Geissel, et al. Nuclear fragmentation of high-energy heavy-ion beams in water. *Advances in Space Research*, 17(2):87–94, 1996. Proceedings of the Meetings F2.6 and F2.7 of COSPAR Scientific Commission F which was held during the Thirtieth COSPAR Scientific Assembly.

[30] F. Sommerer, K. Parodi, A. Ferrari, et al. Investigating the accuracy of the fluka code for transport of therapeutic ion beams in matter. *Physics in Medicine Biology*, 51(17):4385, aug 2006.

[31] D. Thwaites. Accuracy required and achievable in radiotherapy dosimetry: have modern technology and techniques changed our views? *Journal of Physics: Conference Series*, 444(1):012006, jun 2013.

[32] R. Pleskac, Z. Abou-Haidar, C. Agodi, et al. The first experiment at gsi. *Nuclear Instruments and Methods in Physics Research Section A: Accelerators, Spectrometers, Detectors and Associated Equipment*, 678:130–138, 2012.

[33] J. Dudouet, D. Juliani, M. Labalme, et al. Double-differential fragmentation cross-section measurements of 95 mev/nucleon $^{12}$C beams on thin targets for hadron therapy. *Phys. Rev. C*, 88:024606, Aug 2013.

[34] M. Durante and F.A. Cucinotta. Physical basis of radiation protection in space travel. *Rev. Mod. Phys.*, 83:1245–1281, Nov 2011.

[35] M. Durante. Space radiation protection: Destination mars. *Life Sciences in Space Research*, 1:2–9, 2014.

[36] J.H. Heinbockel, T.C. Slaba, S.R. Blattnig, et al. Comparison of the transport codes hzetrn, hetc and fluka for a solar particle event. *Advances in Space Research*, 47(6):1079–1088, 2011.

[37] K. Duda, J. Majerczak, Z. Nieckarz, et al. Chapter 1 - human body composition

and muscle mass. In Jerzy A. Zoladz, editor, *Muscle and Exercise Physiology*, pages 3–26. Academic Press, 2019.

[38] R.A. Weldon, J.M. Mueller, P. Barbeau, et al. Measurement of ej-228 plastic scintillator proton light output using a coincident neutron scatter technique. *Nuclear Instruments and Methods in Physics Research Section A: Accelerators, Spectrometers, Detectors and Associated Equipment*, 953:163192, 2020.

[39] L. Galli, A.M. Baldini, F. Cei, et al. Wavedaq: An highly integrated trigger and data acquisition system. *Nuclear Instruments and Methods in Physics Research Section A: Accelerators, Spectrometers, Detectors and Associated Equipment*, 936:399–400, 2019. Frontier Detectors for Frontier Physics: 14th Pisa Meeting on Advanced Detectors.

[40] Z. "Abou-Haidar, C. Agodi, M.A.G. Alvarez, et al. Performance of upstream interaction region detectors for the FIRST experiment at GSI. *JINST*, 7:P02006, 2012.

[41] D. Yunsheng, G. Silvestre, S. Colombi, and The FOOT Collaboration. The Drift Chamber detector of the FOOT experiment: Performance analysis and external calibration. *Nucl.Instrum.Meth.A*, 986:164756, 2021.

[42] E. Spiriti, Ch. Finck, J. Baudot, et al. Cmos active pixel sensors response to low energy light ions. *Nuclear Instruments and Methods in Physics Research Section A: Accelerators, Spectrometers, Detectors and Associated Equipment*, 875:35–40, 2017.

[43] Sigmaphi. `https://www.sigmaphi.fr/en/`. Accessed: 2023-11-04.

[44] W. de Boer, V. Bartsch, and J. Bol andothers. Measurements with a cmos pixel sensor in magnetic fields. *Nuclear Instruments and Methods in Physics Research Section A: Accelerators, Spectrometers, Detectors and Associated Equipment*, 487(1):163–169, 2002. 3rd International Workshop on Radiation Imaging Detectors.

[45] Eljen plastic scintillator. `https://eljentechnology.com/products/plastic-scintillators`. Accessed: 2023-10-30.

[46] A.C. Kraan, G. Battistoni, N. Belcari, et al. Charge identification performance of a e-tof detector prototype for the foot experiment. *Nuclear Instruments and Methods in Physics Research Section A: Accelerators, Spectrometers, Detectors and Associated Equipment*, 958:162422, 09 2019.

[47] M. Morrocchi, E. Ciarrocchi, A. Alexandrov, et al. Development and characterization of a e-tof detector prototype for the foot experiment. *Nuclear Instruments and Methods in Physics Research Section A: Accelerators, Spectrometers, Detectors and Associated Equipment*, 916:116–124, 2019.

[48] L. Scavarda. Design and performance of the Calorimeter for the FOOT experiment. *Nuovo Cim. C*, 43(4-5):123, 2020.

[49] G. De Lellis et al. Emulsion Cloud Chamber technique to measure the fragmentation of a high-energy carbon beam. *JINST*, 2:P06004, 2007.

[50] M.C. Montesi, A. Lauria, A. Alexandrov, et al. Ion charge separation with new generation of nuclear emulsion films. *Open Physics*, 17:233–240, 05 2019.

[51] G. Galati, A. Alexandrov, B. Alpat, et al. Charge identification of fragments with the emulsion spectrometer of the foot experiment. *Open Physics*, 19:383–394, 07 2021.

[52] T.T. Böhlen, F. Cerutti, M.P.W. Chin, et al. The fluka code: Developments and challenges for high energy and medical applications. *Nuclear Data Sheets*, 120:211–214, 2014.

[53] A. Ferrari, P.R. Sala, A. Fassò, and J. Ranft. Fluka: a multi-particle transport code. *CERN Yellow report*, 2005-10, 01 2005.

[54] G. Battistoni, J. Bauer, T.T. Boehlen, et al. The fluka code: An accurate simulation tool for particle therapy. *Frontiers in Oncology*, 6, 2016.

[55] Fluka. `https:http://www.fluka.org`. Accessed: 2023-11-20.

[56] A. Ferrari and P.R. Sala. The Physics of High Energy Reactions. 9 1997.

[57] A. Capella, U. Sukhatme, C. Tan, et al. Dual parton model. *Phys. Rept.*, 236:225–329, 1994.

[58] G. Sterman. Quantum chromodynamics. In Jean-Pierre Françoise, Gregory L. Naber, and Tsou Sheung Tsun, editors, *Encyclopedia of Mathematical Physics*, pages 144–153. Academic Press, Oxford, 2006.

[59] H.D.I Abarbanel, J.D. Bronza, R.L. Sugar, et al. Reggeon field theory: Formulation and use. *Physics Reports*, 21(3):119–182, 1975.

[60] A. Ferrari, P.R. Sala, R. Guaraldi, et al. An improved multiple scattering model for charged particle transport. *Nuclear Instruments and Methods in Physics Research Section B: Beam Interactions with Materials and Atoms*, 71(4):412–426, 1992.

[61] A. Fassò, A. Ferrari, J. Ranft, et al. New developments in fluka modelling of hadronic and em interactions. 97, 01 1997.

[62] R.J. Glauber and G. Matthiae. High-energy scattering of protons by nuclei. *Nuclear Physics B*, 21(2):135–157, 1970.

[63] M. Cavinato, E. Fabrici, E. Gadioli, et al. Monte carlo calculations using the boltzmann master equation theory of nuclear reactions. *Physics Letters B*, 382(1):1–5, 1996.

[64] G. Battistoni, M. Cavinato, F. Cerutti, et al. Heavy ion interactions from coulomb barrier to few gev/n: Boltzmann master equation theory and fluka code performances. *Brazilian Journal of Physics*, 34, 09 2004.

[65] H. Sorge, H. Stoecker, and W. Greiner. Relativistic quantum molecular dynamics approach to nuclear collisions at ultrarelativistic energies. *Nucl. Phys. A*, 498:567C–576C, 1989.

[66] V. Andersen, F. Ballarini, G. Battistoni, et al. The fluka code for space applications: Recent developments. *Advances in space research : the official journal of the Committee on Space Research (COSPAR)*, 34:1302–10, 02 2004.

[67] S. Roesler, R. Engel, and J. Ranft. The monte carlo event generator dpmjet-iii. In Andreas Kling, Fernando J. C. Baräo, Masayuki Nakagawa, Luis Távora, and Pedro Vaz, editors, *Advanced Monte Carlo for Radiation Physics, Particle Transport Simulation and Applications*, pages 1033–1038, Berlin, Heidelberg, 2001. Springer Berlin Heidelberg.

[68] A. Fassò, A. Ferrari, and P. R. Sala. Photonuclear Reactions in FLUKA: Cross Sections and Interaction Models. *AIP Conf. Proc.*, 769(1):1303, 2005.

[69] S.M. Seltzer and M.J. Berger. Bremsstrahlung spectra from electron interactions with screened atomic nuclei and orbital electrons. *Nuclear Instruments and Methods in Physics Research Section B: Beam Interactions with Materials and Atoms*, 12(1):95–134, 1985.

[70] S.M. Seltzer and M.J. Berger. Bremsstrahlung energy spectra from electrons with kinetic energy 1 kev-10 gev incident on screened nuclei and orbital electrons of neutral atoms with z = 1-100. *Atomic Data and Nuclear Data Tables*, 35(3):345–418, 1986.

[71] L. D. Landau and I. Pomeranchuk. Limits of applicability of the theory of bremsstrahlung electrons and pair production at high-energies. *Dokl. Akad. Nauk Ser. Fiz.*, 92:535–536, 1953.

[72] E. Fermi. High Energy Nuclear Events. *Progress of Theoretical Physics*, 5(4):570–583, 07 1950.

[73] J. Rauch and T. Schl. Genfit - a generic track-fitting toolkit. *Journal of Physics: Conference Series*, 608(1):012042, apr 2015.

[74] F. Didierjean, G. Duchêne, and A. Lopez-Martens. The deterministic annealing filter: A new clustering method for -ray tracking algorithms. *Nuclear Instruments and Methods in Physics Research Section A: Accelerators, Spectrometers, Detectors and Associated Equipment*, 615(2):188–200, 2010.

[75] R. Frühwirth. Application of kalman filtering to track and vertex fitting. *Nuclear Instruments and Methods in Physics Research Section A: Accelerators, Spectrometers, Detectors and Associated Equipment*, 262(2):444–450, 1987.

[76] R. E. Kalman. A New Approach to Linear Filtering and Prediction Problems. *Journal of Basic Engineering*, 82(1):35–45, 03 1960.

[77] S. Gatti. Algoritmi di selezione e riconoscimento tracce nell'esperimento foot: identificazione degli eventi di fondo, 2023.

# List of Figures

# Acknowledgements

I would like to express my deepest gratitude to Dtt.ssa Muraro for her invaluable guidance, encouragement, and support throughout this research performed at the INFN laboratory of the Department of Physics at Università Statale di Milano.

I express my gratitude to Dtt. Battistoni and Dtt. Dong for their crucial daily supervision and guidance throughout the project. Their expertise and insightful feedback have been instrumental in shaping this work.

I wish to extend my appreciation to the FOOT Experiment team for introducing me to the realm of nuclear physics experimental research.

A special thanks goes to Professor Agosteo for giving me the opportunity to develop this thesis project.